UDK 66:54(05) CODEN HMIDA 8 ISSN 0367–598X

4

Hemijska industrija

Vol. 75

Časopis Saveza hemijskih inženjera Srbije

Chemical Industry

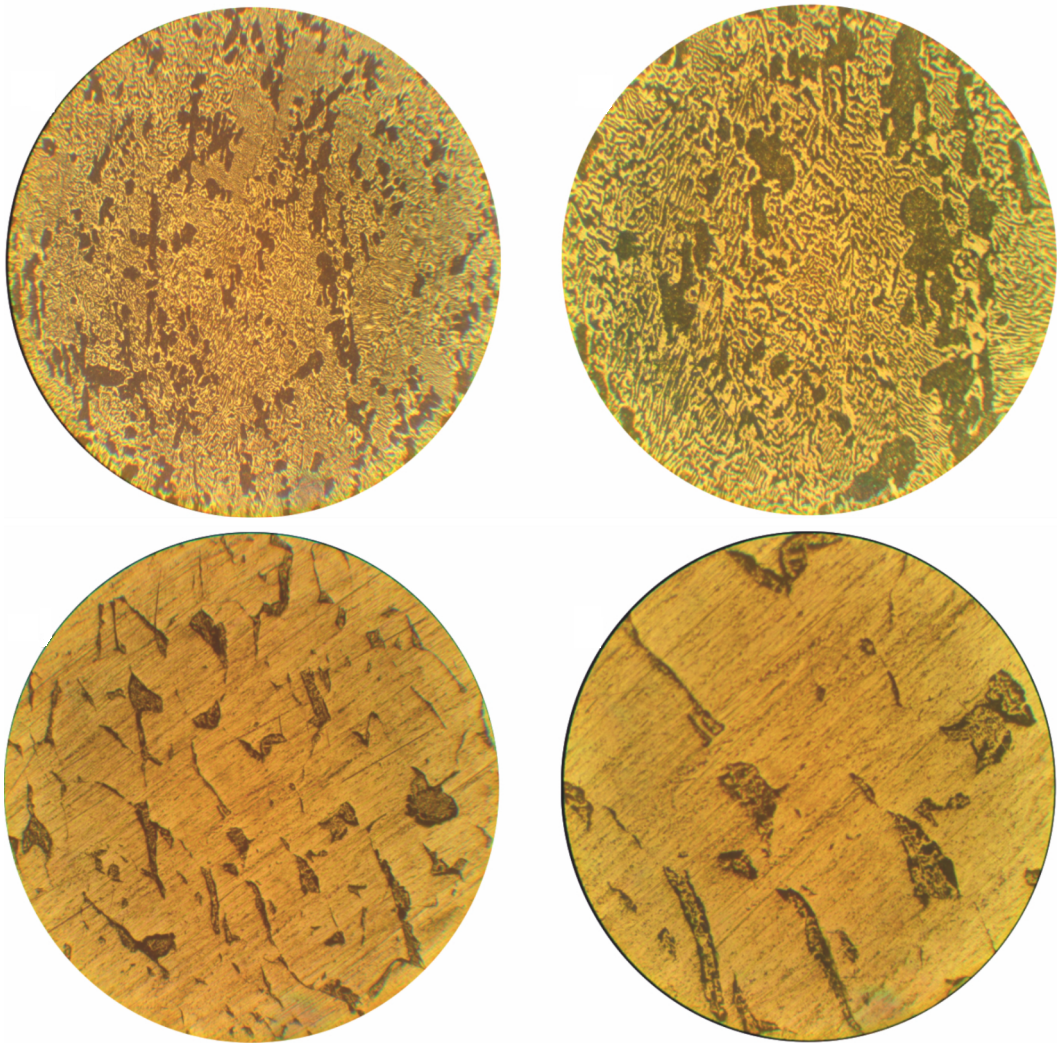

BEOGRAD, JULI-AVGUST 2021. HMIDA 8, 75 (4) 195 -256 (2021)

Aktivnosti Saveza hemijskih inženjera Srbije pomažu:

**MINISTARSTVO PROSVETE,
NAUKE I TEHNOLOŠKOG RAZVOJA
REPUBLIKE SRBIJE**

Tehnološko-metalurški fakultet
Univerziteta u Beogradu, Beograd

Institut za tehnologiju nuklearnih i
drugih mineralnih sirovina, Beograd

Hemijski fakutet Univerziteta u
Beogradu, Beograd

Prirodno-matematički fakultet
Univerziteta u Novom Sadu, Novi Sad

Institut za opštu i fizičku hemiju,
Beograd

Tehnološki fakultet
Univerziteta u Novom Sadu, Novi Sad

NU Institut za hemiju, tehnologiju i metalurgiju
Univerziteta u Beogradu, Beograd

Institut IMS, Beograd

Tehnološki fakultet
Univerziteta u Nišu, Leskovac

Fakultet tehničkih nauka,
Kosovska Mitrovica

Chemical Industry
Химическая промышленность

Hemijska industrija

Časopis Saveza hemijskih inženjera Srbije
Journal of the Association of Chemical Engineers of Serbia
Журнал Союза химических инженеров Сербии

VOL. 75 **Beograd, juli-avgust 2021.** **Broj 4**

Izdavač
Savez hemijskih inženjera Srbije
Beograd, Kneza Miloša 9/I

Glavni urednik
Bojana Obradović

Zamenica glavnog i odgovornog urednika
Emila Živković

Pomoćnik glavnog i odgovornog urednika
Ivana Drvenica

Urednici
Enis Džunuzović, Ivana Banković-Ilić, Maja Obradović, Dušan Mijin, Marija Nikolić, Tatjana Volkov-Husović, Đorđe Veljović,

Članovi uredništva
Nikolaj Ostrovski, Milorad Cakić, Željko Čupić, Miodrag Lazić, Slobodan Petrović, Milovan Purenović, Aleksandar Spasić, Dragoslav Stoiljković, Radmila Šećerov-Sokolović, Slobodan Šerbanović, Nikola Nikačević, Svetomir Milojević

Članovi uredništva iz inostranstva
Dragomir Bukur (SAD), Jiri Hanika (Češka Republika), Valerij Meshalkin (Rusija), Ljubiša Radović (SAD), Constantinos Vayenas (Grčka)

Likovno-grafičko rešenje naslovne strane
Milan Jovanović

Redakcija
11000 Beograd, Kneza Miloša 9/I
Tel/fax: 011/3240-018
E-pošta: shi@ache.org.rs
www.ache.org.rs

Izlazi dvomesečno, rukopisi se ne vraćaju

Za izdavača: Ivana T. Drvenica

Sekretar redakcije: Slavica Desnica

Izdavanje časopisa pomaže
Republika Srbija, Ministarstvo prosvete, nauke i tehnološkog razvoja

Uplata pretplate i oglasnog prostora vrši se na tekući račun Saveza hemijskih inženjera Srbije, Beograd, broj 205-2172-71, Komercijalna banka a.d., Beograd

Menadžer časopisa i Kompjuterska priprema
Aleksandar Dekanski

Štampa
Razvojno-istraživački centar grafičkog inženjerstva, Tehnološko-metalurški fakultet, Univerzitet u Beogradu, Karnegijeva 4, 11000 Beograd

Indeksiranje
Radovi koji se publikuju u časopisu *Hemijska Industrija* ideksiraju se preko *Thompson Reuters Scietific®* servisa *Science Citation Index - Expanded™* i *Journal Citation Report (JCR)*

SADRŽAJ/CONTENTS

Korelisanje uticaja veličine i sadržaja ojačavajućih čestica Al_2O_3 na tvrdoću kompozita sa aluminijumskom matricom dobijenih metodom vrtložnog livenja

Jasmina Lj. Petrović[1], Srba A. Mladenović[1], Aleksandra T. Ivanović[2], Ivana I. Marković[1] i Svetlana Lj. Ivanov[1]

[1]*Univerzitet u Beogradu, Tehnički fakultet u Boru, Bor, Srbija*
[2]*Institut za rudarstvo i metalurgiju Bor, Bor, Srbija*

Izvod

U ovom radu, za izradu kompozita sa metalnom matricom dobijenih metodom vrtložnog livenja, korišćena je legura EN AW 6061 kao metalna osnova, a čestice Al_2O_3 kao ojačivač. Kompoziti sa metalnom matricom su značajni inženjerski materijali i potrebno je detaljno proučiti načine proizvodnje i faktore koji utiču na mehanička svojstva. U tu svrhu, primenjen je planirani eksperiment i matematički je modelovana tvrdoća. Za razvoj korelacionog modela korišćen je pun faktorni plan eksperimenata, 3^2. Veličina i maseni udeo ojačavajućih čestica Al_2O_3 bili su uticajni faktori, a vrednosti tvrdoće odziv sistema. Uticajni faktori posmatrani su na tri nivoa: 50, 80 i 110 μm za veličinu čestica i 2, 5 i 8 mas. % za sadržaj ojačivača. Izmerene vrednosti tvrdoće, kretale su se u opsegu od 72 HV10 do 80 HV10. Višestrukom regresionom analizom, dobijen je polinom drugog reda kojim se mogu predvideti vrednosti tvrdoće kompozita sa metalnom osnovom. Određivanje uticaja ulaznih faktora na odziv sistema i provera adekvatnosti dobijenog regresionog modela, izvršena je primenom analize varijanse. Analiza rezultata je pokazala da veličina i maseni udeo ojačavajućih čestica imaju značajan uticaj na vrednosti tvrdoće kompozita sa metalnom osnovom i da predloženi regresioni model potvrđuje eksperimentalno dobijene rezultate.

Ključne reči: metalna osnova; faktorni eksperiment; odziv sistema.

Dostupno na web stranici časopisa: https://www.ache-pub.org.rs/index.php/HemInd/article/view/778

STRUČNI RAD

UDK: 669.714:661.183.8:620.178

Hem. Ind. **75 (4)** 195-204 (2021)

1. UVOD

Neprekidan razvoj nauke i tehnike doprineo je razvoju novih materijala za proizvodnju i dizajniranje inženjerskih proizvoda. Od sredine prošlog veka, posebna pažnja posvećuje se istraživanju kompozitnih materijala (kompozita) [1]. Kompoziti se sastoje od dva ili više materijala, različitih fizičkih i hemijskih osobina pri čemu su konačna svojstva kompozita bolja od svojstava sastavnih komponenti [2]. Veliki broj istraživača bavi se ispitivanjem čestičnih kompozita sa metalnom matricom (engl. Metal Matrix Composite - MMC). Kod ovih materijala razlikuju se dve osnovne sastavne komponente: metalna osnova (matrica) i ojačavajuća faza (ojačivač). Metali aluminijum, titan, magnezijum, bakar i njihove legure, najčešće se koriste kao osnova za izradu MMC [2,3]. Materijali za ojačavanje su keramičke čestice u obliku oksida (Al_2O_3, MgO, TiO_2), karbida (SiC, TiC, B_4C), nitrida (AlN, BN, Si_3N_4) i borida (TiB_2) [4,5]. Među njima, po značaju, posebno se ističu čestice Al_2O_3 i SiC [6]. Dodatak ojačivača metalnoj osnovi obezbeđuje: povećanu čvrstoću, veći modul elastičnosti, višu radnu temperaturu, poboljšanu otpornost na habanje, smanjenu težinu konstrukcionih delova, veliku električnu i toplotnu provodljivost, mali koeficijent termičkog širenja i dimenzionu stabilnost proizvoda u poređenju sa samim metalima i legurama [1,7-10]. MMC se odlikuju niskom cenom, izotropnim osobinama i mogućnošću proizvodnje upotrebom postojećih tehnologija [11,12]. Zastupljeni su u skoro svim granama industrije: automobilskoj, avio-industriji, vojnoj industriji, građevinarstvu, medicini i dr. Raznolikost u primeni, zahteva odgovore na mnoga pitanja u vezi sa dobijanjem i karakterizacijom metalnih kompozita [13,14].

Autor za prepisku: Jasmina Lj. Petrović, Univerzitet u Beogradu, Tehnički fakultet u Boru, Vojske Jugoslavije 12, 19210 Bor, Srbija
E-mail: jpetrovic@tfbor.bg.ac.rs
Članak primljen: 9. aprila 2021; Članak prihvačen: 19 juna 2021; Članak publikovan: 19. jula 2021.
https://doi.org/10.2298/HEMIND210409018P

U proizvodnji MMC, značajnu ulogu ima postupak njihovog dobijanja. Način proizvodnje primarno utiče na raspodelu ojačavajućih čestica u metalnoj osnovi. Sve veći broj skorašnjih istraživanja bavi se rešavanjem pitanja selekcije odgovarajućih tehnika za proizvodnju MMC i odabira adekvatnog ojačavajućeg materijala [14-17]. Podela tehnika za proizvodnju kompozita izvršena je na osnovu stanja metalne osnove (tečno ili čvrsto) u momentu mešanja sa ojačivačem. Zbog svoje jednostavnosti, ekonomičnosti i visoke proizvodnosti, posebno se izdvaja postupak dobijanja MMC primenom metode vrtložnog livenja (engl. „stir casting“) [4, 10]. Postupak podrazumeva da se nakon pretapanja metala u odgovarajućoj peći, ubacivanje ojačivača vrši uz primenu mešanja rastopa. Tokom mešanja, dolazi do formiranja vrtloga, koji obezbeđuje unošenje veoma slabo kvašljivih čestica ojačivača unutar rastopa i njihovo raspoređivanje.

U brojnim radovima [17-21], eksperimentalno je proučavan uticaj različitih faktora (veličina, oblik i maseni udeo ojačavajućih čestica, brzina i vreme mešanja, oblik mešača, temperatura izlivanja) na osobine dobijenog kompozita. Detaljno razumevanje uticaja različitih faktora na ispitivanu osobinu podrazumeva dugotrajan, komplikovan i skup eksperimentalni rad. Potreban je veliki broj eksperimenata za optimizaciju ispitivane pojave ili određenog procesa. U cilju skraćivanja eksperimentalnog rada i smanjenja troškova, koristi se metoda odzivne površine (engl. Responce Surface Methodology - RSM). Ova metoda predstavlja zbir matematičkih i statističkih tehnika koje služe za modelovanje i analizu problema u kojima na odziv sistema (zavisno promenljiva - y) utiče nekoliko faktora (nezavisno promenljive - x_0, x_2,... x_k) [22]. Metoda odzivne površine predviđa odziv sistema, analizira interakcije između faktora, definiše odnos između odziva i faktora i predviđa vrednosti odziva uz upotrebu ograničenog broja eksperimenata [23]. Brojni istraživači su koristili ovu metodu i razvili regresione modele za predviđanje različitih svojstava MMC [24,25].

Tako je razvijen regresioni model za predviđanje mikrotvrdoće kompozita na bazi aluminijumske legure EN AW 7075 ojačane česticama Al_2O_3 proizvedenih postupkom vrtložnog livenja koristeći faktorni plan eksperimenata sa četiri faktora na pet nivoa [24]. U drugoj studiji je za razvoj regresionog modela korišćena metoda odzivne površine i zaključeno je da je efekat zapreminskog udela ojačivača najuticajniji [25]. Na osnovu literaturnih istraživanja uticajnih faktora [26-29], primećeno je da na vrednosti tvrdoće, između ostalih, najviše utiču veličina i maseni udeo ojačavajućih čestica.

Cilj ovog rada je kreiranje regresionog modela na osnovu koga je moguće odrediti uticaj ispitivanih faktora (veličina i maseni udeo ojačavajućih čestica Al_2O_3) na tvrdoću aluminijumskih MMC. Za razvoj regresionog modela, bitan faktor je izbor plana eksperimenta [30]. U ovom ispitivanju, primenjen je pun faktorni plan eksperimenta (3^2). Statistička obrada rezultata izvedena je korišćenjem programskog paketa SPSS Statistics [31]. Adekvatnost matematičkog modela, statistički je proverena analizom varijanse (Analysis of variance - ANOVA) [22]. Ovakav pristup analizi uticajnih parametara, uz primenu odgovarajućeg plana eksperimenta, uspešno je primenjen u modelovanju mnogih metalurških procesa [32-37].

2. EKSPERIMENTALNI DEO

2. 1. Materijal i aparatura

Za izradu odlivaka korišćena je aluminijumska legura EN AW 6061 (Eling AD, Srbija) i čestice Al_2O_3 (Alumina DOO, Republika Srpska). Hemijski sastav korišćene legure, određen primenom spektrofotometra Niton XL3t, dat je u Tabeli 1 i on odgovara graničnim vrednostima propisanim standardom EN 573-3 [38].

Prilikom izrade MMC, ojačavajuće čestice Al_2O_3 dodavane su u tri različite veličine, 50, 80 i 110 μm i tri različita masena sadržaja, 2, 5 i 8 %.

Uzorci za eksperimentalna ispitivanja dobijeni su metodom vrtložnog livenja. Šematski prikaz korišćene aparature za izvođenje ovog postupka prikazan je na Slici 1.

Tabela 1. Hemijski sastav legure EN AW 6061 propisan standardom [38] i izmerene vrednosti u uzorku
Table 1. Chemical composition of EN AW 6061 alloy according to the standard [38] and measured values in the alloy sample

Element	Količina, mas.%		
	Minimalna [38]	Maksimalna [38]	Izmerena
Si	0,5	0,9	0,82
Cu	0,15	0,40	0,15
Fe	0	0,7	0,29
Zn	0	0,25	0,11
Mg	0,8	1,2	0,84
Mn	0	0,15	0,04
Ni	0	0,05	<0,03
Pb	0	0,05	<0,04
Sn	0	0,05	<0,04
Ti	0	0,15	0,02
Cr	0,04	0,35	0,13
Ti+Zr	0	0,20	0,01
Al	ostatak	ostatak	ostatak

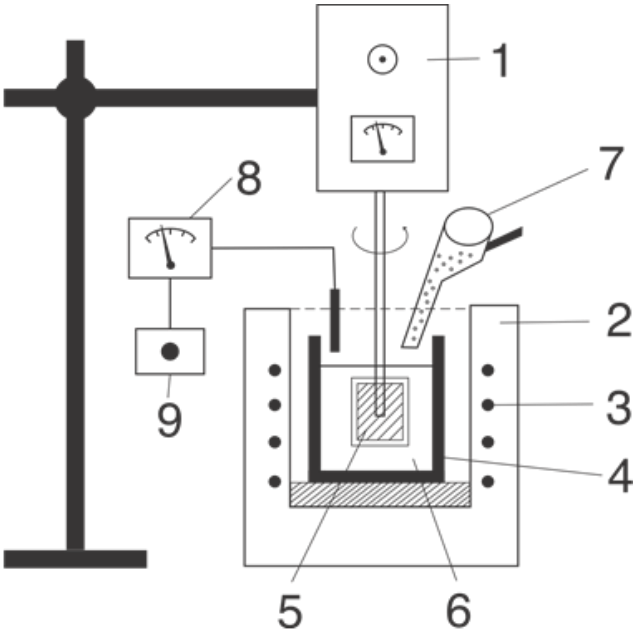

Slika 1. Šematski prikaz aparature za vrtložno livenje: 1 – motor sa regulacijom brzine, 2 – elektrootporna peć, 3 – grejači, 4 – grafitni lonac, 5 – mešač, 6 – istopljeni metal, 7 – levak za doziranje čestica ojačivača, 8 – termopar, 9 – regulator temperature
Figure 1. Scheme of the stir casting experimental set up: 1 - motor with speed regulation, 2 - electric furnace, 3 - heaters, 4 - graphite crucible, 5 - mixer, 6 - molten metal, 7 - funnel for dosing of reinforcing particles, 8 - thermocouple, 9 - temperature regulator

2. 2. Opis eksperimenta

Postupak vrtložnog livenja se zasniva na infiltraciji ojačavajućih čestica Al_2O_3 u istopljenu metalnu aluminijumsku osnovu EN AW 6061 legure uz mešanje rastopa. Legura EN AW 6061 istopljena je u grafitnom loncu zagrevanjem u elektrootpornoj peći na 800˚C. U istopljeni rastop dodat je 1 mas.% Mg (99,9 %, Wifred, Kina), kako bi se povećala kvašljivost ojačavajućih čestica. Posle potpunog topljenja, izvršeno je zahlađivanje rastopa do 710 °C, kako bi se povećala viskoznost. Nakon zahlađenja, u rastop je stavljen mešač od alatnog čelika oblika ploče, koji je zagrejan u peći na 350 °C kako se ne bi dodatno zahladio rastop. Nakon početka mešanja u rastop su ravnomerno dodate čestice Al_2O_3, koje su prethodno zagrejane u peći 3 h na 500 °C, radi uklanjanja vlage. Primenjena je brzina mešanja od 500 o/min. Nakon dodavanja ukupne količine ojačavajućih čestica, mešanje je nastavljeno još 5 min, u cilju njihove ravnomerne raspodele po celoj zapremini rastopa. Izlivanje MMC izvršeno je u grafitnom kalupu. Kalup je prethodno zagrejan na 350˚C radi

smanjenja poroznosti i ravnomernijeg očvršćavanja odlivka. Nakon dobijanja MMC sa različitim sadržajem (2, 5 i 8 mas.%) i različitom veličinom (50, 80 i 110 μm) Al_2O_3 čestica, izvršeno je merenje tvrdoće, pomoću Vikersovog aparata za merenje tvrdoće (VEB Leipzig, Nemačka) sa opterećenjem od 10 kg (HV10). Vreme zadržavanja pri maksimalnom opterećenju bilo je 10 s.

2. 3. Planirani eksperiment

U ovom radu, odziv sistema je tvrdoća kompozita (y), a uticajni faktori su veličina (x_1) i sadržaj (x_2) ojačavajućih čestica Al_2O_3. Planirani eksperiment podrazumeva plansku promenu uticajnih faktora da bi se procenio njihov efekat na odziv sistema. Opšti oblik matematičke zavisnosti odziva sistema od uticajnih faktora prikazan je jednačinom [35]:

$$y = f(x_1, x_2) + \varepsilon \quad (1)$$

gde su: y – odziv sistema i zavisi od uticajnih faktora x_1 *i* x_2; ε – ukupna greška eksperimenta, sadrži slučajnu grešku merenja i uticaje spoljašnje sredine koji nisu obuhvaćeni funkcijom f; $f(x_1, x_2)$ – površina predstavljena ovom funkcijom, odnosno odzivna površina.

Greška ε pokazuje razliku između izmerenih (stvarnih) vrednosti i vrednosti izračunatih po modelu. Ukoliko je greška manja, aproksimacija je bolja. U cilju smanjivanja greške, merenja tvrdoće su ponovljena deset puta za isti nivo faktora i izračunata je srednja vrednost.

Za predviđanja vrednosti tvrdoće kompozita na bazi legure EN AW 6061 ojačanih česticama Al_2O_3, eksperimentalni podaci su modelovani regresionim polinomom drugog reda [13,17], oblika:

$$y = \beta_0 + \beta_1 x_1 + \beta_2 x_2 + \beta_{11} x_1^2 + \beta_{22} x_2^2 + \beta_{12} x_1 x_2 \quad (2)$$

gde β_0, β_1, β_2, β_{11}, β_{22}, β_{12} predstavljaju koeficijente regresije. β_0 je koeficijent regresije preseka modela; β_1 i β_2 su koeficijenti regresije linearnih članova; β_{11} i β_{22} su koeficijenti regresije kvadratnih članova; β_{12} je koeficijent regresije interakcije uticajnih faktora.

Izabrani pun faktorni plan eksperimenata, 3^2, ima dva faktora od kojih je svaki sa tri nivoa (donji, osnovni i gornji), što znači ukupno 9 kombinacija nivoa faktora. U cilju lakšeg formiranja matrice, nivoi su kodirani sa -1, 0 i 1. Kodirane vrednosti su bezdimenzionalne veličine i izračunate su iz opšte jednačine [36]:

$$X = \frac{x - \frac{x_{max} + x_{min}}{2}}{\frac{x_{max} - x_{min}}{2}} \quad (3)$$

gde su: X – kodirana vrednost faktora; x - prava vrednost faktora; x_{min} i x_{max} – maksimalna i minimalna vrednost faktora, redom.

U Tabeli 2 prikazani su uticajni faktori, njihovi nivoi i intervali variranja faktora.

Tabela 2. Nivoi faktora modela
Table 2. Model factor levels

Faktor	Donji nivo	Osnovni nivo	Gornji nivo	Interval variranja
Veličina čestica ojačivača, μm	50	80	110	30
X_1	-1	0	1	
Sadržaj ojačivača, %	2	5	8	3
X_2	-1	0	1	

2. 4. Statistička analiza regresionog modela

Programski paket SPSS Statistics (IBM, NY) korišćen je za statističku analizu. Određeni su svi koeficijenti regresije (linearni, kvadratni i interakcije) i utvrđen je njihov efekat na predviđene vrednosti tvrdoće ANOVA testom. Rezultati statističke analize predstavljeni su tabelama ANOVA.

ANOVA test sproveden je radi utvrđivanja adekvatnosti modela i značajnosti koeficijenata regresione jednačine. Zbir kvadrata, broj stepena slobode, srednji kvadrati, F- i p-vrednosti korišćeni su kao statistički parametri. Statistička značajnost uticajnih faktora analizirana je na osnovu vrednosti p. Faktori su statistički značajni ako je p-vrednost manja

od 0,05. Adekvatnost regresionog modela ispitana je određivanjem koeficijenta determinacije (R^2) koji pokazuje koji procenat varijanse odziva sistema objašnjava model. Značaj modela je proveren pomoću *F*-testa.

3. REZULTATI I DISKUSIJA

U ovom radu analizirana su dva uticajna faktora na tri nivoa. Korišćen je pun faktorni plan eksperimenta, 3^2. Napravljeno je 9 uzoraka različitog sastava na kojima je merena tvrdoća. Izvršeno je deset merenja tvrdoće na svakom uzorku i izračunata srednja vrednost koja je korišćena u daljoj analizi. Razne kombinacije eksperimentalnih uslova (kodirani i nekodirani) sa odgovarajućim eksperimentalnim vrednostima tvrdoće (srednje vrednosti) predstavljene su u Tabeli 3. Eksperimentalne vrednosti tvrdoće kreću se u intervalu od 72 HV10 do 80 HV10. Najveća vrednost tvrdoće (80,45 HV10) izmerena je na uzorku sa najmanjom veličinom čestica Al_2O_3 (50 μm) i najvećim sadržajem (8 mas.%), a najmanje vrednosti tvrdoće (72,35 HV10) na uzorku sa najvećom veličinom čestica (110 μm) i najmanjim sadržajem (2 mas.%).

Tabela 3. Plan eksperimenata i odziv sistema
Table 3. Experimental design and system response

Broj eksperimenta	Kodirane vrednosti		Ulazne veličine		Tvrdoća, HV10 ± standardna devijacija
	X_1	X_2	Veličina čestica, μm	Sadržaj, %	
1	-1	-1	50	2	73,28 ± 2,25
2	-1	0	50	5	78,31 ± 2,64
3	-1	1	50	8	80,45 ± 3,04
4	0	-1	80	2	73,11 ± 2,38
5	0	0	80	5	78,13 ± 1,18
6	0	1	80	8	79,08 ± 2,50
7	1	-1	110	2	72,35 ± 1,14
8	1	0	110	5	77,91 ± 2,59
9	1	1	110	8	78,51 ± 2.16

Vrednosti koeficijenata regresije, *t*-testa, *p*-vrednosti i statistike kolinearnosti, koju čine tolerancija i faktor povećanja varijanse (Variance inflation factor – VIF) date su u Tabeli 4.

Tabela 4. Vrednosti koeficijenta regresije
Table 4. Values of the regression coefficients

Model	Nestandardizovani koeficijent regresije		Standardizovani koeficijent regresije	*t - test*	*p-vrednost*
	β	Standardna greška	β		
Konstanta	78,117	0,228		343,214	0,000
X_1	-0,545	0,161	-0,157	-3,386	0,020
X_2	3,217	0,161	0,925	19,987	0,000
X_1X_1	0,028	0,295	0,005	0,096	0,929
X_2X_2	-1,987	0,279	-0,330	-7,127	0,001
X_1X_2	-0,252	0,208	-0,059	-1,212	0,312

Rezultati iz Tabele 4 pokazuju da linearni članovi uticajnih faktora imaju statistički značajan uticaj na formiranje modela odziva *Y* na nivou $p < 0,05$. Veći uticaj na predviđanje vrednosti tvrdoće ispitivanih aluminijumskih kompozita ima sadržaj, u odnosu na uticaj veličine ojačavajućih čestica. Ovo se može objasniti činjenicom da veći sadržaj Al_2O_3 daje gušću raspodelu ojačivača u matrici i na taj način je povećana dodirna površina između metala i čestica [41]. Statistički značajan uticaj na formiranje modela odziva *Y* ima i kvadratni član masenog sadržaja ojačavajućih čestica. Koeficijenti koji nisu statistički značajni (kvadratni član veličine čestica i član interakcije ulaznih faktora) izuzimaju se iz regresionog polinoma. Tako se poboljšava sposobnost predviđanja predloženog modela.

Uzimajući u obzir samo statistički značajne parametre, formiran je matematički model uticaja veličine čestica i sadržaja ojačivača na vrednosti tvrdoće ispitivanih aluminijumskih kompozita:

$$Y = 78{,}117 - 0545X_1 + 3{,}217X_2 - 1{,}987X_2X_2 \quad (4)$$

Primenom regresionog polinoma (4) može se predvideti promena vrednosti tvrdoće dobijenog MMC, sa promenom veličine čestica i sadržaja ojačivača u granicama ispitivanih vrednosti ovih faktora.

Na osnovu vrednosti koeficijenata regresionog polinoma može se oceniti uticajnost pojedinih faktora. Vrednosti koeficijenata uz uticajne faktore X_1 i X_2 iznose -0,545 i 3,217. Poređenjem ovih vrednosti može se zaključiti da X_1 (sadržaj) ima pozitivan, a X_2 (veličina čestica) negativan uticaj na odziv sistema. Upoređivanjem standardizovanih koeficijenata β, takođe se može odrediti uticaj ispitivanih faktora na odziv sistema. Dolazi se do istih zaključaka kao i upoređivanjem koeficijenata regresionog polinoma.

Vrednovanje modela izvršeno je na osnovu rezultata statističke analize, korišćenjem vrednosti koeficijenta determinacije, R^2 (Tabela 5).

Tabela 5. Vrednovanje modela
Table 5. Model summary

Model	R	R^2	Korigovano R^2	Standardna greška procene
1	0,995	0,989	0,983	0,39422

Na osnovu rezultata prikazanih u Tabeli 5, zaključuje se da izabrani model objašnjava 98,9 % varijanse tvrdoće. Na osnovu literaturnih podataka [42] polinomi sa R^2>95 % mogu se smatrati prihvatljivim rezultatom nelinearne višestruke regresije, odnosno da je primenjeni model faktornog eksperimenta adekvatan. Ovako visok koeficijent determinacije ukazuje na izuzetno slaganje eksperimentalnih vrednosti i onih koje se modelom predviđaju.

Za procenu statističke značajnosti R^2 i adekvatnosti modela korišćen je ANOVA test i rezultati odstupanja su prikazani u Tabeli 6.

Tabela 6. Rezultati ANOVA testa modela drugog reda
Table 6. Results of the ANOVA test of the final second order polynomial model

Izbor varijabiliteta	Suma kvadrata odstupanja	Broj stepena slobode	Srednji kvadrat odstupanja	f - test	p - vrednost
Model	71,758	3	23,919	153,910	0,000
Ostatak	0,777	5	0,155		
Ukupno	72,535	8			

Sastavni deo statističke analize je grafički prikaz slaganja eksperimentalnih i vrednosti predviđenih regresionim modelom (Slika 2). Linija 1 predstavlja idealan položaj, a Linija 2 regresionu liniju. Kružićima na grafiku predstavljene su izmerene vrednosti tvrdoće. Uočava se da izmerene vrednosti tvrdoće leže vrlo blizu regresione linije (Linije 2), što ukazuje na odlično slaganje eksperimentalnih i predviđenih vrednosti. Na podudarnost izmerenih i izračunatih vrednosti ukazuje i visoka vrednost koeficijenta determinacije R^2=0,989.

Na slici 3 predstavljena je odzivna površina koja prikazuje promenu odziva sistema, tvrdoće, sa promenom uticajnih faktora, veličine i sadržaja ojačavajućih čestica.

Posmatrajući grafik sa slike 3, može se zaključiti da predviđene vrednosti tvrdoće rastu sa smanjenjem veličine čestica ojačivača i sa povećanjem njihovog sadržaja u matrici.

Na granici ojačivač-matrica dolazi do povećanja energije naprezanja, kao posledica različitih koeficijenata termičkog širenja aluminijumske osnove i ojačivača. Ova naprezanja izazivaju deformaciju rešetke metalne osnove i pojavu novih dislokacija [43,44]. Povećanje tvrdoće uslovljeno je otežanim kretanjem dislokacija usled prisustva ojačavajućih čestica u metalnoj osnovi. Veći sadržaj i manje dimenzije ojačavajućih čestica dovode do manjeg međučestičnog rastojanja u metalnoj osnovi, dodatno otežavaju kretanje dislokacija i utiču na poboljšanje mehaničkih osobina [20,45].

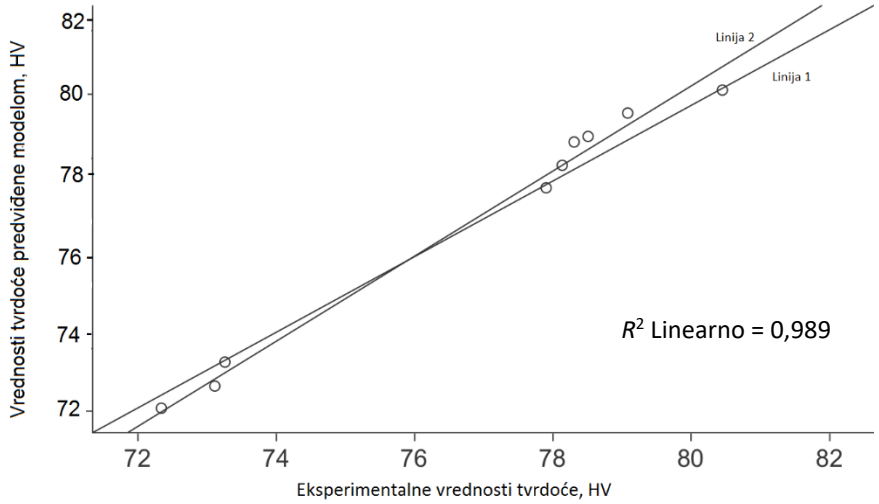

Slika 2. Zavisnost između eksperimentalnih i predviđenih vrednosti tvrdoće (linija 1 - idealan položaj, linija 2 - regresiona linija, o – izmerene vrednosti tvrdoće)

Figure 2. Correlation between experimental and predicted hardness values (line 1 - ideal position, line 2 - regression line, o - measured hardness values)

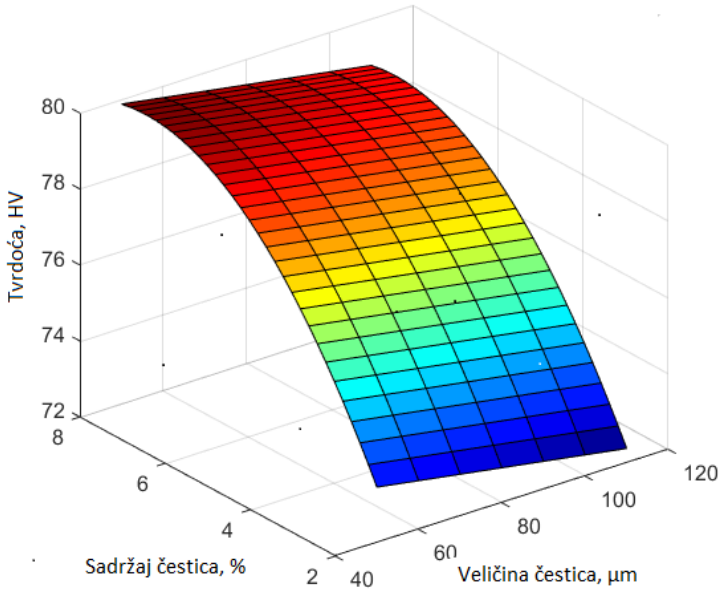

Slika 3. Zavisnost predviđenih vrednosti tvrdoće aluminijumskog kompozita od uticajnih faktora

Figure 3. Dependence of predicted hardness values of the aluminum composite on the investigated influencing factors

4. ZAKLJUČAK

MMC materijali na bazi EN AW 6061 legure koji sadrže 2, 5 i 8 mas.% ojačavajućih čestica Al_2O_3 veličine 50, 80 i 110 µm uspešno su dobijeni metodom vrtložnog livenja. Na osnovu analize efekata uticaja veličine i sadržaja ojačavajućih čestica Al_2O_3 na tvrdoću dobijenih aluminijumskih kompozita, zaključuje se da vrednosti tvrdoće opadaju sa povećanjem veličine, a rastu sa povećanjem sadržaja ojačavajućih čestica. Najveća vrednost tvrdoće (80,45 HV10) dobijena je za MMC sa najmanjom veličinom čestica (50 µm) i najvećim sadržajem (8 mas.%), a najmanje vrednosti tvrdoće (72,35 HV10) za MMC sa najvećom veličinom čestica (110 µm) i najmanjim sadržajem (2 mas.%).

Efekat uticajnih faktora na tvrdoću aluminijumskih MMC ispitan je primenom planiranog eksperimenta i statističke analize. Korišćenjem punog faktornog plana eksperimenata, 3^2, višestrukom regresionom analizom dobijena je matematička zavisnost za predviđanje vrednosti tvrdoće aluminijumskih MMC u funkciji veličine i sadržaja ojačavajućih čestica Al_2O_3. Statističkom analizom utvrđeno je da na formiranje matematičkog modela promene tvrdoće statistički

značajan uticaj imaju linearni članovi uticajnih faktora (veličina i maseni sadržaj ojačavajućih čestica) i kvadratni član masenog udela. Kvadratni član veličine čestica i član interakcije uticajnih parametara, nemaju statistički značajan doprinos u predviđanju vrednosti tvrdoće.

Razvijeni regresioni matematički model pokazuje izuzetno slaganje sa eksperimentalnim vrednostima (R^2=0,989). Primenjeni RSM model može se uspešno koristiti za predviđanje vrednosti tvrdoće aluminijumskog MMC ojačanog Al_2O_3 česticama u posmatranom intervalu ulaznih faktora odnosno veličine i sadržaja čestica ojačivača.

Zahvalnica: Istraživanja predstavljena u ovom radu su urađena uz finansijsku podršku Ministarstva prosvete, nauke i tehnološkog razvoja Republike Srbije, u okviru finansiranja naučno istraživačkog rada na Univerzitetu u Beogradu, Tehničkom fakultetu u Boru, prema ugovoru sa evidencionim brojem 451-03-9/2021-14/ 200131.

LITERATURA

[1] Calister WD, Rethwisch DG. *Materials Science and Engineering, An Introduction.* 9th ed., New York, NY: Wiley; 2014 ISBN: 978-1-118-71718-9.
[2] Mazumdar SK. *Composites Manufacturing: Materials, Product, and Process Engineering*. 1th ed., Boca Raton, USA: CRC Press; 2001 ISBN 0-8493-0585-3.
[3] Campbell FC. *Elements of Metallurgy and Engineering Alloys.* 1th ed., ASM International, USA; 2008 ISBN: 978-0-87170-867-0.
[4] Yigezu BS, Jha PK, Mahapatra MM. The key attributes of synthesizing ceramic particulate reinforced Al-based matrix composites through stir casting. *Materials and Manufacturing Processes*. 2013; 28: 969–979.
[5] Yigezu BS, Mahapatra MM, Jha PK. Influence of reinforcement type on microstructure, hardness, and tensile properties of an aluminum alloy metal matrix composite. *Journal of Minerals and Materials Characterization and Engineering*. 2013; 4: 124-130. http://dx.doi.org/10.4236/jmmce.2013.14022
[6] Telang AK, Rehman A, Dixit G, Das S. Alternate materials in automobile brake disc applications with emphasis on Al composites—A technical review. *Journal of Engineering Research and Studies*. 2010; 1: 35-46.
[7] Vencl A, Šljivić V, Pokusová M, Kandeva M, Sun HG, Zadorozhnaya E, Bobić I. Production, microstructure and tribological properties of Zn-Al/Ti metal-metal composites reinforced with alumina nanoparticles. *Inter Metalcast.* 2021. https://doi.org/10.1007/s40962-020-00565-5
[8] Vencl A, Bobić I, Bobić B, Jakimovska K, Svoboda P, Kandeva M. Erosive wear properties of ZA-27 alloy-based nanocomposites: Influence of type, amount and size of nanoparticle reinforcements. *Friction* 2019; 7(4): 340–350. https://doi.org/10.1007/s40544-018-0222-x.
[9] Manasijević S, Marković S, Radiša R. Primena novih tehnologija u cilju poboljšanja eksploatacionih svojstava klipova sus motora od aluminijumskih legura. *Zaštita materijala*. 2013; 1(54): 45-50. http://idk.org.rs/wp-content/uploads/2013/12/8SRECKO.pdf
[10] Burzić M, Sedmak S, Burzić Z, Jaković D, Momčilović D. Uticaj sadržaja ojačavača na udarnu žilavost livenog Al-SiCp metal matričnog kompozita. *Integritet i vek konstrukcija.* 2002; 1-2: 11-14. http://divk.inovacionicentar.rs/ivk/pdf/IVK1-2-2002-3.pdf
[11] Sakthive A, Palaninathan R, Velmurugan R, Rao PR. Production and mechanical properties of SiC_p particle-reinforced 2618 aluminum alloy composites. *J Mater Sci*. 2008; 43: 7047-7056. http://dx.doi.org/10.1007/s10853-008-3033-z
[12] Bayraktar E, Masounave J, Caplain R, Bathias C. Manufacturing and damage mechanisms in metal matrix composites. *Journal of Achievements in Materia and Manufacturing Engineering*, 2008; 2(31): 294-300.
[13] Miracle DB. Metal matrix composites from science to technological significance. *Compos. Sci. Technol*. 2005; 65 (15-16): 2526-2540. https://doi.org/10.1016/j.compscitech.2005.05.027
[14] Zhou MY, Ren LB, Fan LL, Zhang YWX, Lu TH, Quan GF, Gupta M. Progress in research on hybrid metal matrix composites. *J Alloy Compd.* 2020; 838: 1-40. https://doi.org/10.1155/2020/3765791
[15] George B, Sankar A, Bibin KT. Fabrication and characterization of aluminium hybrid composite. *International Journal of Engineering Sciences and Research Technology*. 2018; 7(4): 437-446.
[16] Shinde S. Manufactoring of aluminium matrix composite using stir casting method. *International Journal of Innovations in Engineering Research and Technology*. 2015; 2(5): 1-6.
[17] Bharath V, Nagaralb M, V Auradib V, Kori S. Preparation of 6061Al-Al_2O_3 MMC's by stir casting and evaluation of mechanical and wear properties. *Procedia Materials Science.* 2014; 6: 1658-1667. https://doi.org/10.1016/j.mspro.2014.07.151
[18] Alaneme KK, Bodunrin MO, Awe AA. Microstructure, mechanical and fracture properties of groundnut shell ash and silicon carbide dispersion strengthened aluminium matrix composites. *Journal of King Saud University – Engineering Sciences*. 2018; 30(1): 96–103. https://doi.org/10.1016/j.jksues.2016.01.001
[19] Prabhu SR, Shettigar AK, Herbert MA, Rao SS. Microstructure and mechanical properties of rutile-reinforced AA6061 matrix composites produced via stir casting process. *Trans. Nonferrous Met. Soc. China.* 2019; 29: 2229−2236. https://doi.org/10.1016/S1003-6326(19)65152-6

[20] Sajjadi SA, Ezatpour HR, Beygi H. Microstructure and mechanical properties of Al–Al_2O_3 micro and nano composites fabricated by stir casting. *Mater Sci Eng A*. 2011; 528: 8765-8771. https://doi.org/10.1016/j.msea.2011.08.052
[21] Baradeswaran A, Perumal AE. Study on mechanical and wear properties of Al7075/Al_2O_3/graphite hybrid composites. *Composites: Part B*. 2014; 56 : 464–471.
[22] Montgomery DC. *Response Surface Methods and Other Approaches to Process Optimization*. In: Montgomery DC, Design and Analysis of Experiments. 1st ed., New York, NY: John Wiley & Sons; 1997 ISBN 978-1118-14692-7.
[23] Khuri AI, Cornell JA. *Response Surfaces: Designs and Analyses*. 2nd ed., USA: CRC Press; 2019 ISBN 9780367401252.
[24] Deshmanya IB, Purohit GK. Development of mathematical model to predict micro-hardness of Al7075/Al_2O_3 composites produced by stir-casting. *Journal of Engineering Science and Technology Review*, 2012; 5(1): 44-50.
[25] Huda D, Baradie MA, Hasmi MSJ. Development of hardness model for MMCs (Al/A_2O_3). *Journal Materials Processing Technology*. 1994; 44: 81- 90. https://doi.org/10.1016/0924-0136(94)90040-X
[26] Anilkumar HC, Hebbar HS, Ravishankar KS. Mechanical properties of fly ash reinforced aluminium alloy (Al6061) composites. *International Journal of Mechanical and Mechatronics Engineering*. 2011; 6: 41–45.
[27] Kok M. Production and mechanical properties of Al_2O_3 particle-reinforced 2024 aluminium alloy composites. *Journal of Materials Processing Technology*. 2005; 161: 381–387.
[28] Kok M, Ozdin K. Wear resistance of aluminium alloy and its composites reinforced by Al_2O_3 particles. *Journal of Materials Processing Technology*. 2007; 183: 301–309. http://dx.doi.org/10.1016/j.jmatprotec.2006.10.021
[29] Mahdavi S, Akhlaghi F. Effect of the SiC particle size on the dry sliding wear behavior of SiC and SiC–Gr-reinforced Al6061 composites. *J Mater Sci*. 2011; 46: 7883–7894. https://doi.org/10.1007/s10853-011-5776-1
[30] Pantelić I. *Uvod u reoriju inženjerskog eksperimenta*. Novi Sad, Srbija: Radnički univerzitet „Radivoj Ćirpanov"; 1976.
[31] SPSS inc. PAWS Statistics 18, Predictive Analysis SoftwarePortfolio (www.spss.com).
[32] Ivanović A, Trumić B, Ivanov S, Marjanović S. Modelovanje uticaja temperatute i vremena homogenizacionog žarenja na tvrdoću PdNi5 legure. *Hem. Ind.* 2014; 68: 597–603. https://doi.org/10.2298/HEMIND130620085I
[33] Savić I, Nikolić G, Savić I, Cakić M, A. Dosić, Čanadi J. Modelovanje stabilnosti bioaktivnog bakar(II) kompleksa primenom eksperimentalnog dizajna, *Hem. Ind.* 2012; 66: 693–699. https://doi.org/10.2298/HEMIND120120021S
[34] Požega E, Ivanov S, Conić V, Čađenović B. Mogućnost procesa boriranja na presovanim uzorcima od železnog praha. *Hem.Ind*. 2009; 63: 253–258. https://doi.org/10.2298/HEMIND0903253P
[35] Ivanov S, Ivanić Lj, Gusković D, Mladenović S. Optimizacija režima starenja legura na aluminijumskoj osnovi. *Hem. Ind*. 2012; 66: 601–607.
[36] Ivanov S, Kočovski B, Stanojević B. Ocena uticaja termomehaničkih parametara prerade bakarne žice na izduženje spirale primenom faktornog eksperimenta. *Metalurgija.* 1996; 2: 13–23.
[37] Indumati D, Purohit G. Prediction of hardness of forged Al7075/Al_2O_3 composites using factorial design of experiments. *International Journal of Engineering Research and Applications*. 2012; 2: 84–90.
[38] BS EN 573-3: Aluminium and aluminium alloys. Chemical composition and form of wrought products. Chemical composition and form of products. 2019.
[39] Raymond HM, Douglas MC. *Response Surface Methodology: Process and Product Optimization Using Designed Experiments. 4th* ed., New York, NY: John Wiley & Sons; 2016 ISBN: 978-1-118-91601-8.
[40] Bas D, Boyaci IH. Modeling and optimization I: Usability of response surface methodology. *J. Food Eng*. 2007; 78: 836-845. https://doi.org/10.1016/j.jfoodeng.2005.11.024.
[41] Raghavendra N, Ramamurthy VS. Effect of particle size and weight fraction of alumina reinforcement on wear behavior of aluminum metal matrix composites. *International Journal of Innovative Research in Science, Engineering and Technology.* 2014; 4(3): 11191-11198.
[42] Mihajlović I, Nikolić Đ, Jovanović A. *Teorija sistema*. 1st ed., Bor, Srbija: Tehnički fakultet u Boru; 2009.
[43] Boopathi MM, Arulshri KP, Iyandurai N. Evaluation of mechanical properties of aluminium alloy 2024 reinforced with silicon carbide and fly ash hybrid metal matrix composites. *American Journal of Applied Sciences.* 2013; 10(3): 219-229. https://doi.org/10.3844/ajassp.2013.219.229
[44] Singh J, Suri N, Verma A. Affect of mechanical properties on groundnut shell ash reinforced Al 6063. *International Journal for Technological Research in Engineering*. 2015; 11(2): 2619-2623.
[45] Ashok N, Shanmughasundaram P. Effect of particles size on the mechanical properties of SiC-reinforced aluminium 8011 composites. *Materials and Technology*. 2017; 51(4): 667-672. https://doi.org/10.17222/mit.2016.252

ABSTRACT

Correlation of hardness of aluminum composites obtained by stir casting technology and the size and weight fraction of reinforcing Al_2O_3 particles

Jasmina Lj. Petrović[1], Srba A. Mladenović[1], Aleksandra T. Ivanović[2], Ivana I. Marković[1] and Svetlana Lj. Ivanov[1]

[1]*University of Belgrade, Technical Faculty in Bor, Bor, Serbia*
[2]*Mining and Metallurgical Institute Bor, Bor, Serbia*

(Technical paper)

In this work, the stir casting method was applied to obtain composites based on the alloy AN EW 6061 used as a metal base, and Al_2O_3 particles as a reinforcement. Composites play a significant role as engineering materials. Therefore, it is necessary to study, in detail, the production methods and the factors that affect their mechanical properties. For this purpose, we have carried out a planned experiment wi ASM International th the aim to use regression analysis to predict the influence of particle size and mass fraction on hardness of the obtained composites. The full factorial experimental design with two factors was used, which was analyzed at three levels. Hardness was observed as a system response, while particle size and mass fraction were set as influencing factors. Influencing factors were observed at three levels: 50, 80 and 110 μm for the particle size and 2, 5 and 8 mass%. Measured hardness values of the composites ranged from 72 HV10 to 80 HV10. Based on the probability values ($p<0.05$), it was determined which factors are important for the system response. Statistical analysis has shown that linear terms of the influence factors (size and mass fraction of reinforcement particles) and the square term of the mass fraction have statistical significance on the hardness change. The square term of the particle size and the interaction term of the influencing parameters do not have a statistically significant contribution in predicting the hardness value. Thus, a second-order polynomial model was obtained by the regression analysis. Influence of input factors on the system response and the adequacy of the obtained mathematical model were determined by using the Analysis of Variance (ANOVA). Based on the statistical data analysis, it was established that, the particle mass fraction has a greater influence on hardness of the obtained composite in relation to the particle size. By comparing the experimental and predicted values, a high degree of agreement was achieved so that the chosen model of the factorial experiment was adequate (R^2=0.989). It can be also concluded that the developed regression model can be applied to predict hardness of the aluminum composite reinforced by Al_2O_3 particles in the chosen variation interval of particle size and mass fraction.

Keywords: metal matrix; factorial experiment; system response

Lithium carbonate sedimentation using flocculants with different ionic bases

Yam Morales[1], Nelson Herrera[1,2] and Kevin Pérez[1,3,4]

[1]*Metallurgical and Mining Engineering Department, Universidad Católica del Norte, Antofagasta 1270709, Chile*
[2]*Oulu Mining School, University of Oulu, Oulu 90570, Finland*
[3]*Faculty of Engineering and Architecture, Universidad Arturo Prat, Almirante Juan José Latorre 2901, Antofagasta 1244260, Chile*
[4]*Department of Chemical Engineering and Mineral Processes, Faculty of Engineering, Universidad de Antofagasta, Antofagasta 1270300, Chile*

Abstract

Lithium has become a metal of enormous interest worldwide. The extensive use of rechargeable batteries for a range of applications has pushed for rapid growth in demand for lithium carbonate. This compound is produced by crystallization, by reaction with lithium chloride (in solution) and by adding sodium carbonate. Low sedimentation rates in the evaporation pools present a problem in the crystallization process. For this reason, in this work, mineral sedimentation tests were carried out with the use of two flocculant types with different ionic charges. The tests were carried out at a laboratory level using different dosages for each flocculant and measurements were performed to obtain the increase in the content of solids in the sediment. The anionic flocculant had better performance as compared to that of the cationic flocculant, increasing the sedimentation rate of lithium carbonate by up to 6.5. However, similar solids contents were obtained with the use of the cationic flocculant at 3.5 times lower dosage making it the flocculant of choice regarding the economic point of view.

Keywords: Brine treatment; anionic flocculation; cationic flocculation; nonferrous metals; mining.
Available on-line at the Journal web address: http://www.ache.org.rs/HI/

TECHNICAL PAPER

UDC: 661.834-032.26:544.77.052.22

Hem. Ind. **75 (4)** 205-212 (2021)

1. INTRODUCTION

The mining industry in Chile is constantly growing [1–4] . Historically, Chile has traded copper, this commodity being the main economic income contributing approximately 10 % of the gross domestic product (GDP) [5]. However, the quantity of high-grade Cu minerals on the surface is decreasing [6]. Therefore, in recent years, considerable investments have been made in utilization of other elements, lithium being the second most exploited commodity in the country [7].

Lithium is an electrochemically active metal and it has been recognized as one of the critical materials for the advancement of modern life due to its superior properties compared to other materials, such as redox potential and specific heat capacity [8]. This metal has a low atomic mass, low coefficient of thermal expansion, and high electrochemical reactivity, which has made it a particularly attractive material for use in rechargeable batteries for electronic devices, electric vehicles, and network storage systems [9,10].

The commercial value of lithium carbonate has increased over the years to reach US $ 13 per kg in 2017 [9]. In turn, the production of LCE (Lithium Carbonate Equivalent) also increased, so that during 2016 approximately 200,000 tons were produced, where Argentina is the largest producer (58.3%) followed by Chile (38.9 %) [11]. It is precisely in South America where the largest reserves are concentrated [12] (85 % of lithium reserves in brines) [13], accompanied also with other elements such as potassium, sodium, boron, sulfate and chlorides [14].

Prices doubled between 2013 and 2017 and lithium demand is expected to triple by 2025, with the World Bank estimating a 965 % increase in demand by 2050 [15]. By 2025, the investment banking group UBS forecasts that batteries

Corresponding author: Kevin Pérez, Metallurgical and Mining Engineering Department, Universidad Católica del Norte, Antofagasta 1270709, Chile; Tel: +56957694202
E-mail keperez@unap.cl
Paper received: 28 November 2020; Paper accepted: 03 July 2021; Paper published: 08 August, 2021
https://doi.org/10.2298/HEMIND201128020M

will account for at least 80 % of the total lithium demand in the application industries [15]. Chilean lithium production comes from companies located in the Salar de Atacama (SQM and Albemarle).

Given the low concentration of this metal in nature reserves and other difficulties in its extraction from hard rocks, many industrially advanced countries have struggled to ensure an uninterrupted supply of lithium to meet their manufacturing demands. This fact has a significant impact on the price of lithium in the international market. For example, in 2017 in China, there was an increase in the price of lithium carbonate to US$ 6,400-12,000 per ton from US $ 2,000 per ton in 2005 [16]. Therefore, innovative processes to increase lithium production must be developed and evaluated to meet future demands.

Lithium is present in a wide range of minerals (spodumene, lepidolite, petalite, amblygonite, and eucriptite). At the same time, lithium is found in natural brines, brines associated with oil wells and geothermal fields. It is also present in various clays (hectorite being the most important) and even in seawater [17]. Although the sources of lithium can be diverse, at present only two production processes are economically feasible: using brines and minerals, with brine being mostly used [18], due to lower manufacturing costs in comparison with the costs of extraction and processing of lithium minerals [19].

The composition of commercial brines from which lithium is recovered varies considerably from brines with low lithium contents (0.02 %) to some with higher contents (close to 0.4 %), with the presence of other elements and salts such as potassium, sodium, calcium, magnesium, iron, boron, bromine, chlorine, nitrates, chlorides, sulfates and carbonates, which imposes a requirement that each brine is treated in a particular way, according to its composition.

The production of lithium carbonate from brines is carried out by precipitation [20]. This lithium compound is the most important compound commercially produced and represented 60 % of the market share of commercial products based on lithium in 2017 [21]. Lithium carbonate precipitation using sodium carbonate (Na_2CO_3) has been commonly used in industry as well as in research as the final step to produce crystals in a hydrometallurgical process [21].

After extraction of the brine (Sª) from a salt flat, it is pumped into huge pools for concentration of lithium, resulting in a decrease in the lithium content from an average value of 600 mg dm^{-3} in the Puna salt flats, to about 5,000 to 10,000 mg dm^{-3}. As a consequence of water evaporation, significant amounts of NaCl crystallize in the pools, accompanied with crystallization of KCl and, depending on the brine composition, other salts, such as $CaSO_4$ [22].

Prior to lithium precipitation, it is necessary to reduce calcium and magnesium contents, which is achieved by chemical precipitation (equations 1 and 2), with the use of calcium hydroxide ($Ca(OH)_2$), sodium carbonate (Na_2CO_3) or sodium sulfate (Na_2SO_4). In the case of boron, its removal is achieved by solvent extraction and/or ion exchange [22].

$$Ca(OH)_2 + Mg^{2+} \rightarrow Mg(OH)_2 + Ca^{2+} \quad (1)$$

$$Na_2(SO)_4 + Ca^{2+} \rightarrow Ca(SO)_4 + 2Na^{+} \quad (2)$$

The lithium carbonate precipitation stage is carried out at a high temperature (90 ºC), by adding sodium carbonate to the concentrated and purified brine [22] as:

$$Na_2(CO)_3 + 2Li^{+} \rightarrow Li_2(CO)_3 + 2Na^{+} \quad (3)$$

Once the carbonate is obtained, particle sedimentation begins at rather low rates, which motivated this investigation. In order to reduce the sedimentation time, it is necessary to add certain reagents that help formation of flocs or particle binding, thus increasing the particle weight and, consequently, the sedimentation rate [23]. In the present work, we present the importance of the use of flocculants to increase production of lithium carbonate, by reducing the sedimentation time.

Flocculation of colloidal particles is typically performed by using high molecular weight polyacrylamides, which can be different with respect to the electrical charge (cationic, anionic, or non-ionic), depending on the use required. Typical chemical structures of anionic, neutral, and cationic polyacrylamides used as flocculants.

2. MATERIALS AND METHODS

2.1. Lithium carbonate sample

Lithium carbonate was acquired from Merck (N" CAS 554-13-2; Chile), having a density of 2.11 g cm^{-3}. To reproduce a brine, lithium carbonate was mixed with water up to a 7.5 wt.% solid content.

2.2. Flocculant preparation

As a cationic flocculant interfloc 5002 was used while SNF 60420 was used as the anionic flocculant. Small flocculant crystals were dissolved in distilled water at the concentration of 1g dm^{-3} while stirring on a magnetic stirrer for 5 h due to the high density of the reagent to obtain a homogeneous solution (without lumps).

2.3. Sedimentation tests

In the present work, the flocculant amounts for the sedimentation tests were 5, 15, 30, 50, 75, 100, 125, 150, 175, 200 and 275 g t^{-1} for each flocculant type. The chosen dosages are the typical values used in non-metallic mining industry.

Sedimentation tests, performed in duplicates, were conducted by pouring 270 cm^3 of the homogeneous pulp into a cylinder and performing interface height measurements every 20 min (due to the low sedimentation rate of lithium carbonate) at the lowest point of clear liquid. The test tubes were previously graduated at the mm precision.

For pulp characterization, the mineralogical and chemical features can be reflected in the content of solids [24]. The relative proportion in which the mineral and water are found is represented by the solid content (C_p), which corresponds to the content ratio of the mineral weight to the pulp weight (eq. 7). For this calculation, from the data obtained in the laboratory, the solid content by volume (C_v) is obtained by using eq. (6) and the volume of the thickened pulp (eq. 5) from the conditions in the developed test. The content of solid is determined at the moment at which the height of the interface stops changing, that is, it does not decrease further.

The volume of ore is calculated as:

$$V_m = \frac{m}{\rho_s} \tag{4}$$

The volume of the thickened pulp is calculated as:

$$\text{Thikened volume} = \pi r^2 h_n \tag{5}$$

The solid content by volume is calculated as:

$$C_v = \frac{V_s}{V_p} 100 \tag{6}$$

The solid content by weight is calculated:

$$C_p = \frac{\rho_s C_v}{(1-C_v)\rho_l + \rho_s C_v} 100 \tag{7}$$

V_m - Mineral volume C_v - Solid content by volume m - Mineral mass
V_p - Pulp volume ρ_s - Mineral density V_s - Solid volume
r - Specimen inner radius C_p - Solid content by weight h_n - Height at each measurement

2. 4. Sedimentation rate

Once the tests in duplicates have been completed, the average height values at each measured time were graphically presented (Figure 1.) and the sedimentation rate is obtained by using the Coe and Clevenger method as the slope of the initial tangent line. In the present investigation first three points were used for construction of the tangent, with the aim to minimize error.

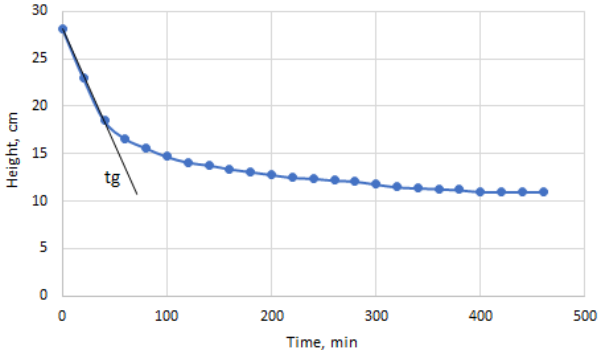

Figure 1. Determination of the sedimentation rate as a slope of the tangent *(tg) at initial values of* the *thickened pulp height vs. time*

3. RESULTS AND DISCUSSION

Table 1. presents the content of lithium carbonate in the sediment after 460 min based on utilization of both flocculant types (anionic and cationic).

Table 1. Content of solids in the sediment obtained in flocculation tests after 460 min.

Dosage, g t^{-1}	Cationic flocculant		Anionic flocculant	
	Content of solids, wt.%	Standard deviation, %	Content of solids, wt.%	Standard deviation, %
0	11.17	± 1.07	11.17	± 1.07
5	15.96	± 2.90	14.88	± 2.36
15	16.08	± 2.58	15.29	± 2.47
30	16.44	± 2.91	15.51	± 2.62
50	17.21	± 2.86	16.20	± 2.23
75	16.95	± 2.76	16.44	± 2.65
100	16.69	± 2.55	16.20	± 2.11
125	16.56	± 2.51	15.62	± 2.42
150	16.69	± 2.48	15.51	± 2.06
175	15.40	± 2.04	18.68	± 2.38
200	15.73	± 2.29	17.77	± 3.01
275	15.19	± 1.90	15.40	± 2.52

The highest solid concentrations in the sediments were ~17 % for the cationic and ~19 % for the anionic flocculant. To reach these concentrations, dosages of 50 and 175 g t^{-1} for the cationic and anionic flocculant, respectively, were used, which indicates an exceptionally large difference between these two flocculant types. The cationic flocculant is used for sedimentation of non-metallic and organic particles, whereas the anionic one is more used for metallic materials [25].

Accordingly, higher contents of solids were achieved for the cationic flocculant in most of the cases, but it should be noted that above the dosage of 175 g t^{-1} the opposite is observed that is higher solid concentrations for the anionic flocculant. The cause of this phenomenon is high adsorption of the flocculant on the particles, reducing the particle surface area to interact with the polymer chain attached to another particle [26], which causes a large part of the solids to remain in suspension.

Figure 2. presents the sediment height over time for the two tests producing the best results.

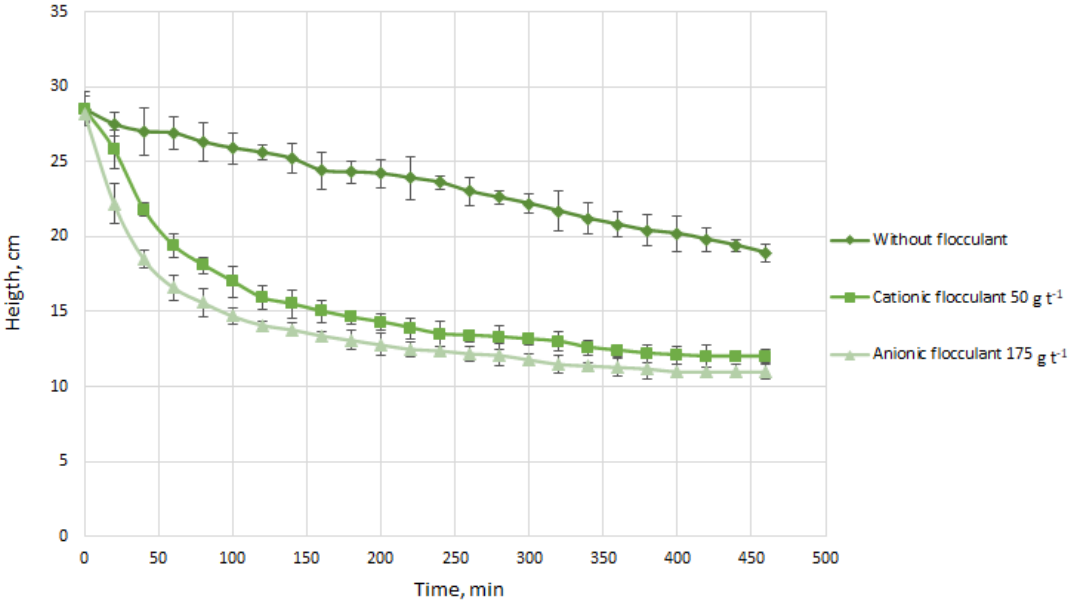

Figure 2: Interface height over time for the control sedimentation test (without flocculant) and the tests with the use of 50 g t^{-1} cationic flocculant and 175 g t^{-1} anionic flocculant

A noticeable difference is seen with regard to the final interface heights obtained in the sedimentation tests, decreasing from 28.5 cm to 12 cm for the cationic flocculant and to 11 cm for the anionic flocculant. Thus, there is a greater compaction of the sediment and consequently a higher content of solids is obtained, possibly due to lower entrapment of water in the test with the anionic flocculant in the compaction zone.

Figure 3. and Figure 4. show the solids concentrations in the sediment zone over time for the cationic and anionic flocculant, respectively, at the dosages studied. It can be seen that the increase in the solids content is not very large (it increases from 7.5 % to approximately 18 %), possibly due to the inverse solubility of lithium carbonate [27]. In specific, at low temperatures, sedimentation is minor because part of the lithium carbonate is dissolved in the solution, thus reducing the number of particles.

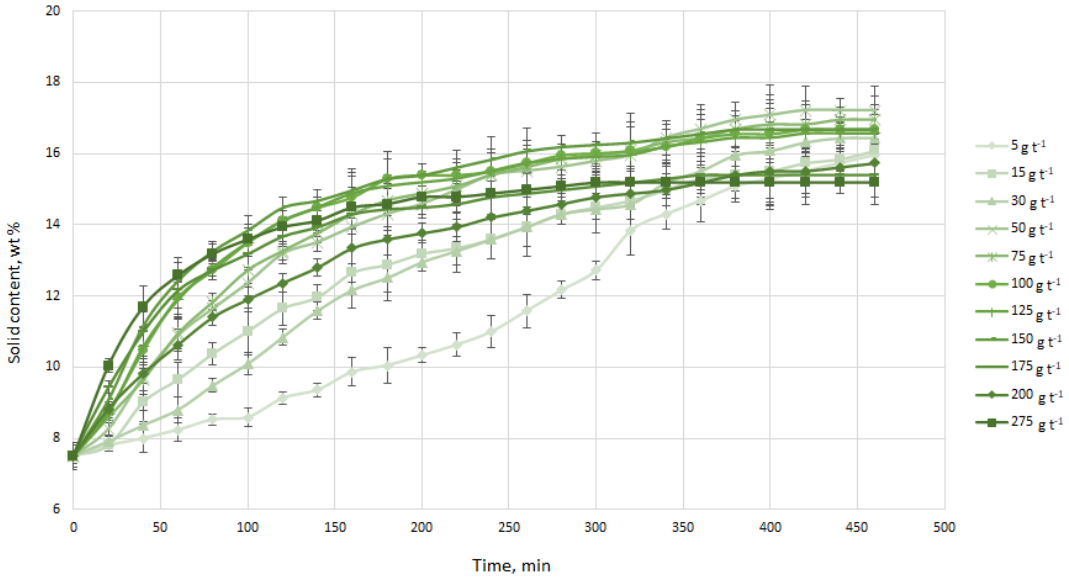

Figure 3: Solids content over time at different dosages of the cationic flocculant

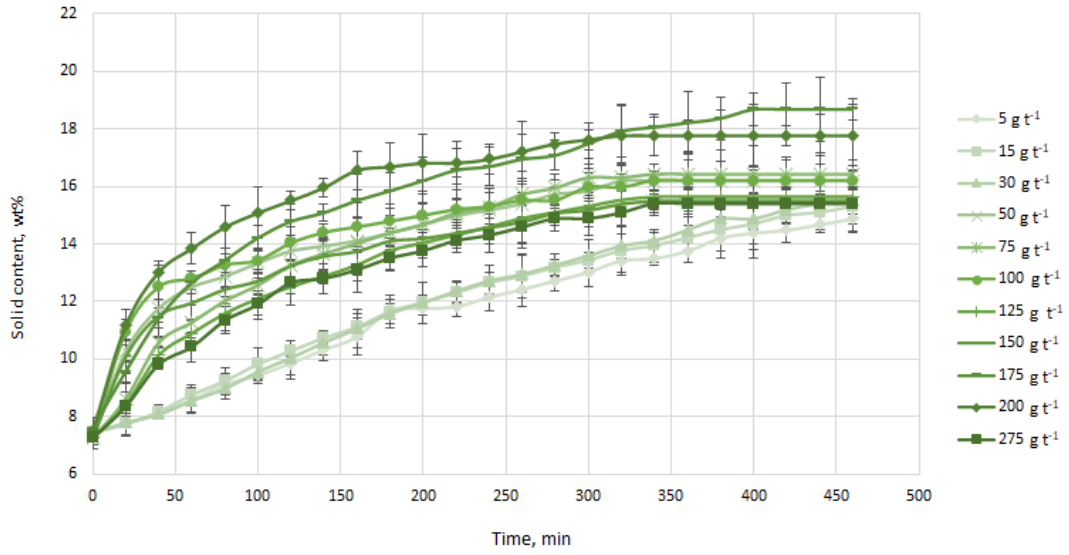

Figure 4. Solids content over time at different dosages of the anionic flocculant

It can be seen that, at high dosages, the solids content stagnates at around 17 % for both flocculant types. It is possible that there is an increase in the viscosity of the sediment due to the large amount of flocculant [28] causing trapping of water and decreasing the content of solids.

It can be seen that even at low dosages of the cationic flocculant except at 5 g t^{-1}, the content of solids exceeds 12 % at the time of 160 min (Figure 3.), whereas for the anionic flocculant (Figure 4.) this result occurs at 220 min, which indicates that the sedimentation rate at low dosages is higher for the cationic flocculant as compared to that for the anionic flocculant. It can be also observed that at the initial times and at high flocculant dosages the solids content increases faster for the anionic flocculant. This is possibly due for to the action mechanisms of each type of the flocculant as mentioned by Concha [29] and Diaz [25]. In the case of the anionic flocculant, covalent bonds and/or hydrogen bridges are formed between the particles and these flocculants are mainly used for concentrates and tailings of copper, lead, zinc, *etc.* On the other hand, cationic flocculants act in a very similar way as coagulants, which predominantly comprises neutralization of particle surface charges, rather than formation of bridges [30].

The thickening process provides concentration of a dilute pulp into a thickened pulp as solid particles settle under the influence of the force of gravity. In the sedimentation tests, the addition of flocculants directly affects the suspension properties, which can be identified by means of the sedimentation rate. Measurement proceeds from the time zero that represents the pulp sample after complete mixing and the beginning of the test until the pulp reaches the maximum compression point (critical point), at which the interface of the water-suspension meets with the interface of the sediment-suspension at a critical height so that the sedimentation ends. The sedimentation rates obtained from Figure 2. and initial tangent slopes are presented in Table 2.

Table 2. Sedimentation rates for the tests in which the highest solid content was achieved

Test	Rate, cm min^{-1}	σ, cm min^{-1}
No flocculant	0.040	0.964
Cationic Flocculant (50 g t^{-1})	0.143	0.991
Anionic flocculant (175 g t^{-1})	0.250	0.978

The sedimentation rate increased 3.5- fold with the flocculant addition to the pulp for the cationic flocculant at a dosage of 50 g t^{-1}, and 6.5-fold for the anionic flocculant at 175 g t^{-1}. The obtained results may be since the cationic flocculant destabilizes the charge of colloidal particles present in the pulp causing particle coagulation and consequently better agglomeration, while another possible cause is that the bonds formed by the anionic flocculant are not strong enough to allow preservation of the flocs over time.

The flocculant dosage difference for the tests resulting the highest solids contents is very high (125 g t^{-1} difference), which could be a determining point in the choice of the reagent, since the expenses that could be caused by the use of the anionic flocculant could be very high as compared to the those of the cationic flocculant.

4. CONCLUSIONS

Sedimentation of lithium carbonate was studied with the use of two flocculant types. For the maximum time studied (460 min), the highest obtained of solids was ~19 % at the use of the anionic flocculant (175 g t^{-1}) and ~17 % for the cationic flocculant (50 g t^{-1}). Therefore, it could be concluded that the best results are obtained with use of the cationic flocculant, because similar contents of final solids are obtained for the two flocculants but at hugely different dosages.

When working at 25 °C, the highest increase in the content of solids was ~11 %, obtained with the anionic flocculant (175 g t^{-1}). Also, the sedimentation rate for this flocculant was higher than that for the cationic flocculant (0.250 and 0.143 mm min^{-1}, respectively), with the disadvantage that the flocculant amount is 3.5-fold higher. From the economic point of view, it is more convenient to use the flocculant with a positive ionic base since it achieves results remarkably similar to the anionic one, but at a noticeably lower dosage.

Overall, it is shown that the use of flocculants is a great alternative to accelerate the processes of obtaining lithium carbonate by thickening in ponds. Still, it is necessary to investigate the behavior of other chemical compounds present in brines during this process.

Acknowledgements: Kevin Pérez acknowledge the infrastructure and support of Doctorado en Ingeniería de Procesos de Minerales of the Universidad de Antofagasta

REFERENCES

[1] Saldaña M, Ayala L, Torres D, Toro N. Global sensitivity analyses of a neural networks model for a flotation circuit. *Hemijska Industrija*. 2020;74(4):247-256 https://doi.org/10.2298/HEMIND20060523S

[2] Toro N, Briceño W, Pérez K, Cánovas M, Trigueros E, Sepúlveda R, Hernández P. Leaching of Pure Chalcocite in a Chloride Media Using Sea Water and Waste Water. *Metals*. 2019;9(7):780 https://doi.org/10.3390/met9070780

[3] Toro N, Pérez K, Saldaña M, Jeldres RI, Jeldres M, Cánovas M. Dissolution of pure chalcopyrite with manganese nodules and waste water. *Journal of Materials Research and Technology*. 2019 https://doi.org/10.1016/j.jmrt.2019.11.020

[4] Torres D, Pérez K, Trigueros E, Jeldres R, Salinas-Rodríguez E, Robles P, Toro N. Reducing-effect of chloride for the dissolution of black copper. *Metals (Basel)*. 2020;10(1) https://doi.org/10.3390/met10010123

[5] Pérez K, Toro N, Campos E, González J, Jeldres R, Nazer A, Rodriguez MH. Extraction of Mn from Black Copper Using Iron Oxides from Tailings and Fe2+ as Reducing Agents in Acid Medium. *Metals (Basel)*. 2019;9:1112 https://doi.org/10.3390/met9101112

[6] Toro N, Robles P, Jeldres R. Seabed mineral resources, an alternative for the future of renewable energy: A critical review. *Ore Geology Reviews*. August 2020:103699 https://doi.org/10.1016/j.oregeorev.2020.103699

[7] Toro N, Jeldres R, Órdenes J, Robles P, Navarra A. Manganese Nodules in Chile , an Alternative for the Production of Co and Mn in the Future — A Review. *Minerals*. 2020;10(674):1-19 https://doi.org/10.3390/min10080674

[8] Heelan J, Gratz E, Zheng Z, Wang Q, Chen M, Apelian D, Wang Y. Current and Prospective Li-Ion Battery Recycling and Recovery Processes. *Jom*. 2016;68(10):2632-2638 http://doi.org/10.1007/s11837-016-1994-y

[9] Maxwell P, Mora M. Lithium and Chile: looking back and looking forward. *Mineral Economics*. 2020;33(1-2):57-71 https://doi.org/10.1007/s13563-019-00181-8

[10] Pinna EG, Drajlin DS, Toro N, Rodriguez MH. Kinetic modeling of the leaching of LiCoO2 with phosphoric acid. *Journal of Materials Research and Technology*. 2020;9(6):14017-14028 https://doi.org/10.1016/j.jmrt.2020.09.109

[11] Donoso, F; Garay, V; Cantallopts J. *International Lithium Market and Its Potential in Chile*. Chile; 2017.

[12] Gruber PW, Medina PA, Keoleian GA, Kesler SE, Everson MP, Wallington TJ. Global lithium availability: A constraint for electric vehicles? *Journal of Industrial Ecology*. 2011;15(5):760-775 https://doi.org/10.1111/j.1530-9290.2011.00359.x

[13] U.S. Geological Survey. *Mineral Commodity Summaries 2020*.; 2020.

[14] Velásquez C, Cabrera V. Small-scale lithium production from brines. In: Lima, Perú; 2018:19-21.

[15] Lunde Seefeldt J. Lessons from the Lithium Triangle: Considering Policy Explanations for the Variation in Lithium Industry Development in the "Lithium Triangle" Countries of Chile, Argentina, and Bolivia. *Politics and Policy*. 2020;48(4):727-765.

[16] Chen QB, Ji ZY, Liu J, Zhao YY, Wang SZ, Yuan JS. Development of recovering lithium from brines by selective-electrodialysis: Effect of coexisting cations on the migration of lithium. *Journal of Membrane Science*. 2018;548(8):408-420 https://doi.org/10.1016/j.memsci.2017.11.040

[17] Miranda C. *Background for a Public Policy in Strategic Minerals: Lithium*. Chile; 2009.

[18] Boryta, Kullberg T. Production of lithium compounds directly from lithium containing brines, in: Google Patents. 2007;2(12).

[19] Jandová J, Dvořák P, Vu HN. Processing of zinnwaldite waste to obtain Li2CO3. *Hydrometallurgy*. 2010;103(1-4):12-18 https://doi.org/10.1016/j.hydromet.2010.02.010

[20] Taborga P, Brito I, Graber TA. Effect of additives on size and shape of lithium carbonate crystals. *Journal of Crystal Growth*. 2017;460(November 2016):5-12 https://doi.org/10.1016/j.jcrysgro.2016.12.001

[21] Han B, Anwar UI Haq R, Louhi-Kultanen M. Lithium carbonate precipitation by homogeneous and heterogeneous reactive crystallization. *Hydrometallurgy*. 2020;195(October 2019):105386 https://doi.org/10.1016/j.hydromet.2020.105386

[22] Riveros Zapata A, Ale Ruiz L, Lezama J, Erdmann E. Lithium carbonate production: Simulation using aspen plus. Salta, Argentina; 2018.

[23] Schoenmann, Hales, Bedell D. Strategies for instru-mentation and control of thickeners and other solid–liquid separation circuits. *Mineral Processing Plant Design, Practice, and Control*. 2002;2:2164-2173.

[24] Teerikoski S. *Optimal Control of Clarifier-Thickeners*. Uppsala, Sweden; 2017 http://uu.diva-portal.org/smash/get/diva2:1088256/FULLTEXT01.pdf

[25] Díaz J. Coagulants - organic and inorganic flocculants made from plants and scrap metal recycling, for the treatment of polluted water. *McKinsey Quarterly*. 2014;2(1):1-22.

[26] Elhaei R, Kharrat R, Madani M. Stability, flocculation, and rheological behavior of silica suspension-augmented polyacrylamide and the possibility to improve polymer flooding functionality. *Journal of Molecular Liquids*. 2021;322:114572 https://doi.org/10.1016/j.molliq.2020.114572

[27] Wilkomirsky I. Extraction and refining of non-ferrous metals: Lithium; Metallurgical engineering department, Universidad de Concepción, Concepción, Chile 2008:1-25.

[28] Salam AM, Örmeci B, Simms PH. Determination of optimum polymer dosage for dewatering of oil sands tailings using torque rheology. *Journal of Petroleum Science and Engineering*. 2021;197 (August 2020) https://doi.org/10.1016/j.petrol.2020.107986

[29] Concha F. Filtration and separation manual; Metallurgical engineering department, Universidad de Concepción, Concepción, Chile 2001;(January 2001):234-308.

SAŽETAK

Taloženje litijum karbonata korišćenjem flokulanata sa različitim jonskim bazama

Yam Morales[1], Nelson Herrera[1,2] i Kevin Pérez[1,3,4]

[1]*Metallurgical and Mining Engineering Department, Universidad Católica del Norte, Antofagasta 1270709, Chile*
[2]*Oulu Mining School, University of Oulu, Oulu 90570, Finland*
[3]*Faculty of Engineering and Architecture, Universidad Arturo Prat, Almirante Juan José Latorre 2901, Antofagasta 1244260, Chile*
[4]*Department of Chemical Engineering and Mineral Processes, Faculty of Engineering, Universidad de Antofagasta, Antofagasta 1270300, Chile*

(Stručni rad)

Litijum je postao metal od ogromnog interesa u celom svetu. Široka upotreba punjivih baterija za čitav niz primena podstakla je brzi rast potražnje za litijum karbonatom. Ovo jedinjenje se dobija kristalizacijom, reakcijom sa litijum hloridom (u rastvoru) uz dodavanjem natrijum karbonata. Niske stope taloženja u bazenima za isparavanje predstavljaju problem u procesu kristalizacije. Iz tog razloga, u ovom radu su izvršena ispitivanja sedimentacije minerala upotrebom dva tipa flokulanta sa različitim jonskim naelektrisanjem. Ispitivanja su izvedena na laboratorijskom nivou koristeći različite doze za svaki flokulant, a cilj istraživawa je bio postizanje povećanja asadržaja čvrstih materija u sedimentu. Anjonski flokulant je imao bolje performanse u poređenju sa kationnim flokulantom, povećavajući brzinu taloženja litijum karbonata do 6,5 puta. Međutim, slični sadržaji čvrstih materija dobijeni su upotrebom katjonskog flokulanta u dozi nižoj 3,5 puta, što ga čini flokulantom izbora sa ekonomskog stanovišta.

Ključne reči: tretman rastvora; anjonska flokulacija; katjonska flokulacija; obojeni metali; rudarstvo.

Ispitivanje uticaja mehaničke aktivacije smeše MgO-TiO_2 na sintezu magnezijum- titanata

Nataša G. Đorđević[1], Milica M. Vlahović[2], Sanja P. Martinović[2], Slavica R. Mihajlović[1], Nenad M. Vušović[3] i Miroslav D. Sokić[1]

[1]*Institut za tehnologiju nuklearnih i drugih mineralnih sirovina, Franše d'Eperea 86 Beograd, Srbija*
[2]*Univerzitet u Beogradu, Institut za hemiju, tehnologiju i metalurgiju, Njegoševa 12, Karnegijeva 4, Beograd, Srbija*
[3]*Univerzitet u Beogradu, Tehnički fakultet u Boru, Vojske Jugoslavije 12, Bor, Srbija*

Izvod

U ovom istraživanju izvršena je mehanička aktivacija smeše magnezijum oksida i titanijum dioksida u cilju ispitivanja mogućnosti mehanohemijske sinteze magnezijum titanata. Mehanička aktivacija (MA) je vršena tokom 1000 min u visokoenergetskom vibro mlinu sa torzionim oprugama i prstenastim radnim elementima. Nakon ovog vremena, analiza strukture difrakcijom X-zraka je ukazala na potpunu amorfizaciju smeše polaznih komponenti. U skladu sa uputstvom za upotrebu vibro mlina u smislu vremenskog ograničenja kontinualnog rada, eksperiment je prekinut nakon 1000 minuta aktivnog mlevenja. Nemogućnost sinteze magnezijum titanata objašnjava se suviše niskom negativnom vrednošću Gibsove energije od -25,8 kJ mol^{-1} (i pored teorijske mogućnosti da se reakcija odigra), kao i količinom energije unete u sistem tokom mehaničke aktivacije koja se pokazala nedovoljnom za dobijanje željenog proizvoda. Iako sinteza magnezijum titanata nije ostvarena, dobijeni su značajni rezultati koji identifikuju metode za dalje ispitivanje mogućnosti odvijanja mehanohemijskih reakcija zemnoalkalnih metala i titanijum dioksida.

Ključne reči: visokoenergetski vibro mlin; magnezijum titanat; amorfizacija; analiza difrakcijom X-zraka.

Dostupno na web stranici časopisa: https://www.ache-pub.org.rs/index.php/HemInd/article/view/773

STRUČNI RAD

UDK 666.962:542.057:542.22: 546.824

Hem. Ind. **75 (4)** 213-225 (2021)

1. UVOD

U oblasti ispitivanja mogućnosti dobijanja titanata zemnoalkalnih metala, postupak sinteze mehanohemijskim postupkom zauzima značajno mesto. Dobijanje kalcijum titanata je vršeno različitim metodama. Proučavani su nanoprahovi kalcijum-titanata ($CaTiO_3$) dobijeni mehanohemijskom metodom uz pomoć mikrotalasnog zračenja kalcijum-oksida i titan-dioksida, kao i njegove suspenzije uz dodatak akril-polietilen glikola [1]. Kalcijum titanat ($CaTiO_3$) sintetizovan je sagorevanjem izvora kalcijuma, ljuske jajeta patke, titanijum dioksida (A-TiO_2) i magnezijuma (Mg) [2]. U nekim radovima vreme mlevenja polaznih komponenti je iznosilo 10 do 50 h [3]. U radu Manafija i saradnika [4] metoda mehaničkog legiranja primenjena je za dobijanje kalcijum-titanata bez toplotne obrade. Praćena je mehanohemijska sinteza $CaTiO_3$ iz CaO–TiO_2 polazne smeše [5], ispitivanje mogućnosti mehanohemijske sinteze $CaTiO_3$ od različitih polaznih komponenata [6]. Doprinos ispitivanju mogućnosti dobijanja kalcijum titanata dali su i mnogi drugi autori [7-10]. Dobijanje barijum bizmut titanata mehanohemijskim postupkom je takođe detaljno proučavano [11]. Takođe su proučavani i kinetika dobijanja barijum titanata [12], uticaj grupisanja kristala na dobijanje tetragonalno-kubne transformacije čestica $BaTiO_3$ [13], izotermalno sinterovanje barijum cink titanata [14], kao i električna svojstva barijum titanata [15]. Sprovedena su i mnoga druga istraživanja koja se odnose na ovu tematiku, i to ispitivanje dielektričnih svojstava barijum titanata sinterovanog iz tribofizički aktiviranih prahova i praćenje mehanizama sinterovanja [16-18], ispitivanje evaluacije strukture dobijene intenzivnim mlevenjem sistema $2Bi_2O_3$ i $3TiO_2$ [19]. Proučavani su materijali dobijeni mehanohemijskim postupkom kao i veličine kristala i njihova piezoelektrična svojstva u funkciji od gustine dobijenog materijala [20-26]. Dobijanje $SrTiO_3$ i Sr_2TiO_4 u čvrstom stanju iz sistema $SrCO_3$–TiO_2 je prikazano u radu [27],

Autor za prepisku: Nataša Đorđević, Institut za tehnologiju nuklearnih i drugih mineralnih sirovina, Franše d'Eperea 86, Beograd
E-mail: n.djordjevic@itnms.ac.rs
Članak primljen: 2. aprila 2021; Članak prihvačen: 9. avgusta 2021; Članak publikovan: 22. avgusta 2021.
https://doi.org/10.2298/HEMIND210402022D

sinteza $SrTiO_{3-x}F_x$ sa fotokatalitičkim svojstvima [28], mehanohemijska sinteza i fotokatalitički efekat $SrTiO_3$ sa azotom kao aditivom [29-31].

U toku mehaničke aktivacije čvrstih materijala dolazi do transformacije i akumulacije saopštene mehaničke energije u obliku defekata kristalne rešetke što dovodi do porasta entalpije i entropije tretiranog sistema [32,33]. Prema svojim termodinamičkim karakteristikama, reakcije čija je promena Gibsove energije $\Delta G < 0$ imaju potencijal da se odigraju spontano ili uz početni dodatak energije u cilju premošćavanja energetske barijere [34]. Od svih zemnoalkalnih metala, magnezijum oksid ima najmanji potencijal za reakciju u čvrstoj fazi. Mehaničko aktiviranje polaznih komponenti u cilju dobijanja magnezijum titanata ispitivali su mnogi autori [35-41].

Očekivani ishod svih pretpostavljenih mehanohemijskih reakcija neutralizacije između oksida zemnoalkalnih metala i titanijum dioksida je sinteza odgovarajućih titanata. Poređenje rezultata sinteza postignutih mehanohemijskim postupkom i ustanovljene razlike mogu se pripisati međusobnim razlikama između tih metala. Kako pripadaju istoj grupi elemenata, međusobne elementarne razlike na nivou strukture osnovne čestice – atoma zemnoalkalnih metala utiču i na razlike između njihovih jedinjenja, kao i ponašanje tih jedinjenja u hemijskim reakcijama neutralizacije. U tom smislu, korisno je prikazati relevantne podatke koji opisuju ove razlike. Za hemijske reakcije između oksida zemnoalkalnih metala i titanijum dioksida u Tabeli 1 su dati osnovni hemijsko – termodinamički podaci kao i odgovarajuće konstante ravnoteže na temperaturi od 20 °C.

Tabela 1. Termodinamički podaci za hemijske reakcije zemnoalkalnih metala i titanijum dioksida na temperaturi od 20 °C (ΔH°_r–entalpija reakcije, ΔS°_r – promena entropije reakcije, ΔG°_r – promena Gibsove slobodne energije reakcije; K_r – konstanta ravnoteže reakcije) [42]

Table 1. Thermodynamic parameters of chemical reactions between alkaline earth metals and titanium dioxide at 20 °C (ΔH°_r– enthalpy of reaction, ΔS°_r– entropy change, ΔG°_r– Gibbs free energy of reaction; K_r– equilibrium constant) [42]

Reakcija	T / K	ΔH°_r / kJ mol^{-1}	ΔS°_r / J mol^{-1}	ΔG°_r / kJ mol^{-1}	K / dm^3 mol^{-1}
$BaO + TiO_2 = BaTiO_3$	293	-161,5	-12,69	-157,8	$1{,}31 \times 10^{28}$
$SrO + TiO_2 = SrTiO_3$	293	-135,6	3,02	-136,5	$2{,}10 \times 10^{24}$
$CaO + TiO_2 = CaTiO_3$	293	-80,7	5,28	-82,3	$4{,}64 \times 10^{14}$
$MgO + TiO_2 = MgTiO_3$	293	-26,6	-2,64	-25,8	$3{,}94 \times 10^{4}$

Na osnovu prikazanih termodinamičkih parametara, može se očekivati da će se sinteza magnezijum titanata, u poređenju sa titanatima ostalih zemnoalkalnih metala, najteže odigrati iako postoji potencijal za spontano dobijanje svih pomenutih titanata bez obzira na tehniku koja se primeni.

Cilj istraživanja prikazanih u ovom radu bio je pokušaj sinteze magnezijum titanata mahaničkom aktivacijom stehiometrijske smeše magnezijum oksida i titanijum dioksida korišćenjem raspoložive opreme, visokoenergetskog vibro mlina sa torzionim oprugama i prstenastim radnim elementima. Ideja je bila da se kinetika reakcije prati na osnovu rendgenostrukturne analize i hemijske analize koja bi služila za određivanje stepena sinteze.

2. EKSPERIMENTALNI DEO

Za eksperimentalna ispitivanja u ovom radu upotrebljen je magnezijum oksid, MgO, kao bazni reaktant i titanijum dioksid, TiO_2, kao kiseli reaktant. Korišćeni magnezijum oksid je proizvodnje MERCK (Nemačka), CAS No. [1309-48-4], kvaliteta *pro analysi,* a titanijum dioksid takođe proizvodnje MERCK (Nemačka), CAS No. [13463-67-7], kvaliteta *pro analysi.*

U cilju odvijanja mehanohemijske reakcije neutralizacije, izvršena je mehanička aktivacija sistema MgO-TiO_2.

Jednačina (1) prikazuje hemijsku reakciju koja bi mogla da se odigra u mehanohemijskom reaktoru tokom mehaničke aktivacije polaznih komponenti, dajući magnezijum titanat kao krajnji produkt

$$MgO(s) + TiO_2(s) \rightarrow MgO\text{-}TiO_2 \rightarrow MgTiO_3(s) \quad (1)$$

($MgO\text{-}TiO_2$ Intermedijarno jedinjenje)

Mehanička aktivacija obavljena je u trajanju od 1000 min u visokoenergetskom vibro mlinu, tip MH954/3 (proizvođač KHD Humboldt Wedag A.G., Nemačka), Slika 1.

Mlin je snabdeven ležištem sa horizontalno postavljenim zatvaračem. Cilindrična radna posuda od nerđajućeg čelika, dubine 40 mm i unutrašnjeg prečnika 170 mm poseduje radne elemente u vidu dva slobodna koncentrična prstena,

takođe od nerđajućeg čelika i ukupne mase 3 kg. Ovi prstenovi prenose energiju udarom i trenjem na materijal koji se tretira. Ispod tela mlina je pogonski mehanizam sa elastičnim vratilom, ekscentričnim zamajcem i torzionim oprugama, koji stvara rezonantne vibracije radne posude. Radni elementi, čija je masa neuporedivo veća od mase uzorka, vrše usitnjavanje i mehaničku aktivaciju materijala zahvaljujući vibracijama. Snaga motora je 0,8 kW. Optimalna količina praha koji se mehanički aktivira je 50-150 g.

Slika 1. Visokoenergetski vibro mlin MH954/3 (KHD Humboldt Wedag A.G., Nemačka)
Figure 1. High-energy vibration mill, type MH954/3 (KHD Humboldt Wedag A.G., Germany)

Imajući u vidu optimalnu količinu reaktanata koji mogu da se aktiviraju, kao i njihov stehiometrijski odnos prema pretpostavljenoj hemijskoj reakciji prikazanoj jednačinom (1), početne količine su iznosile 20,2 g MgO (0,5 mol) i 39,9 g TiO_2 (0,5 mol), odnosno ukupno 60,1 g.

U toku mehaničke aktivacije periodično su uzimani uzorci (po 1 g, nakon 60, 180, 330 i 1000 min) iz reakcionog sistema i vršena je njihova rendgenostrukturna analiza, kao i analiza trenutnog hemijskog sastava sistema. Hemijska analiza reaktanata i uzoraka iz reakcionog sistema tokom mehaničke reakcije vršena je metodom atomske apsorpcione spektrofotometrije na atomskom adsorpcionom spektrofotometru (AAS) Analyst 300 (proizvođač "Perkin Elmer"- SAD) pri čemu je kao rastvarač korišćen 10 % rastvor sirćetne kiseline (99,5 % glacijalna sirćetna kiselina, Zorka Pharma, Hemija – DOO, Srbija).

Rendgenostrukturna analiza reaktanata i uzoraka iz reakcionog sistema tokom mehaničke aktivacije vršena je na PHILIPS PW-1700 automatizovanom difraktometru (proizvođač "Philips", Holandija) sa bakarnom cevi koji radi na 40 kV i 35 mA. Uređaj je snabdeven grafitnim monohromatorom i proporcionalnim brojačem, napunjenim ksenonom. Korišćen je ugao snimanja (2θ) od 4 do 15°.

Na osnovu rezultata hemijske analize moguće je izračunati stepen reakcije sinteze prema jednačini (2):

$$S = \left(1 - \frac{0{,}25\left(c - bc_{\text{Ti}}\right)}{c_0 w}\right)100 \qquad (2)$$

gde je c sadržaj magnezijuma u rastvoru, c_0 - odvaga uzorka, - c_{Ti} sadržaj titanijuma u rastvoru, w - maseni udeo magnezijuma u polaznom sistemu MgO-TiO_2 koji iznosi w_{Mg}=0,2025, b - faktor ekvivalencije učešća magnezijuma u pretpostavljenom intermedijarnom jedinjenju stehiometrijskog sastava $MgTiO_3$ koji za sistem MgO-TiO_2 iznosi b_{Mg} = 0,5062.

Mehanohemijska aktivacija je u okviru eksperimentalne procedure obavljena jedanput, dok su uzorci za hemijsku analizu uzimana po 2 uzorka za analizu na atomskom adsorpcionom spektrofotometru (AAS) Analyst 300 (proizvođač "Perkin Elmer"- SAD) pri čemu je kao rastvarač korišćen 10 % rastvor sirćetne kiseline (99,5 % glacijalna sirćetna kiselina, Zorka Pharma, Hemija – DOO., Srbija).

3. REZULTATI I DISKUSIJA

3. 1. Karakterizacija reaktanata

U Tabeli 2 data je hemijska karakterizacija magnezijum oksida. Na osnovu podataka prikazanih u Tabeli 2, može se utvrditi da je sadržaj magnezijum oksida 97,0 %, da najveći udeo nečistoća potiče od karbonata (1,5 %), kao i da je gubitak žarenjem 2,0 %.

Tabela 2. Hemijski sastav magnezijum oksida
Table 2. Chemical composition of magnesium oxide

Komponenta	Sadržaj, %	Komponenta	Sadržaj, %
MgO (kompleksometrijski),minimalno	97,00	Kalcijum	0,0200
Supstance rastvorne u vodi, maksimalno	0,4	Bakar	0,0010
Supstance nerastvorne u HCl, maksimalno	0,005	Gvožđe	0,0050
Nečistoće, maksimalno		Kalijum	0,0050
Karbonati	1,5000	Mangan	0,0005
Hloridi	0,0100	Natrijum	0,2500
Sulfati	0,0010	Olovo	0,0010
Ukupni azot	0,0020	Cink	0,0005
Barijum i stroncijum	0,0050	Gubitak žarenjem, maksimalno	2,00
Arsen	0,0001	Supstance koje taloži NH_4OH, maksimalno	0,02

Rendgenostrukturna analiza magnezijum oksida prikazana je na Slici 2, dok su u Tabeli 3 date brojčane vrednosti položaja difrakcionih maksimuma karakterističnih za magnezijum oksid. Difraktogram na slici 2 prikazuje karakteristične pikove (odnosno difrakcione maksimume) za magnezijum oksid, a položaj difrakcionih maksimumia (vrednosti uglova) prikazani u Tabeli 3 ukazuju da je u analiziranom uzorku, pored dominantnog sadržaja magnezijum oksida, prisutan i zanemarljiv procenat nečistoća, što je potvrda rezultata hemijske analize.

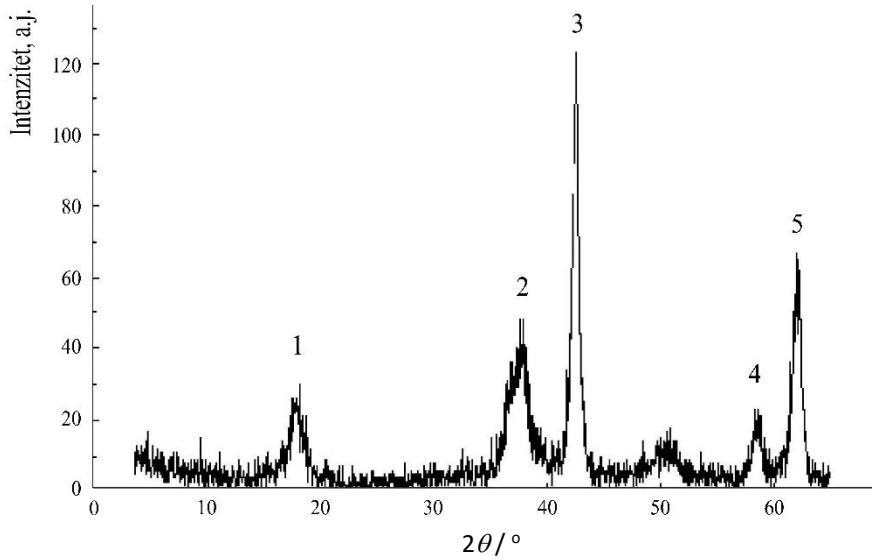

Slika 2. Rendgenostrukturna analiza magnezijum oksida
Figure 2. X-ray diffraction analysis of magnesium oxide

U Tabeli 4 prikazan je hemijski sastav upotrebljenog titanijum dioksida. Prikazani rezultati pokazuju da je sadržaj titanijum dioksida ≥99 %, sadržaj nečistoća rastvorljivih u vodi i hlorovodoničnoj kiselini ≤1 %, dok je gubitak žarenjem na 105 i 800 °C maksimalno 0,5 %.

Rendgenostrukturna analiza titanijum dioksida prikazana je na Slici 3, dok su u Tabeli 5 date vrednosti položaja difrakcionih maksimuma karakterističnih za titanijum dioksid. Na Slici 3 jasno su definisani pikovi karakteristični za titanijum dioksid što je očekivano s obzirom da su korišćenje supstance *p.a.* kvaliteta.

Tabela 3. Položaji karakterističnih difrakcionih maksimuma magnezijum oksida
Table 3. Position of characteristic diffraction maxima for magnesium oxide

Pik br.	*d* / nm*	2θ / °
1	0,48506	18,275
2	0,23796	37,775
3	0,21196	42,651
4	0,15792	58,390
5	0,14974	61,920

**d* – rastojanje između dve susedne ravni u kristalu

Tabela 4. Hemijski sastav titanijum dioksida
Table 4. Chemical composition of titanium dioxide

Komponenta	Sadržaj, %	Komponenta	Sadržaj, %
Sadržaj TiO_2, min	99	Kiselo rastvorni barijum	0,0002
Supstance rastvorne u vodi, max	0,5	Arsen	0,0001
Supstance nerastvorne u HCl, max	0,5	Gvožđe	0,0050
Nečistoće, max		Kiselo-rastvorno olovo	0,0010
Teški metali	0,0020	Cink	0,0005
Kiselo rastvorni antimon	0,0002	Gubitak žarenjem na 800 °C, max	0,5
Sulfati	0,0010	Gubitak sušenjem na 105 °C, max	0,5
Ukupni azot	0,0020		

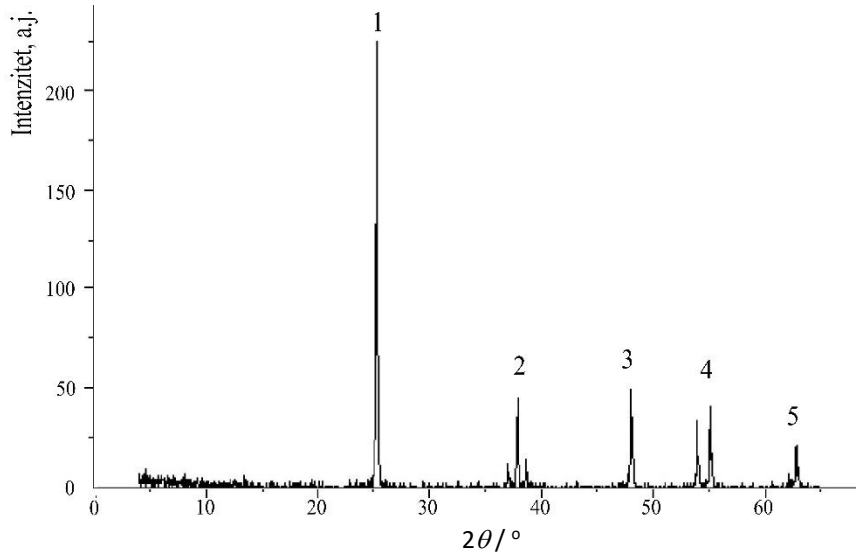

Slika 3. Rendgenostrukturna analiza titanijum dioksida
Figure 3. X-ray diffraction analysis of titanium dioxide

Tabela 5. Položaji karakterističnih difrakcionih maksimuma titanijum dioksida
Table 5. Position of characteristic diffraction maxima for titanium dioxide

Pik br.	*d* /·nm*	2θ / °
1	0,35133	25,330
2	0,23778	37,805
3	0,18926	48,035
4	0,16667	55,055
5	0,14806	62,700

**d* – rastojanje između dve susedne ravni u kristalu

Rezultati hemijske i rendgenostrukturne analize magnezijum oksida i titanijum dioksida, u prikazanim tabelama i dijagramima odgovaraju zahtevima koje moraju da ispune hemikalije kvaliteta *pro analysi* i kao takve su odgovarajuće komponente za reakciju koja se očekuje u eksperimentalnoj proceduri. Suština analiza bila je da se precizno kako hemijski tako i rendgenostrukturno utvrdi sastav polaznih supstanci, kako bi se pratilo ponašanje reaktanata tokom vremena aktivacije, kao i očekivani hemizam.

3. 2. Karakterizacija reakcionog sistema MgO-TiO_2 tokom mehaničke aktivacije

Dinamika mehaničkog tretmana reakcionog sistema MgO-TiO_2 praćena je rendgenostrukturnom analizom. Dobijeni difraktogrami uzoraka reakcionog sistema nakon 60, 180, 330 i 1000 min mehaničke aktivacije uporedno su prikazani na Slici 4, dok su vrednosti položaja karakterističnih difrakcionih maksimuma date u Tabeli 6.

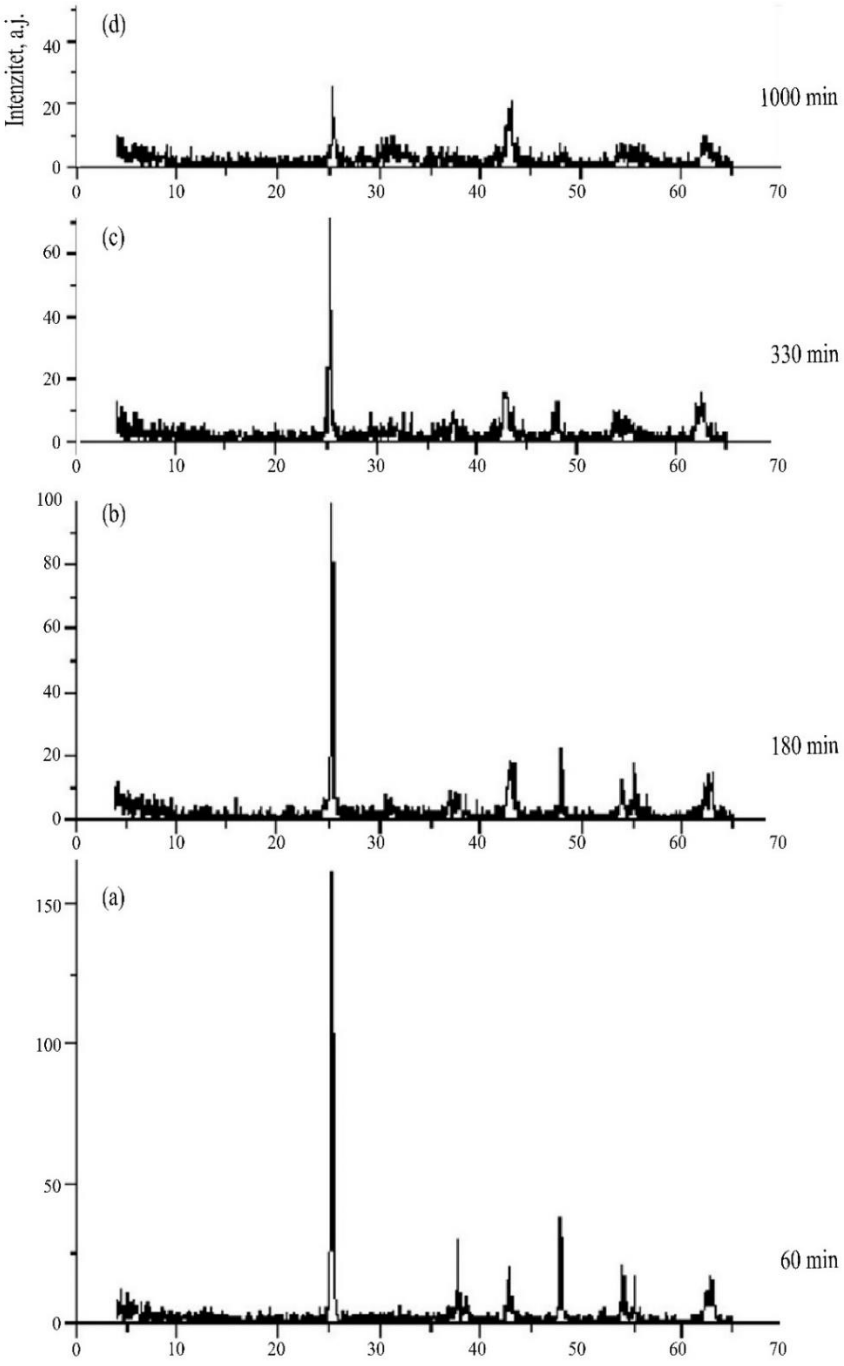

2θ / °

Slika 4. Rendgenostrukturna analiza uzorka sistema MgO-TiO_2 mehanički aktiviranog a) 60, b) 180, c) 330 i d) 1000 min

Figure 4. X-ray diffraction analysis of samples of the MgO-TiO_2 system mechanically activated for a) 60, b) 180, c) 330 i d) 1000 min

Tabela 6. Položaji karakterističnih difrakcionih maksimuma uzorka sistema MgO-TiO_2 posle 60, 180, 330 i 1000 min mehaničke aktivacije

Table 6. Position of characteristic diffraction maxima of the MgO-TiO_2 system sample after 60, 180, 330, and 1000 min of mechanical activation

Vreme aktivacije, min	Pik br.	Supstanca	d /·10^{-10} m*	2θ / °
60	1	TiO_2	0,35133	25,33
	2	TiO_2	0,23651	37,85
	3	MgO	0,21060	42,91
	4	TiO_2	0,18931	48,02
	5	TiO_2	0,16636	55,16
	6	MgO	0,14794	62,75
	Intenzitet preostalih 7 pikova je na nivou šuma.			
180	1	TiO_2	0,35093	25,360
	2	TiO_2	0,23766	37,825
	3	MgO	0,21078	42,870
	4	TiO_2	0,18931	48,020
	5	TiO_2	0,16657	55,090
	6	MgO	0,14910	62,215
	Intenzitet preostalih 9 pikova je na nivou šuma.			
330	1	TiO_2	0,35133	25,303
	2	TiO_2	0,23808	37,755
	3	MgO	0,21141	42,730
	4	TiO_2	0,18889	48,135
	5	MgO	0,14826	62,605
	Intenzitet preostalih 8 pikova je na nivou šuma.			
1000	1	TiO_2	0,35065	25,38
	2	TiO_2	0,23802	37,76
	3	MgO	0,21060	42,91
	4	TiO_2	0,18876	48,17
	5	MgO	0,14874	62,38

**d* – rastojanje između dve susedne ravni u kristalu

Smanjenje intenziteta i širenje difrakcionih maksimuma koji se javljaju na difraktogramima aktiviranih reakcionih smeša, Slika 4(a-d), ukazuju da dolazi do destrukcije materijala, unošenja defekata i nastanka velikih naprezanja unutar kristalne rešetke.

Difraktogram reakcione smeše posle 60 min aktivacije, Slika 4a, već pokazuje prisustvo amorfne strukture pošto se uočava smanjenje intenziteta karakterističnih pikova.

Sa produženjem vremena mehaničke aktivacije trend smanjenja intenziteta difrakcionih maksimuma se nastavlja, a zapaža se i njihovo širenje, pri čemu su obe pojave najizraženije posle 1000 min aktivacije, Slike 4 b,c,d. Ove promene izgleda difraktograma su najčešće posledica smanjenja veličine čestica i naprezanja rešetke.

Osnovni zaključak koji se može doneti analizom difraktograma na Slici 4 jeste da je mehaničkom aktivacijom sistema MgO-TiO_2 došlo do gotovo potpune amorfizacije reakcione smeše.

Jasno se raspoznaju maksimumi magnezijum oksida (d = 0,21060 i 0,14874 nm) kao i titanijum dioksida (d = 0,35065; 0,23802 i 0,18876 nm). Difrakcioni maksimumi magnezijum titanata nisu identifikovani.

Kako se može zaključiti, tokom ukupnog perioda mehaničke aktivacije analiziranog sistema uočavaju se samo karakteristični pikovi na određenim talasnim dužinama čiji su se intenziteti smanjivali sa porastom vremena, ali nije

došlo do pojave novih pikova. Ovo ukazuje da u posmatranom sistemu tokom aktivacije nisu nastupile očekivane hemijske promene, već samo strukturne kao rezultat rušenja kristalne rešetke pod uticajem unete mehaničke energije.

S obzirom na dobijene rezultate, pošto nije ostvarena sinteza očekivanog produkta, smatralo se da se daljim produžavanjem aktivacije sistema MgO-TiO_2 u raspoloživom mehanohemijskom reaktoru gubi smisao eventualne primene metode dobijanja magnezijum titanata pod ovakvim reakcionim uslovima, a sa druge strane dovodi u pitanje bezbednost zbog njegovog dugotrajnog neprekidnog rada, dalji eksperimentalni rad je obustavljen. Tokom izvršenih eksperimenata postignuti rezultati bili su dovoljni za analizu procesa koji se odigravao u mehanohemijskom reaktoru tokom vremena aktivacije.

Hemijskom analizom uzoraka reakcionog sistema konstatovano je prisustvo reaktanata u količini koja se nije menjala u odnosu na polaznu. Prema tome, na osnovu hemijske analize, konstatovano je da se proces sinteze nije odigrao. Stoga je mehanička aktivacija obustavljena posle 1000 min.

Na osnovu difraktograma i hemijske analize jasno je da je u prvih 1000 min mehaničke aktivacije reakcionog sistema MgO-TiO_2 detektovana prva faza procesa tokom koje dolazi do intenzivnog narušavanja kristalne strukture reaktanata koji su dovedeni skoro u potpuno amorfizovano stanje, ali da nije došlo do hemijske reakcije između reaktanata i pored mehaničke energije koja je dovedena sistemu tokom aktivacije.

Promena intenziteta difrakcionih maksimuma titanijum dioksida sa vremenom mehaničke aktivacije prikazana je na slici 5, dok su promene širina difrakcionih maksimuma date u Tabeli 7.

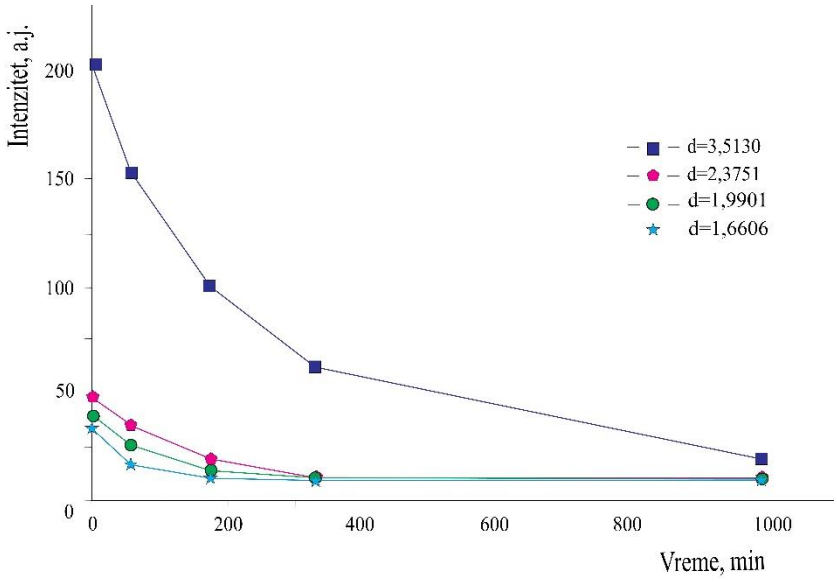

Slika 5. Zavisnost intenziteta difrakcionih maksimuma TiO_2 od vremena mehaničke aktivacije reakcionog sistema MgO-TiO_2
Figure 5. Intensity of TiO_2 diffraction maxima as a function of time of mechanical activation of the MgO-TiO_2 reaction system

Tabela 7. Širina difrakcionih maksimuma titanijum dioksida u funkciji od vremena mehaničke aktivacije
Table 7. Width of diffraction maxima of titanium dioxide as a function of mechanical activation duration

d /·nm*	Vreme, min				
	0	60	180	330	1000
	Širina difrakcionog maksimuma, °				
0,35130	0,080	0,160	0,080	0,100	0,080
0,23751	0,060	0,200	0,280	0,320	0,320
0,19901	0,120	0,080	0,100	0,280	0,480
0,16606	0,080	0,140	0,320	0,360	0,960

**d* – rastojanje između dve susedne ravni u kristalu

Na dijagramu Slike 5 uočljiv je pad intenziteta difrakcionih maksimuma gotovo do granica osetljivosti uređaja što je indikacija narušavanja kristalne strukture. S obzirom da na difraktogramu uzorka izloženog mehaničkoj aktivaciji tokom 1000 min, slika 4d), nije identifikovan maksimum očekivanog produkta reakcije, može se pretpostaviti da je celokupna reakciona masa, osim što je gotovo potpuno amorfizovana, takođe i nedefinisane hemijske strukture u pogledu zastupljenosti čvrstih i stabilnih hemijskih veza. Sa dijagrama se može zaključiti da se maksimalna promena intenziteta pikova odigrala na samom početku aktivacije što je posledica narušavanja kristalne strukture polaznih komponenti. Nakon 330 min aktivacije praktično nije došlo do bitnijih promena intenziteta pikova iz razloga što uložena mehanička energija nije bila dovoljna da se premosti energetska barijera ka formiranju novog hemijskog jedinjenja- magnezijum titanata i pored negativne vrednosti Gibsove energije i teorijske mogućnosti da se reakcija neutralizacije (1) odigra.

Analizom podataka iz Tabele 6, zaključuje se da širina difrakcionih maksimuma analiziranih uzoraka raste, što je takođe pokazatelj opisanih procesa.

Upoređujući difraktograme magnezijum oksida (Slika 2) i titanijum dioksida (Slika 3) sa difraktogramima aktivirnog reakcionog sistema (Slika 4), uočava se da su pikovi karakteristični za magnezijum oksid kao i titanijum dioksid prisutni na difraktogramima aktiviranog reakcionog sistema, ali sa smanjenim intenzitetom, što ukazuje na proces amorfizacije tokom mehaničke aktivacije.

Jasno je da se do prekida eksperimenta posle 1000 min mehaničke aktivacije odvijala prva faza, na difraktogramima vidljiva kao faza razaranja kristalne strukture reaktanata MgO i TiO_2 i njihovog prevođenja u amorfno stanje, ali očekivani produkt- magnezijum titanat nije nastao.

Reakcije u čvrstom stanju značajno su kompleksnije od reakcija koje se odigravaju u gasovitom i tečnom stanju. Pored termodinamičih parametara reakcije za koju se pretpostavlja da će se odigrati, na primer tokom procesa sinterovanja na tačno definisanoj teperaturi, višestruki parametri imaju uticaj na reakcije koje se očekuju usled mehaničkog delovanja na polazne komponente u stehiometrijskom odnosu. Pored teorijske mogućnosti da se pretpostavljena reakcija odigra (negativna Gibsova energija, što je slučaj u ovim eksperimentima, važnu ulogu ima i uređaj u kome se vrši mehanička aktivacija. U ovom slučaju korišćen je vibro mlin sa dva prstena mase 3 kg, koji na smešu prahova deluju silom trenja i udara, pa ne može da se govori o kontinualnom procesu. Uz to, sa povećanjem vremena mehaničke aktivacije raste temperatura sistema, čime se takođe menjaju parametri koji utiču na sistem. Kako u samom mlinu ne postoji oprema za praćenje sile kojom prstenovi deluju na zidove posude mlina, a time i na prahove, niti termometar, kojim bi se pratio porast temperature u funkciji vremena aktivacije i odredio trenutak kada mlevenje postaje temperaturno kontinualan proces, praktično je nemoguće na osnovu teorijskih parametara unapred utvrditi hoće li se i u kom stepenu u datom uređaju odigrati neka reakcija. Stoga je neophodno empirijski utvrditi da li je u datom reaktoru za određeno vreme aktivacije reakcija moguća. Iz tog razloga se i vrše periodična ispitivanja hemijskog sastava u određenim fazama mehaničke aktivacije da bi se utvrdilo postojanje pretpostavljenih intermedijarnih jedinjenja. Takođe se na osnovu hemijskog sastava određuje i trajanje mehaničke aktivacije, odnosno vreme potrebno da dođe do mehanohemijske reakcije. Tokom tog ispitivanja, u trenutku kada hemijska i rendgenostrukturna analiza pokažu da je očekivana reakcija završena i dobijen željeni produkt, mehanička aktivacija se završava.

Ključ za proučavanje i tumačenje kinetike mehanohemijskih reakcija je u uspostavljanju relacije između korisnog dela saopštene mehaničke energije i brzine hemijske reakcije. Pre nego što započne reakcija u čvrstom stanju između dve supstance koje se nalaze pod uticajem mehaničke energije, dolazi do rušenja kristalne strukture i pojave defekata u komponentama smeše. I pored toga što je predata mehanička energija obema supstancama (MgO i TiO_2) ista, obzirom da se radi o različitim jedinjenjima, sa sigurnošću se može tvrditi da kinetika rušenja kristalne rešetke nije ista za oba materijala. Stoga bi u cilju ispitivanja reakcije dobijanja magnezijum titanata bilo potrebno odvojeno pod istovetnim uslovima, uključujući i vreme trajanja, izvršiti mehaničku aktivaciju svakog od polaznih oksida pojedinačno, da bi se utvrdio mehanizam i kinetika uticaja aktivacije na svaku od komponenti. Takođe, obzirom da upotrebljenim vibro mlinom snage 0,8 kW nije unesena dovoljna količina energije u sistem da bi tokom 1000 min aktivacije započela hemijska reakcija, koja je teorijski moguća, trebalo bi izvršiti ispitivanje uticaja snage motora mlina na odvijanje reakcije. Ukoliko bi se koristio mlin sa kuglama, jedan od parametara bi bio i odnos mase kuglica u odnosu na masu prahova na kojima se vrši mehanička aktivacija.

Proizvodi mehaničke aktivacije u velikoj meri zavise od uslova mlevenja. S obzirom da tip mlina uz parametre mlevenja značajno utiče na efikasnost i prirodu prenosa mehaničke energije na tretirani materijal, primena različitih tipova mlinova ili varijacija parametara aktivacije može da rezultuje različitim tokovima mehanohemijskih reakcija. Stoga je realno očekivati da će mehaničkom aktivacijom sistema MgO-TiO_2 u nekom drugom tipu mlina doći do sinteze magnezijum titanata. Magnezijum titanat je moguće dobiti mehanohemijskom metodom u planetarnom mlinu [43]. S obzirom da fenomeni koji se dešavaju tokom mehaničke aktivacije nisu dovoljno proučeni, ne može se pouzdano predvideti finalni produkt tretmana.

Na slici 6 prikazana je promena potencijalne energije reaktanata, aktiviranog kompleksa i produkta tokom odvijanja hemijske reakcije.

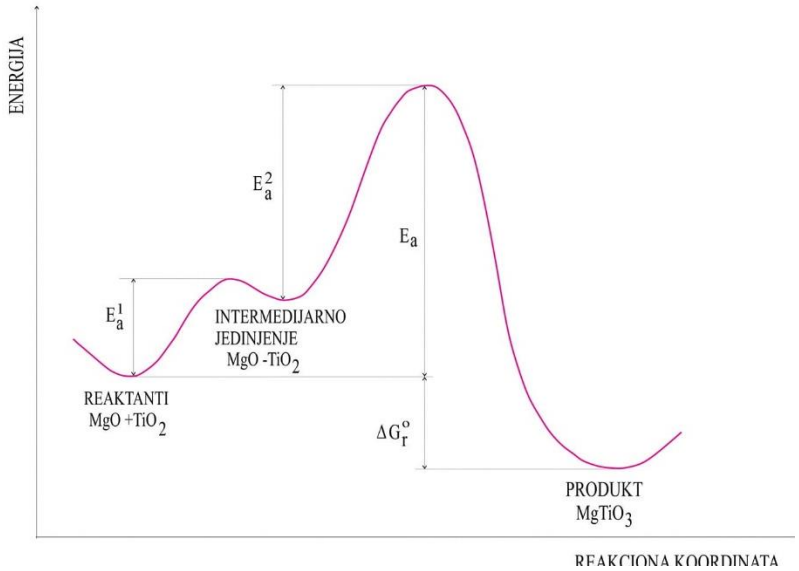

Slika 6. Promena potencijalne energije reaktanata, aktiviranog kompleksa i produkta duž reakcione koordinate.
Figure 6. Potential energy of reactants, activated complex and the product along the reaction coordinate

Na slici 6 prikazan je dijagram promene potencijalne energije polaznih komponenti koje se aktiviraju, očekivanog intermedijarnog jedinjenja i očekivanog produkta reakcije, magnezijum titanata. E_a^1 je energija potrebna da polazne komponente, usled unete mehaničke energije u sistem i narušene kristalne strukture međusobno počnu da reaguju i stvaraju hemijsku vezu formiranjem intermedijarnog jedinjenja (MgO-TiO_2) Daljim unosom energije u sistem (E_a^2) prevazišla bi se energetska barijera nakon čega bi bilo omogućeno neometano dobijanje konačnog proizvoda, magnezijum titanata. Ukupna aktivaciona energija E_a čini zbir ove dve energije ($E_a = E_a^1 + E_a^2$). Konačni produkt pretpostavljene reakcije nalazi se na energetskom nivou koji predstavlja negativni zbir energije unete u sistem (E_a) i promene Gibsove slobodne energije ($\Delta G_r°$).

Na osnovu dijagrama na Slici 6 vidi se da je razlika između potencijalnih energija reaktanata i produkta jednaka Gibbsovoj slobodnoj energiji reakcije (1) i iznosi, kako je navedeno u Tabeli 1, $\Delta G_r° = -25{,}8$ kJ mol^{-1}. Međutim, sa aspekta potencijalne energije reaktanata i aktiviranog kompleksa, vidi se da ako je odnos potencijalnih energija takav, kako je prikazano na slici 6, odnosno ako je $E_a^1 < E_a^2$, stepen odigravanja potencijalne reakcije svodi se na razliku u energijama aktivacije između dve potencijalne reakcije (usitnjavanje polaznih oksida, dobijanje intermedijarnog jedinjenja (MgO-TiO_2)), gde je potrebno dodatno ulaganje energije da bi nastalo konačno jedinjenje, magnezijum titanat. Primenjeno na konkretnu diskusiju o mehanizmu mehanohemijske sinteze magnezijum titanata, zaključuje se da je energija aktivacije prvog stupnja reakcije (1) manja od energije aktivacije drugog stupnja. Ta razlika utiče da je u eksponencijalnoj relaciji konstanta brzine drugog stupnja manja od konstante brzine prvog stupnja reakcije, što bi trebalo da rezultuje kinetičkim dijagramom reakcije prvog reda. Kako eksperimentom nije dobijeno pretpostavljeno intermedijaro jedinjenje, zaključuje se da primenjeni uređaj snage 0,8 kW nije mogao da preda sistemu potrebnu količinu energije E_a^1 i da se ni prvi stupanj reakcije nije odigrao.

Imajući u vidu prikazane vrednosti slobodne Gibsove energije, prema kojima je sintezu titanata ostalih zemnoalkalnih metala lakše ostvariti u odnosu na magnezijum titanat, dalja istraživanja će se izvršiti u vibro mlinu sa većom snagom motora i istim parametrima težine prstenova, kao i u planetarnom mlinu, a u funkciji odnosa mase kuglica i mase unetog materijala (MgO i TiO_2) u vidu smeše prahova, kako bi mehanička energija koju sistemu predaje primenjeni tip mlina bila dovoljna za prevazilaženje energetske barijere i za dobijanje magnezijum titanata.

4. ZAKLJUČAK

U ovom radu izvršen je pokušaj mehanohemijske sinteze magnezijum titanata u visokoenergetskom mlinu sa torzionim oprugama i prstenastim radnim elementima. Teorijski, hemijska reakcija je moguća samo ako je Gibsova slobodna energija te reakcije negativna, odnosno ako je energetski sadržaj produkata reakcije na nižem nivou od energetskog sadržaja reaktanata. Na osnovu rezultata dobijenih u ovom istraživanju može se zaključiti da i pored dovedene mehaničke energije u sistem, prisutna slobodna energija nije bila dovoljna da se odigra reakcija između MgO i TiO_2 i dobije magnezijum titanat kao produkt. Mehanička energija koja je predata reakcionom sistemu u mehano-hemijskom aktivatoru dovela je do rušenja kristalne strukture i amorfizacije reaktanata, što se vidi na prikazanim diftaktogramima, ali nije bila dovoljna za sintezu magnezijum titanata prema jednačini (1), pa bi u tom cilju bilo neophodno koristiti energetski jači uređaj koji bi polaznim komponentama predao veći sadržaj energije, čime bi se preskočila energetska barijera i omogućilo polaznim oksidima da uđu u hemijsku reakciju tokom mehaničke aktivacije.

Zahvalnica: Sredstva za realizaciju ovog istraživanja obezbedilo je Ministarstvo prosvete, nauke i tehnološkog razvoja Republike Srbije (451-03-9/2021-14/200023, 451-03-9/2021-14/200026 i 451-03-9/2021-14/200131).

LITERATURA

[1] Tyliszczak B, Gaca K, Sobczak-Kupiec A, Dulian P. Mechanochemical synthesis and investigations of calcium titanate powders and their acrylic dispersions. *J Eur Ceram Soc.* 2014; 34(10): 2259-2264.

[2] Cherdchom S, Rattanaphan T, Chanadee T. Calcium Titanate from food waste: Combustion Synthesis, Sintering, Characterization, and Properties. *Adv Mater Sci Eng.* 2019; 9639016.

[3] Fauzi F, Habieb AM, Noviyanto A, Kusumaningrum R, Sukmarani G, Muhammad E, Widodo V, Amalia D, Aryanto D, Rochman N. The Effect of Mechanochemical on The Formation of Calcium Titanate ($CaTiO_3$) Prepared by High Energy Milling. In: Proceedings of IOP Conference Series: Materials Science and Engineering, International Conference on Advanced Materials and Technology. Indonesia, Bogor, 2019, 924, pp. 8-9.

[4] Manafi S, Jafarian M. Synthesis of perovskite $CaTiO_3$ nanopowders with different morphologies by mechanical alloying without heat treatment. *Int J Phys Sci.* 2013; 8(23): 1277-1283.

[5] Guomin M, Murakami Y, Shindo D, Saito F. Mechanochemical synthesis of $CaTiO_3$ from a CaO–TiO_2 mixture and its HR-TEM observation. *Powder Technol.* 1999; 105(1–3): 162-166.

[6] Branković G, Vukotić V, Branković Z, Varela J. Investigation on possibility of mechanochemical synthesis of $CaTiO_3$ from different precursors. *J Eur Ceram Soc.* 2007; 27(2–3): 729-732.

[7] Palaniandy S, Jamil N. Influence of milling conditions on the mechanochemical synthesis of $CaTiO_3$ nanoparticles. *J Alloy Compd.* 2009; 476(1–2): 894-902.

[8] Tyliszczak B, Gaca K, Sobczak-Kupiec A, Dulian P. Mechanochemical synthesis and investigations of calcium titanate powders and their acrylic dispersions. *J Eur Ceram Soc.* 2014; 34(10): 2259-2264.

[9] Wieczorek-Ciurowa K, Dulian P, Nosal A, Domagała J. Effects of reagents nature on mechanochemical synthesis of calcium titanate. *J Therm Anal Calorim.* 2010; 101(2): 471–477.

[10] Ralphs K, Hardacreand C, James S. Application of heterogeneous catalysts prepared by mechanochemical synthesis. *Chem Soc Rev*. 2013; 42: 7701-7718.

[11] Lazarević Z, Bobić J, Romčević N, Paunović N, Stojanović B. Study of Barium Bismuth Titanate Prepared by Mechanochemical Synthesis. *Sci Sinter.* 2009; 41: 329-335.

[12] Đorđević N, Obradović N, Filipović S. Kinetika mehanohemijske sinteze barijum-titanata, *Tehnika*. 2011; 66(3): 367-371.

[13] Li X, Shih W. Size Effects in Barium Titanate Particles and Clusters. *J Am Ceram Soc.* 1997; 80(11): 2844-2852.

[14] Obradović N, Filipović S, Pavlović V, Mitrić M, Marković S, Mitić V, Đorđević N, Ristić M. Isothermal sintering of barium-zinc-titanate ceramics. *Ceram Int.* 2011; 37(1): 21-27.

[15] Pavlović V, Nikolić M, Nikolić Z, Branković G, Živković Lj, Pavlović V, Ristić M. Microstructural evolution and electric properties of mechanically activated $BaTiO_3$ ceramics. *J Eur Ceram Soc.* 2007; 27(2-3): 575-579.

[16] Stojanović B, Pavlović V, Pavlović VP, Đurić S, Marinković B, Ristić M. Dielectric properties of barium-titanate sintered from tribophysically activated powders. *J Eur Ceram Soc.* 1999; 19 (6-7): 1081-1083.

[17] Tkacova K. *Mechanical activation of minerals*. Amsterdam, New York, Elsevier; 1989.

[18] Yangyun S, Brook RJ. Mechanism of reactive sintering of aluminium nitride. *Sci Sinter*. 1985; 17: 35-47.

[19] Zdujic M, Poleti D, Jovalekic C, Karanovic L. The evolution of structure induced by intensive milling in the system 2Bi(2)O(3) center dot 3TiO(2). *J Non-Cryst Solids*. 2006; 352(28-29): 3058-3068.

[20] Bobić J, Vijatović M, Rojac T, Stojanović B. Characterization and properties of barium bismuth titanate. *Process Appl Ceram.* 2009; 3(1-2): 9–12.

[21] Stojanovic B, Paiva-Santos C, Cilense M, C. Valekic J, Lazarevic Z. Structure study of $Bi_4Ti_3O_{12}$ produced via mechanochemically assisted synthesis. *Mater Res Bull*. 2008; 43: 1743–1753.

[22] Kudłacik-Kramarczyk S, Drabczyk A, Głąb M, Dulian P, Bogucki R, Miernik K, Sobczak-Kupiec A, Tyliszczak B. Mechanochemical Synthesis of $BaTiO_3$ Powders and Evaluation of Their Acrylic Dispersions. *Materials*. 2020; 13(15): 3275.

[23] Buscaglia V, Randall C. Size and scaling effects in barium titanate. *J Eur Ceram Soc*. 2020; 40: 3744–3758.

[24] Barber P, Balasubramanian S, Anguchamy Y, Gong S, Wibowo A, Gao H, Ploehn H, Loye H. Polymer Composite and Nanocomposite Dielectric Materials for Pulse Power Energy Storage. *Materials*. 2009; 2:1697–1733.

[25] Wei X, Liu Y, Zhao D, Ge S. 3D printing of piezoelectric barium tinatate with high density from milled powders. *J Eur Ceram Soc*. 2020; 40(15): 5423-5430

[26] Ziegmann A, Schubert D. Influence of the particle size and the filing degree of barium titanate filled silicone elastomers used as potential dielectric elastomers on the mechanical properties and the crosslinking density. *Mater Today Commun*. 2018; 14: 90–98.

[27] Berbenni V, Mariniv A, Bruni G. Effect of Mechanical Activation on the Preparation of $SrTiO_3$ and Sr_2TiO_4 Ceramics from the Solid State Systems $SrCO_3$–TiO_2. *J Alloy Compd.* 2001; 329(1–2): 230–238.

[28] Wang J, Yin S, Zhang Q, Saito F, Sato T. Mechanochemical synthesis of $SrTiO_{3-x}F_x$ with high visible light photocatalytic activities for nitrogen monoxide destruction. *J Mater Chem.* 2003; 13: 2348-2352.

[29] Wang J, Yin S, Zhang Q, Saito F, Sato T. Mechanochemical Synthesis and Photocatalytic Activity of Nitrogen Doped $SrTiO_3$. *J Ceram Soc Jpn.*, 2004; 112(5): 1408-1410.

[30] Živojinović J, Pavlović V, Kosanović D, Marković S, Krstić J, Blagojević V, Pavlović V. The influence of mechanical activation on structural evolution of nanocrystalline $SrTiO_3$ powders. *J Alloy Compd.* 2017; 695: 863-870.

[31] Wang TX, Liu SZ, Chen J. Molten salt synthesis of $SrTiO_3$ nanocrystals using nanocrystalline TiO_2 as a precursor. *Powder Technol*. 2011; 205: 289–291.

[32] Avvakumov EG. *Mekhanicheskie metody aktivacii khimicheskih procesov*, Moskva, SSSR, Akademii Nauk; 1986.

[33] Boldyrev VV. Mechanochemistry and mechanical activation of solids. *Solid State Ionics*, 1993; 63-65: 537-543.

[34] Glasstone S. *Textbook of Physical Chemistry*. Lancaster, PA Lancaster Press; 1967.

[35] Filipovic S, Obradovic N, Pavlović V, Markovic S, Mitrić M, Ristic M. Influence of Mechanical Activation on Microstructure and Crystal Structure of Sintered MgO-TiO2 System. *Sci Sinter*. 2010; 42(2): 143-151.

[36] Filipovic S, Obradovic N, Kosanovic D, Pavlovica V, Djordjevic A. Sintering of the mechanically activated MgO-TiO2 system. *J Ceram Process Res*. 2013; 14(1): 31-34.

[37] Nikzad L, Ghofrani S, Majidian H, Ebadzadeh T. Effect of Ball Milling on Reactive Microwave Sintering of MgO-TiO2 System. *ACERP*. 2016; 2(3): 25-28.

[38] Khalajabadi S, Rafiq M, Kadir A, Izman S, Bakhsheshi-Rad H, Farahany S. Effect of mechanical alloying on the phase evolution, microstructure and bio-corrosion properties of a Mg/HA/TiO2/MgO nanocomposite. *Ceram Int*. 2014; 40(10): 16743-16759.

[39] Bhuyan R, Sahoo P, Basanta K, Sarangi A. Structural and Thermal Study of Mg2TiO4 Nanoparticles Synthesized by Mechanical Alloying Method. *Micro Nanosyst*. 2020; 12(2): 87-91.

[40] Yang H, Zhihong L, Yumei Z. Effect of MgO–TiO2–SiO2 additions on in-situ anisotropic grains growth and mechanical properties of corundum abrasive using pseudo-boehmite as raw material. *Ceram Int*. 2020; 46 (2): 1934-1939.

[41] Khalajabadi S, Kadir M, Izman S, Yusop M. Facile fabrication of hydrophobic surfaces on mechanically alloyed-Mg/HA/TiO2/MgO bionanocomposites. *Appl. Surf. Sci*. 2015; 324: 380-392.

[42] Vidojković V. *Proučavanje mehanizma i kinetike mehanohemijske sinteze neorganskih soli kod reakcija neutralizacije*. Doktorska disertacija, Univerzitet u Beogradu; 2001.

[43] Filipović S, Obradović N, Pavlović V, Marković S, Mitrić M, Mitrović N. Sinteza magnezijum titanata mehanohemijskom metodom. *Tehnika*. 2014; 23 (5): 727-731.

ABSTRACT

Investigation of the impact of mechanical activation on synthesis of the MgO-TiO_2 system

Nataša G. Đorđević[1*], Milica M. Vlahović[2], Sanja D. Martinović[2], Slavica R. Mihajlović[1], Nenad M. Vušović[3] and Miroslav D. Sokić[1]

[1]*Institute for Technology of Nuclear and Other Mineral Raw Materials, Belgrade, Serbia*
[2]*University of Belgrade, Institute of Chemistry, Technology and Metallurgy, Belgrade, Serbia*
[3]*University in Belgrade, Technical Faculty in Bor, Bor, Serbia*

(Technical paper)

In this study, a mixture of magnesium oxide and titanium dioxide was mechanically activated in order to investigate the possibility of mechanochemical synthesis of magnesium titanate. Mechanical activation was performed for 1000 min in a high-energy vibro mill (type MH954/3, KHD Humboldt Wedag AG, Germany). The mill is equipped with housing having a horizontally placed shutter. The cylindrical stainless steel working vessel, with inner dimensions of 40 mm in height and 170 mm in diameter, has working elements consisting of two free concentric stainless steel rings with a total weight of 3 kg. The engine power is 0.8 kW. Respecting the optimal amount of powder to be activated of 50-150 g and the stoichiometric ratio of the reactants in the equation presenting the chemical reaction of magnesium titanate synthesis, the starting amounts were 20.2 g (0.5 mol) of MgO and 39.9 g (0.5 mol) TiO_2. During the experiments, X-ray diffraction analysis of the samples taken from the reaction system after 60, 180, 330, and 1000 min of mechanical activation was performed. Atomic absorption spectrophotometry was used for chemical composition analysis of samples taken at different activation times. Based on the X-ray diffraction analysis results, it can be concluded that the greatest changes in the system took place at the very beginning of the mechanical activation due to the disturbance of the crystal structure of the initial components. X-ray diffraction analysis of the sample after 1000 min of activation showed complete amorphization of the mixture, but diffraction maxima characteristic for magnesium titanate were not identified. Therefore, the mechanical activation experiments were stopped. Evidently, the energy input was not sufficient to overcome the energy barrier to form a new chemical compound - magnesium titanate. The failure to synthesize magnesium titanate is explained by the low negative Gibbs energy value of -25.8 kJ/mol (despite the theoretical possibility that the reaction will happen), as well as by the amount of mechanical energy entered into the system during activation which was insufficient to obtain the reaction product. Although the synthesis of $MgTiO_3$ was not achieved, significant results were obtained which identify models for further investigations of the possibility of mechanochemical reactions of alkaline earth metals and titanium dioxide.

Keywords: high energy vibrating mill; magnesium titanate; amorphization; X-ray structural analysis

Study of microstructure, hardness and thermal properties of Sn-Bi alloys

Kristina N. Božinović, Dragan M. Manasijević, Ljubiša T. Balanović, Milan D. Gorgievski, Uroš S. Stamenković, Miljan S. Marković and Zoran D. Mladenović

Technical Faculty in Bor, Department of Metallurgical Engineering, University of Belgrade, Vojske Jugoslavije 12, 19210 Bor, Serbia

Abstract

Lead-free solders have become a main focus of the electronic industry in recent years, because of the high toxicity of lead. Alloys based on the Sn-Bi system figure as potential replacements for Sn-Pb alloys in soldering due to favorable properties and low cost. One of the main advantages of these alloys are low melting temperatures, while additional advantages include good compatibility with substrates, low process temperature, high reliability, and potential applications in conjunction with reduced graphene oxide nanosheets as thermal interface materials. In this paper, characterization of microstructural and thermal properties as well as hardness measurements of seven alloys of different Sn-Bi compositions are performed. Structural properties of the samples were analyzed using optical microscopy and scanning electron microscopy and energy dispersive X-ray spectroscopy (SEM-EDS). Thermal conductivity of the samples was investigated using the xenon-flash method, and phase transition temperatures were measured using the differential scanning calorimetry (DSC) analysis.

Keywords: structural properties; soldering; lead-free solders; thermal conductivity.

Available on-line at the Journal web address: http://www.ache.org.rs/HI/

ORIGINAL SCIENTIFIC PAPER

UDC: 620.17:669.017.12 (546.811+546.87)

Hem. Ind. **75 (4)** 227-239 (2021)

1. INTRODUCTION

For a long time, lead-tin alloy was broadly used in electronic industry because of its favorable physical and mechanical characteristics (low melting point, good wettability on different substrates, high strength of joints), and well-studied and optimized production [1]. Because of the high toxicity of lead, this alloy was abandoned, which prompted the electronics industry to seek for new solutions and lead-free solders became one of the main interests. A variety of systems have been proposed such as Sn-Ag, Sn-Cu, Sn-Bi, Sn-Zn, Sn-Au, Sn-Ag-Cu (SAC), Sn-Bi-Zn, Sn-Ag-Cu-Bi, etc. [2-5]. Commonly used in wave and reflow soldering processes, many of these lead-free solders melt at much higher temperatures than the conventional Sn-Pb eutectic solder (183°C). Higher melting temperatures cause damage to high-temperature-sensitive components and pose a major challenge to the electronic industry [4-5]. Alloys based on the Sn-Bi system were proposed as one of the best candidates in replacing Sn-Pb alloys in soldering due to their low melting temperatures (eutectic point: 139°C), good mechanical properties and cost-efficiency [1,5-8]. Yet, Sn-Bi solder alloys have also disadvantages, such as precipitation of Bi in the supersaturated Sn matrix during aging, and coarsening of the microstructure in the case of Bi-rich phases [9,10]. Therefore, a considerable number of investigations have been devoted to examining microstructure and mechanical properties of Sn-Bi alloys with addition of alloying elements such as Ni, Cu, Zn, Ag [5,6,9-14]. These systems with addition of other components also, have been particularly researched because of their potential application as thermal interface materials (TIM). The increasing demand for higher processing speeds, and smaller and thinner products had led the electronic industry to develop high performance devices, leaving a thermal management as a main challenge. In microelectronic packaging, TIM acts as a tunnel for the heat transfer from the device to the heat sink. Simultaneously, it provides a mechanical connection. The efficiency of the thermal management system is largely limited by the thermal conductivity of the TIM. Sn-Bi alloys reinforced with carbon

Corresponding author: Kristina N. Božinović, Technical Faculty in Bor, Department of Metallurgical Engineering, University of Belgrade, Vojske Jugoslavije 12, 19210 Bor, Serbia; tel. +381 61 613 12 95

E-mail: kbozinovic@tfbor.bg.ac.rs

Paper received: 19 January 2021; Paper accepted: 09 July 2021; Paper published: 30 July, 2021

https://doi.org/10.2298/HEMIND210119021B

nanotubes, reduced graphene oxide nanosheets, and other supplements have become very attractive as TIMs, because of their relatively low process temperatures, high reliability, and good compatibility with substrates [15-18].

In recent years, research of Sn-Bi system properties has been mainly focused on microstructure [9,19-24], mechanical properties [9,12,13,20-23], wettability [25,26], thermal characteristics [20,27], and interfacial reactions between the molten solder and the substrate [24,28], considering primarily the Sn-Bi eutectic alloy. Very little to none attention was given to the thermal conductivity [20,29] and hardness measurements. Therefore, this work focused on microstructure characterization, hardness measurements, and thermal properties investigations as a contribution to more complete knowledge of the mentioned system. These investigations included determination of thermal diffusivities and thermal conductivities of seven Sn-Bi alloys with different compositions.

2. EXPERIMENTAL

The metals used for the preparation of selected samples were bismuth and tin of >99.9 % purity (Alfa Aesar, United States). The investigated alloys with bismuth molar fractions of 0.1; 0.2; 0.4; 0.5; 0.6; 0.8 and 0.9 were prepared by melting weighted masses of pure metals in alumina crucibles under inert argon atmosphere at 400°C. The investigated compositions are given in Table 1.

Table 1. Molar and mass compositions of investigated Sn-Bi alloys

	x		Content, mas.%	
Sample	**Bi**	**Sn**	**Bi**	**Sn**
Alloy 1	0.1	0.9	16.36	83.64
Alloy 2	0.2	0.8	30.56	69.44
Alloy 3	0.4	0.6	53.99	46.01
Alloy 4	0.5	0.5	63.77	36.23
Alloy 5	0.6	0.4	72.53	27.47
Alloy 6	0.8	0.2	87.56	12.44
Alloy 7	0.9	0.1	94.06	5.97

After solidification of alloy ingots, they were further homogenized for 60 min at 120 °C and cut into two parts. A smaller part of the sample was used for differential scanning calorimetry (DSC) analysis, and the remaining part was pressed by a hydraulic press (Mohr-Federhaff-Losenhausen, Germany) to obtain samples of the same dimensions in form of a tablet 12.7 mm in diameter and about 2 mm thick. The pressing force was 7000 N.

Annealing was performed after pressing in order to remove internal stresses created during the pressing. The annealing was carried out at 100 °C, in a closed chamber furnace, in a nitrogen-protected atmosphere, for 6 h.

Pressed and annealed samples were then used for investigations of thermal conductivity and diffusivity, structural analyses, and hardness measurements.

The samples were prepared for the microstructural investigation *via* three steps: grinding, polishing and structure development. In the structure development step, different etching agents were used, depending on the composition (5 % alcoholic solution of hydrochloric acid – 5 % HCl in C_2H_5OH; A solution of ferric chloride in water - $FeCl_3$ + HCl in H_2O; concentrated nitric acid - conc. HNO_3; 8 % hydrochloric acid solution in alcohol – 8 % HCl in C_2H_5OH). All chemicals used as etching agents were GR graded and produced by Dispochem.

Investigation of microstructural properties was performed by using light optical microscopy (LOM, Carl Zeiss Jena Epy Type 2 microscope, Zeiss, Germany) as well as by scanning electron microscopy and energy dispersive X-ray spectroscopy (SEM-EDS, VEGA 3, TESCAN, USA). Phase transition temperatures were measured by using the DSC analysis (SDT-Q600 Simultaneous TGA/DSC, TA Instruments, Germany), and thermal conductivities of the investigated alloys were determined by using the xenon-flash method on TA Discovery Xenon Flash (DXF) 500 instrument (TA Instruments, Germany). The experimental procedure is explained in detail in the previous paper [30].

The investigation of hardness was also carried out using Brinell's method (HPO 250, WPM Leipzig, Germany) with the applied force of 50 N. The measurements were performed at three different points of the sample surface, and the mean value was calculated.

Thermal analysis was conducted on the DSC/DTA/TGA simultaneous device TA SDT Q600 (TA Instruments, Germany). The specimens with an approximate weight of 40 mg were heated to 350 °C under inert argon atmosphere, at a constant rate of 5 °C/min. The onset temperature of the first DSC peak in the heating process was considered as the temperature of the eutectic reaction, and the peak temperature of the second thermal effect on heating was selected as the liquidus temperature.

3. RESULTS AND DISCUSSION

3. 1. Results of LOM and SEM-EDS analysis

The samples were prepared *via* three steps: grinding, polishing and structure development and afterwards examined by using the optical microscope (Fig. 1).

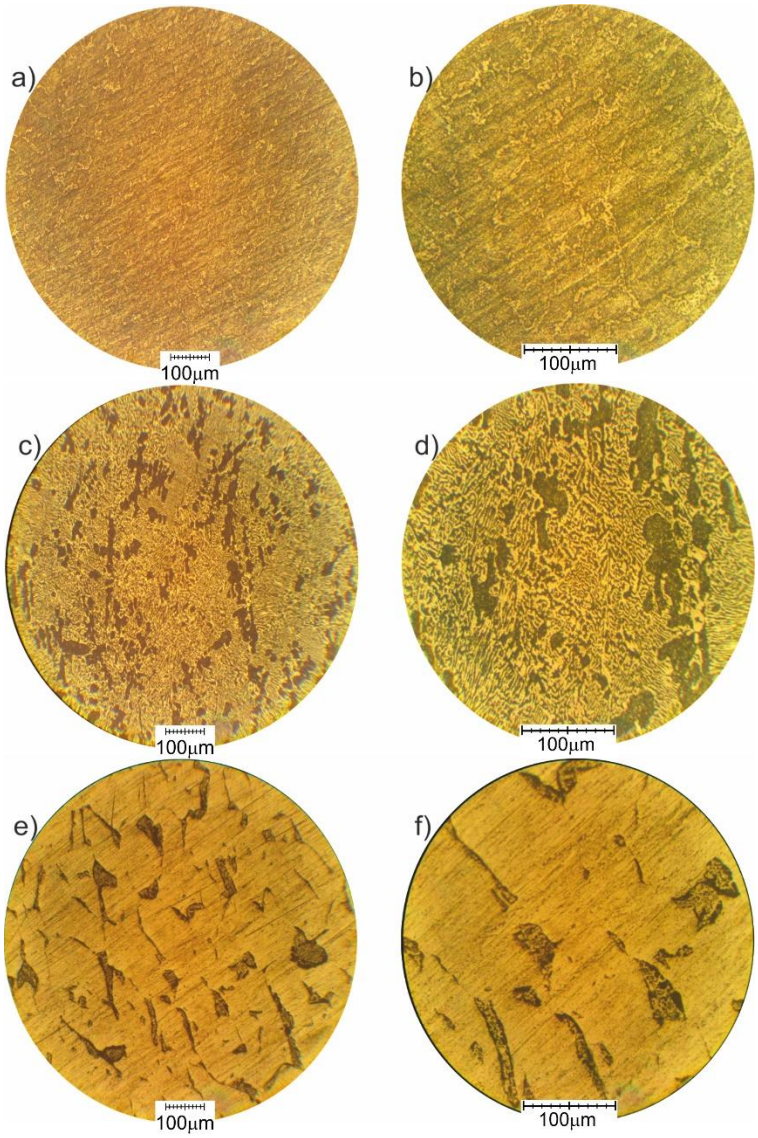

Fig. 1. Optical micrographs of chosen samples: (a) Alloy 2 magnification 200×; (b) Alloy 2 magnification 500×; (c) Alloy 3 magnification 200×; (d) Alloy 3 magnification 500×; (e); Alloy 7 magnification 200×; (f) Alloy 7 magnification 500×

Existence of two phases can be distinguished in the presented results as well as by the SEM-EDS analysis (Fig. 2). In Figure 1 darker areas correspond to the phase richer in tin and brighter to the phase richer in bismuth. However, in Figure 1c and d the eutectic mixture present in the microstructure can be observed. SEM-EDS analysis was used to analyze the phase morphology, to identify the coexisting phases, and to determine sample compositions (both overall and phase compositions).

For the alloys analyzed by using SEM (Fig. 2), co-existing phases in the microstructure were confirmed by the EDS point analysis. In the obtained SEM micrographs presented in Figures 3, 4 and 5 the darker colour signifies the phase richer in the lighter metal tin, and the brighter colour, on the other hand, corresponds to the phase richer in the heavier metal bismuth.

In this case, the existence of two phases is explained by the presence of a solid solution based on bismuth and a solid solution based on tin, which was confirmed by the EDS analysis.

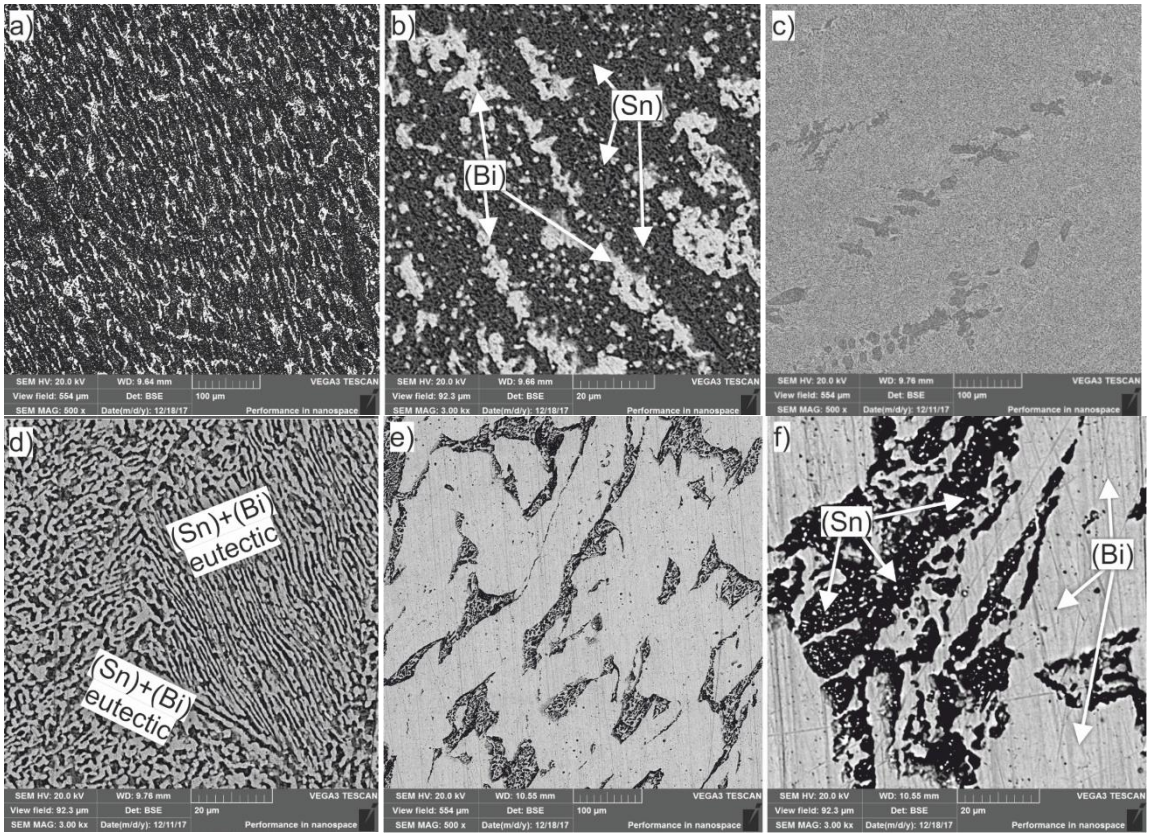

Fig. 2. SEM micrographs of examined samples - mixture of light (Bi) and dark (Sn) phases: a) Alloy 2 magnification 500×; (b) Alloy 2 magnification 3000×; (c) Alloy 3 magnification 500×; (d) Alloy 3 magnification 3000×; (e) Alloy 6 magnification 500×; (f) Alloy 6 magnification 3000×

We performed two types of the EDS analysis: 1) testing the overall composition of the observed surface and 2) examining the composition at individual points or spectrums on the surface.

Numerical values obtained by both types of EDS analysis, shown as atomic percentages of investigated components, are shown in Tables 2, 3 and 4, for each sample individually. Figure 3 shows microstructure of the Sn-rich sample, the alloy 2 (Bi0.2Sn0.8) subjected to the SEM-EDS analysis where Figure 3a shows the surface at which the overall composition was determined while Figure 3b shows particular points at which individual spectrums were obtained.

As it is shown in Figure 3b and in Table 2, darker phase represents the phase rich in tin solid solution (spectra 3 and 4), and lighter phase represents the phase rich in bismuth solid solution (spectra 1 and 2). In dark regions Sn-rich dendrites with Bi precipitates inside can be seen. A good agreement between the overall composition of the investigated surface and the nominal composition of the alloy 2 is obtained.

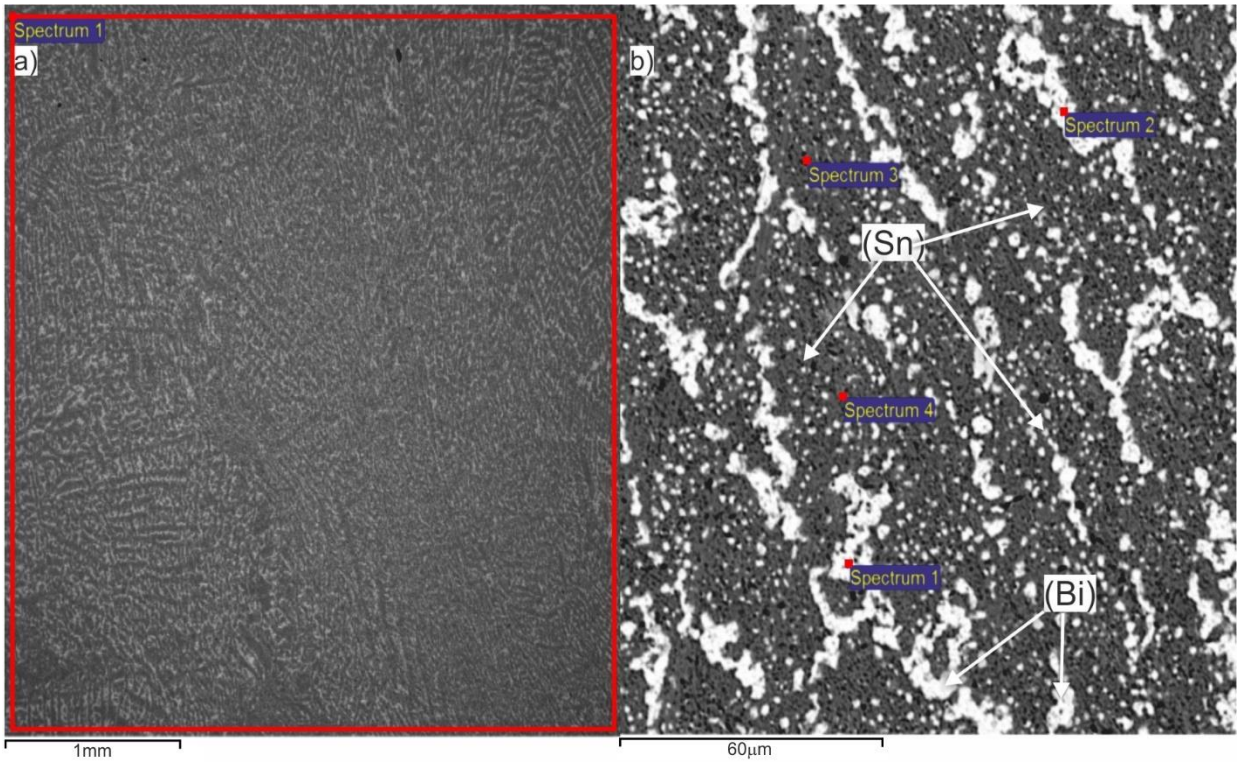

Fig. 3. SEM-EDS micrographs of the alloy 2 (Bi0.2Sn0.8): (a) determination of the overall composition; (b) determination of composition based on spectrums obtained at four different spots .

Table 2. Results of EDS spectrum analyses for the alloy 2 (Bi0.2Sn0.8)

Nominal composition of alloys, at.%		Overall composition of the observed surface, at.%		Identified phase	Individual point spectrum	Content, at.%	
						Sn	Bi
Bi	Sn	Bi	Sn	(Bi)	Spectrum 1	2.17	97.83
					Spectrum 2	3.40	96.60
20.00	80.00	19.82	80.18	(Sn)	Spectrum 3	96.48	3.52
					Spectrum 4	90.09	9.91

Fig. 4 represents the results of the SEM-EDS analysis for the near-eutectic sample, alloy 3 (Bi0.4Sn0.6) where the overall microstructure and details of the eutectic microstructure under higher magnification are shown.

Table 3 shows good agreement between the chemical composition of the examined surface and the nominal alloy composition. The Bi–Sn eutectic has an irregular lamellar structure, also termed a complex regular microstructure in which two phases are arranged in alternating not-flat plates [20]. This eutectic microstructure arrangement is also recognized as a “Chinese script” eutectic structure.

Figure 5 representing results of the EDS analysis for the Bi-rich alloy 6 (Bi0.8Sn0.2), shows the microstructure under low magnification (Fig. 5a) and high magnification with four different points for the analysis of the present phases (Fig. 5b).

As it is shown in Figure 5 and Table 4, the alloy 6 consists of bright, coarse dendrites of the Bi-rich solid solution and darker, interdendritic (Sn)+(Bi) eutectic regions. A good agreement between the chemical composition of the examined surface and the nominal alloy composition is obtained.

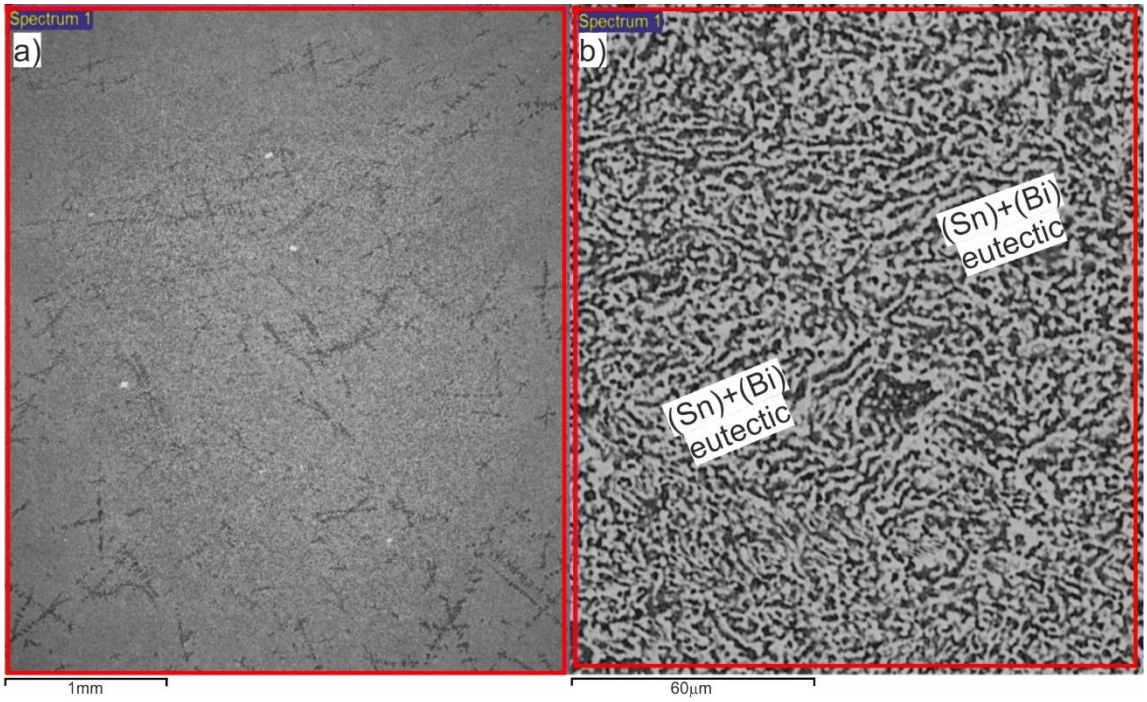

Fig. 4. SEM-EDS micrographs of the alloy 3 (Bi0.4Sn0.6): (a) determination of the overall composition; (b) determination of the composition of the eutectic microstructure

Table 3. Results of the EDS spectrum analysis for the alloy 3 (Bi0.4Sn0.6) showing the overall and the composition of the eutectic ((Sn)+(Bi)) mixture

Nominal composition of alloys, at%		Overall composition of the observed surface, at.%		Identified phase	Individual point spectrum	Content, at.%	
						Sn	Bi
Bi	Sn	Bi	Sn	(Sn)+(Bi) eutectic	Spectrum 1	60.72	39.28
40.00	60.00	39.14	60.86				

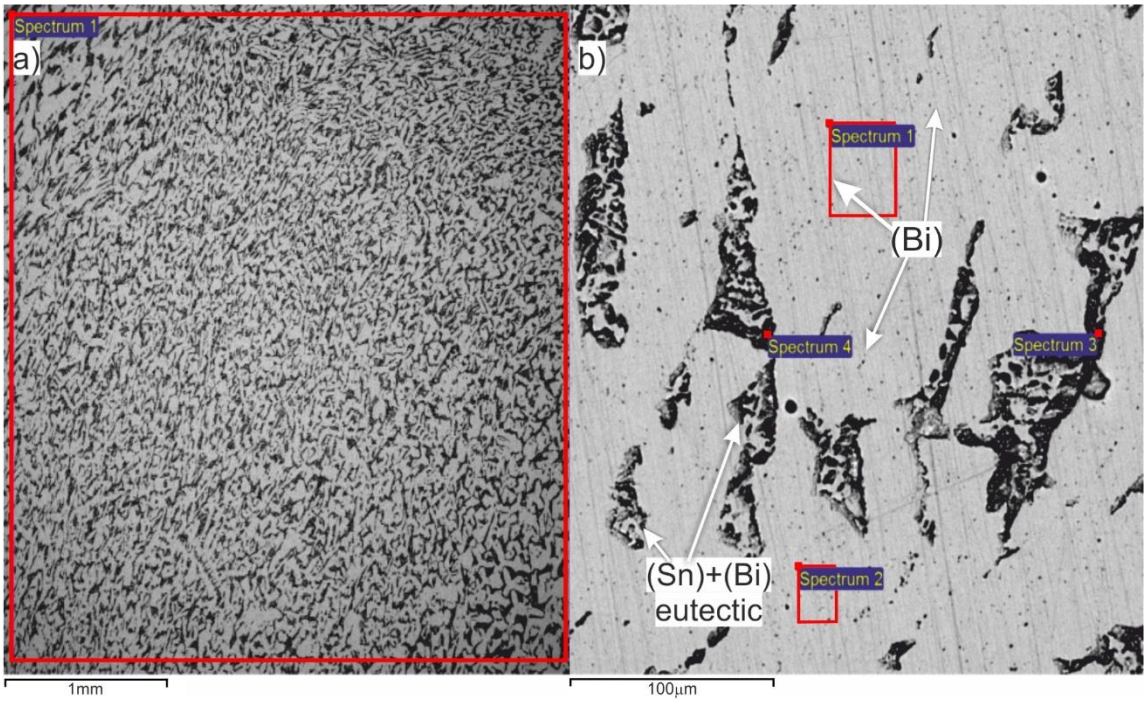

Fig. 5. SEM-EDS micrographs of the alloy 6 (Bi0.8Sn0.2): (a) determination of the overall composition; (b) determination of composition based on spectrums obtained at four different spots

Table 4. Results of EDS spectrum analyses for the alloy 6 (Bi0.8Sn0.2)

Nominal composition of alloys, at.%		Overall composition of the observed surface, at.%		Identified phase	Individual point spectrum	Content, at.%	
						Sn	Bi
Bi	Sn	Bi	Sn	(Bi)	Spectrum 1	2.56	97.44
					Spectrum 2	2.58	97.42
80.00	20.00	78.58	21.42	(Sn)+(Bi) eutectic	Spectrum 3	27.82	72.18
					Spectrum 4	46.43	53.57

The overall chemical compositions of the all prepared samples were checked by the EDS method and it was found that differences between the nominal and the experimentally determined compositions of alloys were negligible (less than 1 at.%).

3. 2. Hardness measurements

Hardness of the investigated alloys was determined by using the Brinell test method with the applied force of 50 N (Table 5). A decrease in hardness can be observed with addition of bismuth so that the largest hardness value was measured for the alloy 1. Similar results were observed in some previous studies [31].

Table 5. Hardness determined by using the Brinell test method at the force of 50N

Sample	Hardness, HB	
	Mean value	Standard deviation
Alloy 1	23.7	0.1
Alloy 2	22.4	0.4
Alloy 3	21.2	0.6
Alloy 4	20.0	0.4
Alloy 5	17.9	0.4
Alloy 6	18.0	0.4
Alloy 7	17.0	1.2
Pure Bi	10.7	0.2
Pure Sn	9.0	0.5

3. 3. DSC analysis

Melting behavior of the alloys was investigated by using differential scanning calorimetry (DSC) and results are given in Table 6 along with DSC thermograms in Figures 6-8, showing identified phase transition temperatures for the hypoeutectic alloy 2 (Bi0.2Sn0.8), near-eutectic alloy 3 (Bi0.4Sn0.6) and the hypereutectic alloy 6 (Bi0.8Sn0.2), respectively.

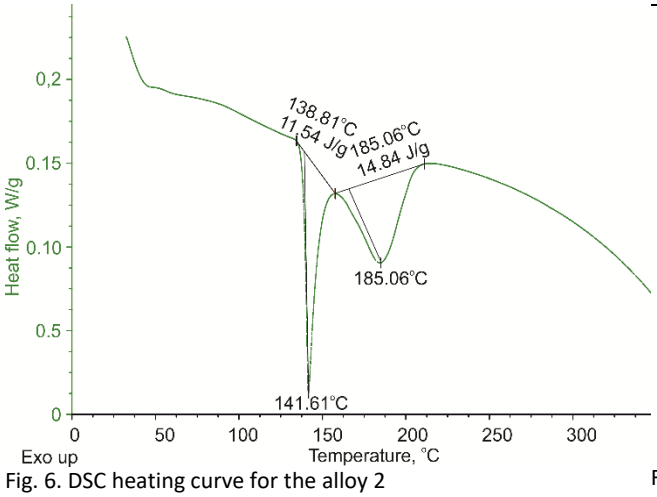

Fig. 6. DSC heating curve for the alloy 2

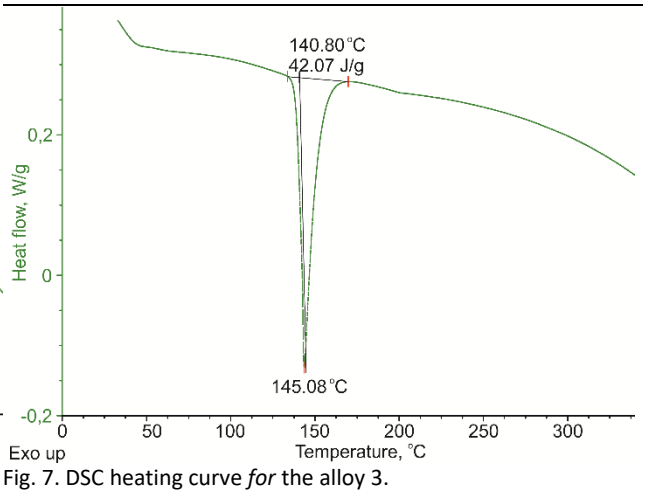

Fig. 7. DSC heating curve *for* the alloy 3.

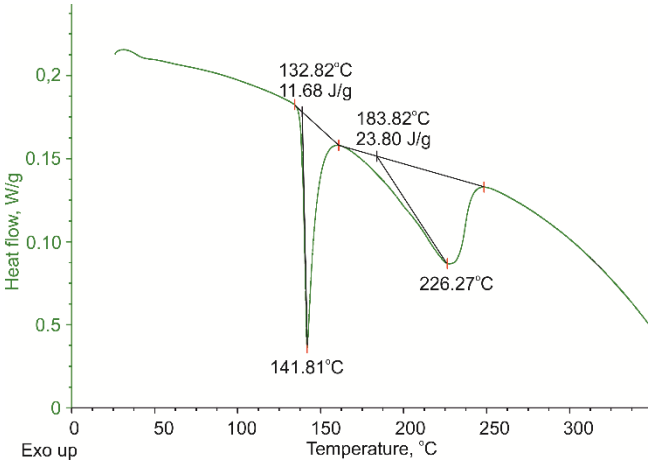

Fig. 8. DSC heating curve for the alloy 6

Table 6. Phase transitions temperatures for examined alloy compositions obtained by the DSC analysis

Sample	Phase transition temperature, °C	
	Eutectic reaction	Liquidus
Alloy 1	137.00	210.34
Alloy 2	138.80	185.00
Alloy 3	140.80	/
Alloy 4	139.73	171.11
Alloy 5	139.67	195.47
Alloy 6	138.82	226.27
Alloy 7	138.19	249.92

The obtained experimental results were compared to the results of thermodynamic calculations and good agreement was noticed. By using the COST 531 lead-free solder thermodynamic database [32] and the PANDAT software [33], a phase diagram for the Bi-Sn system was calculated (Fig. 9). Experimentally obtained results were inserted, where every square represents a temperature obtained by the DSC analysis, for a specific composition in the Sn-Bi system.

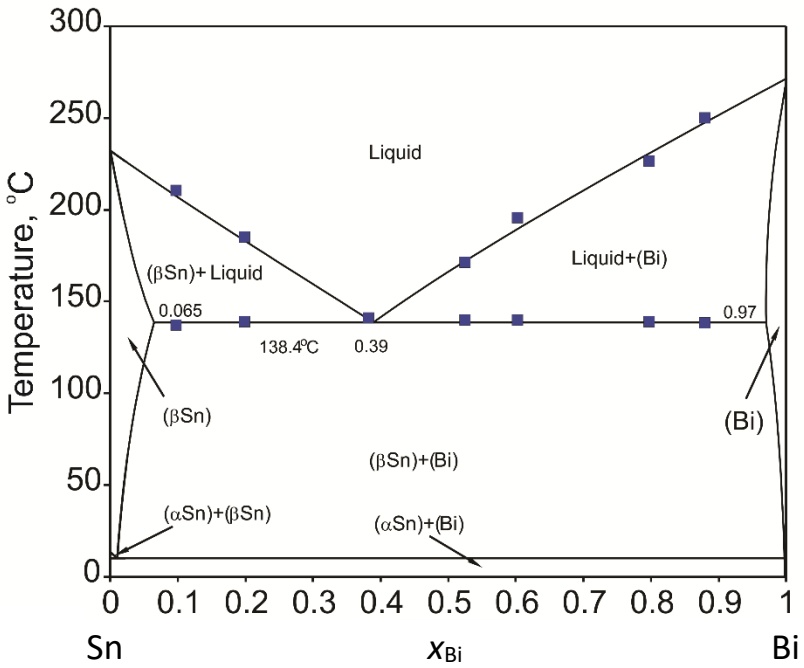

Figure 9. Calculated phase diagram of the Sn-Bi system by using the optimized thermodynamic parameters [32,34] and experimental results obtained in the present work (symbols)

Over the years, there were many uncertainties concerning the solvus surfaces of Bi and Sn in the Sn-Bi system. The uncertainties were mostly related to the Sn solvus surface, where the bismuth fraction went up to more than 10 at.% of bismuth in tin. In recent years, the solubility was calculated to be around 6.2 at.% [8]. In the present case, we confirmed that the solubility of Bi in tin was less than 10 at.%, and based on the calculated phase diagram using Pandat software [33], the solubility is around 6.5 at.%, which is in a good agreement with the proposed literature data.

3. 4. Thermal conductivity measurements

Thermal diffusivity and thermal conductivity were determined for every investigated Sn-Bi alloy composition by using the xenon-flash method [35]. Thermal conductivity of the investigated samples was determined by using the following fundamental relation (1):

$$\lambda = \alpha \, \rho \, C_p \tag{1}$$

where λ is the thermal conductivity, α is thermal diffusivity, ρ is density, and C_p is specific heat capacity. Thermal diffusivity was directly measured. Values of the specific heat capacity for the studied alloys were calculated by using the COST 531 thermodynamic database [32]. Alloys densities were determined by using the buoyancy method based on the Archimedes' principle. The results of conducted analyses are given in Table 7. The total uncertainty for the determined thermal conductivity is estimated to be ±8 % [30].

Table 7. Thermal diffusivities, specific heat capacities and thermal conductivities of the Bi-Sn alloys at 25, 50 and 100 °C.

Sample	t / °C	α / 10^{-4} m^2 s^{-1}		C_p / J g^{-1} K^{-1}	λ / W m^{-1} K^{-1}	
		Mean value	Standard deviation		Mean value	Standard deviation
Alloy 1	25	0.257	7.789	0.210	40.525	2.432
	50	0.253	7.594	0.213	40.337	2.420
	100	0.215	2.944	0.220	35.508	2.130
Alloy 2	25	0.172	9.274	0.195	26.161	1.570
	50	0.169	3.559	0.198	26.162	1.570
	100	0.148	2.082	0.204	23.597	1.416
Alloy 3	25	0.143	8.813	0.170	20.439	1.226
	50	0.143	2.887	0.173	20.683	1.241
	100	0.126	2.160	0.177	18.682	1.121
Alloy 4	25	0.125	7.416	0.160	19.764	1.186
	50	0.124	1.732	0.162	17.404	1.044
	100	0.110	2.887	0.166	15.852	0.951
Alloy 5	25	0.087	7.874	0.151	11.719	0.703
	50	0.089	8.832	0.153	12.065	0.724
	100	0.082	2.887	0.156	11.328	0.680
Alloy 6	25	0.057	1.000	0.135	7.231	0.434
	50	0.059	5.447	0.136	7.501	0.450
	100	0.057	1.732	0.139	7.484	0.449
Alloy 7	25	0.050	0.577	0.128	6.132	0.368
	50	0.051	1.732	0.129	6.341	0.380
	100	0.052	1.633	0.132	6.564	0.394

The obtained results show that the thermal diffusivity and thermal conductivity of the investigated Bi-Sn alloys gradually decrease with increasing the Bi content due to bismuth being one of the metals with the lowest thermal conductivity [36]. Figure 10 shows the dependence of the thermal conductivity on the alloy composition at 25 °C. The literature value of thermal conductivity for the commercial Bi58Sn42 (mas.%) solder alloy [37] is labeled in Figure 10 and used for comparison with the results obtained in the present study. A reasonable agreement can be observed. The specific heat capacity of the Sn-Bi alloys monotonically decreases with the increase in the Bi content (Fig. 11). It can be noticed that there is an excellent agreement of the calculated specific heat capacity in the present research with the value reported for the Bi58Sn42 (mas.%) solder alloy in literature [37].

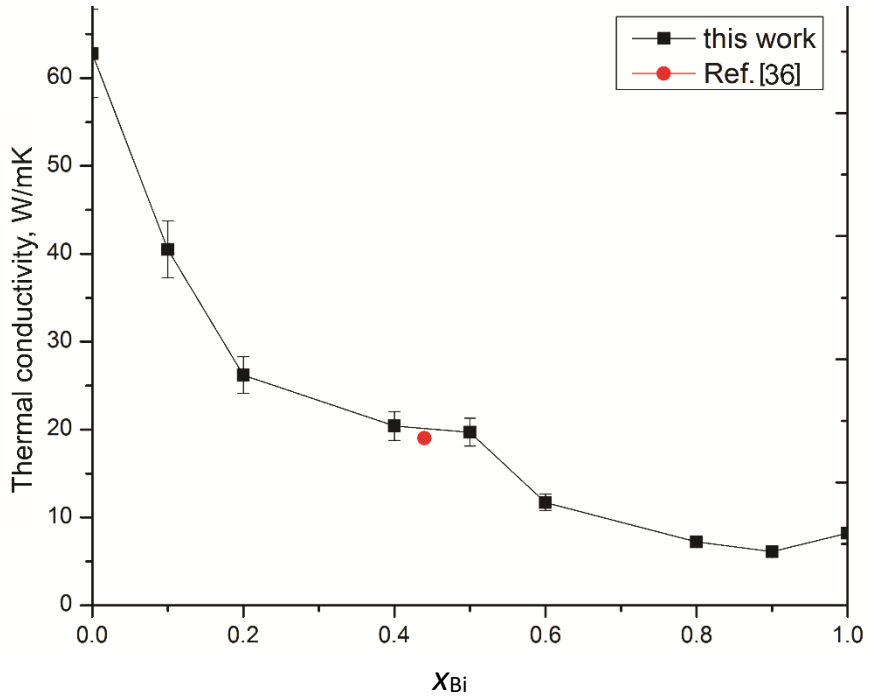

Fig. 10. Thermal conductivity of the Bi-Sn alloys at 25 °C as a function of alloy composition. Thermal conductivity values for pure Sn and Bi are from the ref. [38] while the red symbol shows the literature value for the commercial Bi58Sn42 (mas.%) solder alloy [37]

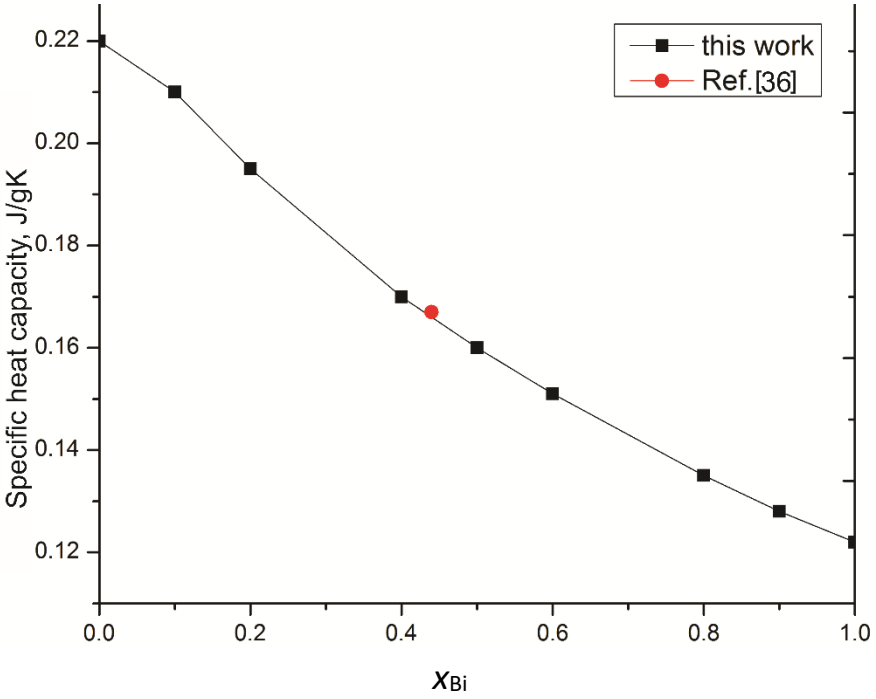

Fig. 11. Specific heat capacity of the Bi-Sn alloys at 25 °C as a function of alloy composition. Specific heat capacity values for pure Sn and Bi are from the ref. [38], while the red symbol shows the literature value for the commercial Bi58Sn42 (mas.%) solder alloy [37]

4. CONCLUSION

In this work, seven Sn-Bi alloys with bismuth molar fractions in the range from 0.1 - 0.9 were investigated regarding microstructure, hardness and thermal properties. Microstructural analyses performed by LOM and SEM- EDS have shown the existence of Sn-rich and Bi-rich solid solutions along with a complex regular eutectic microstructure

containing a mixture of (Sn) and (Bi) solution phases. Measured hardness values of the investigated Sn-Bi alloys were considerably higher than those of pure constitutive metals, Sn and Bi.

Using the optimized thermodynamic data from literature, a Sn-Bi phase diagram has been constructed. Furthermore, the phase transition temperatures, obtained by the DSC analysis, were compared to those in the phase diagram, and a good agreement was observed. Values of thermal diffusivity and thermal conductivity decreased with increasing the Bi content. The specific heat capacity also decreased with the increase in the Bi content and slightly increased with the increase in temperature. This work, focused on the investigation of thermal properties, hardness measurements and microstructure characterization of Sn-Bi alloys with different composition, provides a more detailed and attentive contribution to the general knowledge of this system.

Acknowledgements: The research presented in this paper was done with the financial support of the Ministry of Education, Science and Technological Development of the Republic of Serbia, within the funding of the scientific research work at the University of Belgrade, Technical Faculty in Bor, according to the contract under the registration number 451-03-9/2021-14/200131.

REFERENCES

[1] Frongia F, Pilloni M, Scano A, Ardu A, Cannas C, Musinu A, Borzone G, Delsante S, Novakovic R, Ennas G, Ennas. Synthesis and melting behaviour of Bi, Sn and Sn–Bi nanostructured alloy. *J. Alloys Compd.* 2015; 623: 7-14. https://doi.org/10.1016/j.jallcom.2014.08.122

[2] Ren G, Wilding I, Collins M. Alloying influences on low melt temperature SnZn and SnBi solder alloys for electronic interconnections. *J. Alloys Compd.* 2016; 665: 251-260. https://doi.org/10.1016/j.jallcom.2016.01.006

[3] Zhang X. P, Yu C. B, Zhang Y. P, Shrestha S, Dorn L. Processing treatment of a lead-free Sn–Ag–Cu–Bi solder by rapid laser-beam reflowing and the creep property of its soldered connection. *J. Mater. Process. Technol.* 2007; 192: 539-542. https://doi.org/10.1016/j.jmatprotec.2007.04.072

[4] Kanlayasiri K, Ariga T. Physical properties of Sn58Bi–xNi lead-free solder and its interfacial reaction with copper substrate. *Mater. Des.* 2015; 86: 371-378. https://doi.org/10.1016/j.matdes.2015.07.108

[5] Sun H, Li Q, Chan Y. A study of Ag additive methods by comparing mechanical properties between Sn57. 6Bi0. 4Ag and 0.4 wt% nano-Ag-doped Sn58Bi BGA solder joints. *J. Mater. Sci.: Mater. Electron.* 2014; 25: 4380-4390. https://doi.org/10.1007/s10854-014-2177-7

[6] Silva B, Garcia A, Spinelli J. Complex eutectic growth and Bi precipitation in ternary Sn-Bi-Cu and Sn-Bi-Ag alloys. *J. Alloys Compd.* 2017; 691: 600-605. https://doi.org/10.1016/j.jallcom.2016.09.003

[7] Abtew M, Selvaduray G. Lead-Free Solders in Microelectronics. *Mater. Sci. Eng.* 2000; 27: 95-141. https://doi.org/10.1016/S0927-796X(00)00010-3

[8] Braga M. H, Vizdal J, Kroupa A, Ferreira J, Soares D, Malheiros L. F. The experimental study of the Bi–Sn, Bi–Zn and Bi–Sn–Zn systems. *Calphad.* 2007; 31: 468–478. https://doi.org/10.1016/j.calphad.2007.04.004

[9] Mokhtari O, Nishikawa H. Correlation between microstructure and mechanical properties of Sn–Bi–X solders. *Mater. Sci. Eng.* 2016; 651: 831-839. https://doi.org/10.1016/j.msea.2015.11.038

[10] Zhao J, Qi L, Wang X, Wang L. Influence of Bi on microstructures evolution and mechanical properties in Sn–Ag–Cu lead-free solder. *J. Alloys Compd.* 2004; 375: 196-201. https://doi.org/10.1016/j.jallcom.2003.12.005

[11] Li J, Mannan S, Clode M, Whalley D, Hutt D. Interfacial reactions between molten Sn–Bi–X solders and Cu substrates for liquid solder interconnects. *Acta Mater.* 2006; 54: 2907-2922. https://doi.org/10.1016/j.actamat.2006.02.030

[12] Shen J, Pu Y, Yin H, Luo D, Chen J. Effects of minor Cu and Zn additions on the thermal, microstructure and tensile properties of Sn–Bi-based solder alloys. *J. Alloys Compd.* 2014; 614: 63-70. https://doi.org/10.1016/j.jallcom.2014.06.015

[13] Shalaby R. Effect of silver and indium addition on mechanical properties and indentation creep behavior of rapidly solidified Bi–Sn based lead-free solder alloys. *Mater. Sci. Eng., A.* 2013; 560: 86-95. https://doi.org/10.1016/j.msea.2012.09.038

[14] Miao H, Duh J. Microstructure evolution in Sn–Bi and Sn–Bi–Cu solder joints under thermal aging. *Mater. Chem. Phys.*. 2013; 71: 255-271. https://doi.org/10.1016/S0254-0584(01)00298-X

[15] Peng Y, Deng K. Fabrication of reduced graphene oxide nanosheets reinforced Sn–Bi nanocomposites by electro-chemical deposition. *Compos. Part A Appl. Sci. Manuf.* 2015; 73: 55–62. https://doi.org/10.1016/j.compositesa.2015.03.006

[16] Billah M, Chen Q. Thermal conductivity of Ni-coated MWCNT reinforced 70Sn-30Bi alloy. *Compos. B. Eng.* 2017; 129: 162-168. https://doi.org/10.1016/j.compositesb.2017.07.071

[17] Wang J, Wei H, He P, Lin T, Lu F. Microstructure and mechanical properties of tin-bismuth solder reinforced by aluminum borate whiskers. *J. Electron. Mater.* 2015; 44: 3872-3879. https://doi.org/10.1007/s11664-015-3896-0

[18] Peng Y, Deng K. Study on the mechanical properties of the novel Sn–Bi/Graphene nanocomposite by finite element simulation. *J. Alloys Compd.* 2015; 625: 44-51. https://doi.org/10.1016/j.jallcom.2014.11.110

[19] Lai Z, Ye D. Microstructure and fracture behavior of non eutectic Sn–Bi solder alloys. *J. Mater. Sci.: Mater. Electron.*2016; 27: 3182-3192. https://doi.org/10.1007/s10854-015-4143-4

[20] Silva B, Reinhart G, Nguyen-Thi H, Mangelinck-Noël N, Garcia A, Spinelli J. Microstructural development and mechanical properties of a near-eutectic directionally solidified Sn–Bi solder alloy. *Mater. Charact.* 2015; 107: 43-53. https://doi.org/10.1016/j.matchar.2015.06.026

[21] Gao L, Wang J, Lin T, He P, Lu F. Improvement of microstructure and mechanical properties of Sn-58Bi alloy with La_2O_3. In: *14th International Conference on Electronic Packaging Technology*. Dalian, China, 2013, pp. 193-195.

[22] Osório W, Peixoto L, Garcia L, Mangelinck-Noël N, Garcia A. Microstructure and mechanical properties of Sn–Bi, Sn–Ag and Sn–Zn lead-free solder alloys. *J. Alloys Compd.* 2013; 572: 97-106. https://doi.org/10.1016/j.jallcom.2013.03.234

[23] Guo Q, Zhao Z, Shen C. Comparison study on microstructure and mechanical properties of Sn-10Bi and Sn-Ag-Cu solder alloys and joints. *Microelectron Reliab.* 2017; 78: 72-79.

[24] Wang Q, Cheng X, Li Y, Yu G, Liu Z. Microstructures and Thermal Properties of Sn–Bi–Zn–Ga Alloys as Heat Transfer and Heat Storage Materials. *J. Wuhan Univ. Technol. Mater. Sci. Ed.* 2019; 34: 676-683. https://doi.org/10.1007/s11595-019-2103-1

[25] Wang F, Huang Y, ZhangZ, Yan C. Interfacial reaction and mechanical properties of Sn-Bi solder joints. *Mater.* 2017; 10: 920-936. https://doi.org/10.3390/ma10080920

[26] Hua F, Zequn M, Glazer J. Eutectic Sn-Bi as an alternative to Pb-free solders. In: *Proceedings of 48th Electronic Components and Technology Conference*. Seattle, Washington, 1998, pp. 277-283.

[27] Dong W, Shi Y, Xia Z, Lei Y, Guo F. Effects of trace amounts of rare earth additions on microstructure and properties of Sn-Bi-based solder alloy. *J. Electron. Mater*. 2008; 37: 982-991. https://doi.org/10.1007/s11664-008-0458-8

[28] Morando C, Fornaro O, Garbellini O, Palacio H. Thermal properties of Sn-based solder alloys. *J. Mater. Sci.: Mater. Electron.* 2014; 25: 3440-3447. https://doi.org/10.1007/s10854-014-2036-6

[29] Hu X, Li Y, Min Z. Interfacial reaction and growth behavior of IMCs layer between Sn–58Bi solders and a Cu substrate. *J. Mater. Sci.: Mater. Electron.* 2013; 24: 2027-2034 https://doi.org/10.1007/s10854-012-1052-7

[30] Manasijević D, Balanović Lj, Ćosović V, Minić D, Premović M, Gorgievski M, Stamenković U, Talijan N. Thermal characterization of the In–Sn–Zn eutectic alloy. *Metall. Mater. Eng*. 2019; 25: 325-334. https://doi.org/10.30544/456

[31] Marković B, Živković D, Manasijević D, Talijan N, Sokić M, Ćosović V. Phase Equilibria Calculation and Investigation of Hardness and Electrical Conductivity for Alloys in Selected Sections of Bi-Cu-Ni System. *J. powder metall. min.* 2012; 2:104 https://doi.org/10.4172/2168-9806.1000104

[32] Kroupa A, Dinsdale A, Watson A, Vrestal J, Vízdal J, Zemanova A. The development of the COST 531 lead-free solders thermodynamic database. *JOM*. 2007; 59: 20-25. https://doi.org/10.1007/s11837-007-0084-6

[33] Cao W, Chen S, Zhang F, Wu K, Yang Y, Chang Y, Schmid-Fetzer R, Oates W. PANDAT Software with PanEngine, PanOptimizer and PanPrecipitation for Multi-Component Phase Diagram Calculation and Materials Property Simulation. *Calphad*. 2009; 33: 328–342. https://doi.org/10.1016/j.calphad.2008.08.004

[34] Vízdal J, Braga M, Kroupa A, Richter K, Soares D, Malheiros L, Ferreira J. Thermodynamic assessment of the Bi–Sn–Zn System. *Calphad*. 2007; 31: 438-448. https://doi.org/10.1016/j.calphad.2007.05.002

[35] Parker W, Jenkins R, Butler C, Abbot G. Flash Method of Determining Thermal Diffusivity, Heat Capacity, and Thermal Conductivity. *J. Appl. Phys.* 1961; 32: 1679-84. https://doi.org/10.1063/1.1728417

[36] Engineering ToolBox, (2005). Thermal Conductivity of Metals, Metallic Elements and Alloys. [online] Available at: https://www.engineeringtoolbox.com/thermal-conductivity-metals-d_858.html. Accessed January 11, 2021.

[37] Indium Corp. Indalloy® 281 Bi-Sn Solder Alloy. http://www.matweb.com/search/datasheet.aspx?matguid=967a4cd7871b46fa9128a29c303cf8be. Accessed January 11, 2021.

[38] ASM Handbook Volume 2. *Properties and Selection: Nonferrous Alloys and Special-Purpose Materials*. ASM International; 1990.

SAŽETAK

Ispitivanje mikrostrukture, tvrdoće i termijskih karakteristika legura u sistemu Sn-Bi

Kristina N. Božinović, Dragan M. Manasijević, Ljubiša T. Balanović, Milan D. Gorgievski, Uroš S. Stamenković, Miljan S. Marković i Zoran D. Mladenović

Tehnički fakiltet u Boru, Odsek za metalurško inženjerstvo, Univerzitet u Beogradu, Vojske Jugoslavije 12, 19210 Bor, Srbija

(Naučni rad)

Zbog velike toksičnosti olova, bezolovni lemovi postali su glavni fokus elektronske industrije poslednjih godina. Zbog svojih povoljnih svojstava i niske cene, legure iz sistema Sn-Bi predstavljaju potencijalnu zamenu za legure Sn-Pb u lemljenju. Jedna od glavnih prednosti legura iz sistema Sn-Bi su niske temperature topljenja. Legure iz ovog sistema su takođe veoma atraktivne zbog dobre kompatibilnosti sa podlogama, niske temperature procesa, visoke pouzdanosti i potencijalne primene u vidu materijala termičkog sučelja. U ovom radu je urađena karakterizacija mikrostrukturnih i termijskih karakteristika, kao i merenje tvrdoće sedam Sn-Bi legura različitog sastava. Strukturna svojstva uzoraka analizirana su optičkom mikroskopijom i skenirajućom elektronskom mikroskopijom sa energetski disperzivnom spektrometrijom (SEM-EDS). Toplotna provodljivost uzoraka je ispitivana ksenon-fleš metodom (engl. xenon-flash method), a temperature faznih transformacija merene su diferencijalnom skenirajučom kalorimetrijom (engl. differential scanning calorimetry, DSC).

Ključne reči: strukturna svojstva; lemljenje; bezolovne lemne legure; toplotna provodljivost

Experimental investigation of a one-level eight-channel cyclone-separator incorporating quarter-rings

Aleksandras Chlebnikovas

Research Institute of Environmental Protection, Institute of Mechanical Science, Vilnius Gediminas Technical University, Vilnius, Lithuania

Abstract

The main aim of this investigation was an experimental analysis of the air cleaning efficiency in a mock-up next-generation air cleaning device – one-level 8-channel industrial cyclone-separator with quarter-rings – while changing parameters of the inner structure and the assessment of the effects of dispersion of particulate matter. Therefore, the research was carried out in two stages: the first stage covered the analysis of the efficiency of the multi-channel cyclone with particulate matter of <20 and <50 μm. During the second stage, a cascade impactor was used to measure the particle collection efficiency in the multi-channel cyclone by fractions: PM1, PM2.5 and PM10. Results of the tests with using the cascade impactor were compared to show changes in the PM composition before and after the multi-channel cyclone-separator. According to the obtained experimental data, the one-level 8-channel cyclone-separator collects 70 to 80 % of PM up to 10 μm in size, 45 to 60 % of PM up to 2.5 μm in size and 21 to 25 % of PM up to 1 μm in size.

Keywords: multi-channel cyclone-separator; particulate matter; air treatment; channel; cascade impactor.

Available on-line at the Journal web address: http://www.ache.org.rs/HI/

TECHNICAL PAPER

UDC: 621.928.93: 614.44-032.1

Hem. Ind. **75 (4)** 241-251 (2021)

1. INTRODUCTION

Industrial progress is closely related to environmental protection objectives with one of the most important being treatment of air pollution. Electrostatic and sleeve filters are the most commonly applied devices in world practice due to high efficiency in removing particulate matter (PM) from the air. However, they are expensive and rather difficult to maintain [1–4]. Centrifugal filter is a kind of industrial equipment used for gas (air)-PM separation in thermal power plants, fluidized bed combustion processes, control of air pollution as well as for sorting/sieving materials [5]. Advantages of this filter type include collection and fractional efficiency and low pressure drop [6].

Air treatment facilities are under ongoing development aimed at cleaning the air from increasingly complex chemical compounds and finer PM, with improved cleaning efficiency and reduced operational costs. The term particulate matter (PM) refers to diverse tiny particles found, for example, in exhaust emissions and technological process emissions. It is widely recognized now that fine PM has extremely severe effects on human health. These particles affect lungs and may have adverse effects on humans of various ages, but primarily on people diagnosed already with lung and heart diseases [7,8]. It should be also noted that airborne PM can pass through the skin or eye mucous tissues, but most of PM enter the respiratory system [9]. The smaller is the diameter of the particle, the deeper it settles in the respiratory system. In addition to the respiratory system, PM affects the cardiovascular system causing various heart diseases. Moreover, deposition of these pollutants in the lungs creates an additional load on the heart as it tries to compensate for the reduced oxygen content. Combustion products containing carcinogen benzo[a]pyrene may cause cancer [10]. Likewise, exposure to PM has been found to be associated with lower body resistance to infection. Pneumoconiosis, a common and serious lung disease, is caused by inhaling polluted air containing free silica, or SiO_2 particles. Pneumoconiosis remains a severe global public health issue due to lack of PM prevention in the workplace [11]. Free silicon dioxides

Corresponding author: Aleksandras Chlebnikovas, Research Institute of Environmental Protection, Institute of Mechanical Science, Vilnius Gediminas Technical University, Vilnius, Lithuania

E-mail: aleksandras.chlebnikovas@vilniustech.lt; Tel./Fax: +370 52 74 4726

Paper received: 7 March 2021; Paper accepted: 18 August 2021; Paper published: 31 August, 2021

https://doi.org/10.2298/HEMIND210307024C

(sand, quartz) not only affect the lung tissue locally, but also have adverse effects on the entire human body causing functional disorders in the cardiovascular system, central nervous system, etc. Silicosis is a common disease suffered by people working in dusty conditions [12].

Selection of gas treatment equipment should consider a number of factors such as physical/ chemical characteristics of polluted gas and characteristics and contents of gaseous pollutants and PM. Complex pollution of dusted gases requires the use of multistage treatment systems, including dry and wet cleaning devices, which increases capital and operating costs [17, 18]. Apparatus for complex purification of off gases operates in the regime of developed turbulence and is a promising tool for solving this problem [13,14].

Cyclones have been so far some of the most popular devices used for removing PM from air. The reason is a simple structure, low cost and easy operation of these devices. Cyclones are recommended for gas pre-treatment, while the secondary treatment phase usually involves other air treatment devices [15–17] collecting particles smaller than 20 μm. Multi-stage air treatment systems, however, are more complex and expensive [18]. Analysis of PM separation principles shows that for intensification of the dust collection process in gas-PM systems, the use of centrifugal and vortex interactions in fluid flows are the most effective. PM is affected by inertial and centrifugal forces, which significantly exceed the force of gravity. Devices with a regular movable nozzle are an example of vortex interactions of fluid flows. Packing bodies are mounted on flexible strings at fixed steps in vertical and radial directions in the contact zone [14]. Wet-based cyclone design is less implemented due to production of mud or sludge with small particle size (less than 50 μm) and high mass concentration. The conventional hydrocyclone has a poor separation effect in gases with high concentrations of fine particles [19].

Cyclones are incomparable in terms of the price and simplicity of their structure and operation. Due to the specific structure without any movable parts or filtering surfaces that would require regular maintenance, resulting in comparatively small aerodynamic resistance and high efficiency, cyclones are likely to remain competitive in the modern market of air cleaning systems for a long time [20].

Operation of a usual cyclone is based on the widespread principle of separating PM by centrifugal forces created by the turbulent airflow within the equipment shell. The efficiency of such cyclones ranges between 75 and 85 %, for particles larger than 20 μm in size. However, this is not sufficient in terms of the objectives laid down in the EU Directive 2008/50/EC on ambient air quality and cleaner air for Europe [21–25].

On the other hand, multi-channel cyclones can remove very small particles down to 2 μm in size from contaminated airflows. These devices present a possible alternative to more expensive air treatment technologies that are currently in use. In addition, application of a multi-channel cyclone-separator for air cleaning is possible in environments with high temperatures and humidity [26,27].

One of the problems in calculation of the efficiency of a cyclone is the effect of flow dynamic parameters. The flow, which is turbulent in the cyclone body, may be laminar at the entrance. Laminar flow operating parameters have a greater influence on the cyclone efficiency than those of turbulent flow. In small cyclones, it is extremely difficult to predict the effect of flow regime on efficiency and pressure losses compared to the effects of geometrical parameters. It is even more complicated to identify parameters and evaluate a two-phase flow movement in a multi-channel cyclone, as flow dynamics is turbulent and involves such aspects as a swirling movement and backflow circular areas [28,29]. Closed-vortex-flow theory has so far not been able to identify features of a number of flow fields. In addition, assessment based on the turbulence isotropy assumption cannot be adapted to quickly swirling flows [30].

The purpose of this research was an experimental analysis of the air cleaning efficiency in a mock-up next-generation air cleaning device, a one-level 8-channel industrial cyclone with quarter-rings. The aim was to vary the parameters of the inner structure as well as to assess the effects of PM dispersion on the cleaning efficiency. Therefore, the research was carried out in two stages: the first stage focused on the efficiency analysis of the multi-channel cyclone-separator with PM of <20 and <50 μm in size. During the second stage, a cascade impactor was used to measure the particle collection efficiency in the multi-channel cyclone-separator by fractions: PM1, PM2.5 and PM10.

2. RESEARCH METHODS

The mock-ups of one-level, two-level and three-level next-generation multi-channel cyclones have been made at the Research Institute of Environmental Protection of Vilnius Gediminas Technical University (VilniusTech) (Fig. 1) [31,32]. The contaminated air 1 enters the cyclone and passes through channels 3 where particulate matter is collected and then deposited in the collection hopper 4. The purified air 2 exits the cyclone. The use of two-level or three-level cyclones is reasonable in cases of cleaning larger quantities of contaminated air. The novelty of the mock-ups of the multi-channel cyclone-separator provides the opportunity to clean larger quantities of contaminated air by using a smaller cross-section of the cyclone. For this purpose, the number of cyclone levels is increased while the cross-section of the separation chamber remains the same.

Multi-channel cyclones work by centrifugal forces with the additional filtration effect (Fig. 2). The two-phase airflow tangentially passes through the inlet 1 and enters the first channel of the cyclone 8 which is restrained by the peripheral wall and the first quarter-ring 6. Moving gradually in the radial direction, the flow is cleaned from PM by centrifugal force. The flow proceeding to the following channels encounters the quarter-ring wall and is distributed into two flows: peripheral and transitional. The peripheral flow passes to repeated filtration in the cyclone, while the transitional flow goes to the following channel towards the axis of the device and the outlet of the cyclone. In this way, the airflow is distributed evenly in channels with different curves and is filtered through the spaces between the quarter-rings. Turbulent flow is dependent on the fluid velocity, where the turbulent intensity influences the effect of centrifugation while the additional filtration effect occurs in the flow distribution zone. The overall effect of the forces is precipitation of PM at the bottom of the multi-channel cyclone and the particles settle into a conical settlement hopper. Having passed through all six channels of the cyclone, cleaned air flows out of the system through the outlet 4. The dusty air is filtered in the active zone of each channel space. It is a difficult task to investigate dependencies of aerodynamic and separation efficiency parameters, as the flow is influenced by many other parameters (specific geometry, distribution of feedback flows into channels (peripheral and transitional), emission and properties of particulate matter) in addition to its three-dimensional nature [11].

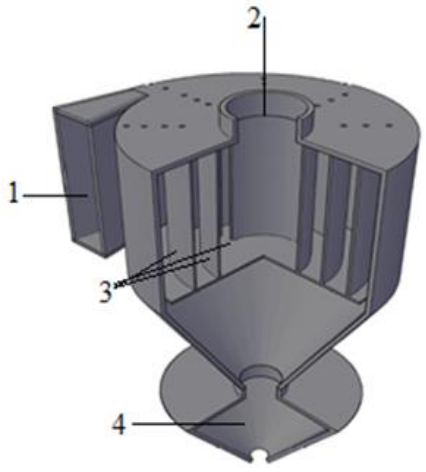

Figure 1. Basic diagram of a one-level multi-channel cyclone-separator: 1– contaminated air, 2 – purified air, 3 –channels of the cyclone, 4 – dust collection hopper

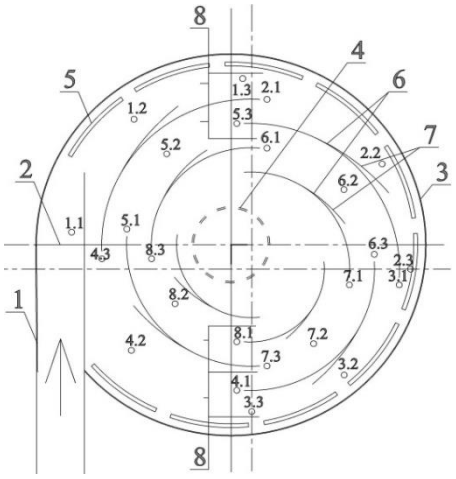

Figure 2. Basic diagram of the 8-channel cyclone-separator: 1 – dusty air flow inlet, 1.1-8.3 – sampling points, 2 – inlet, 3 – cyclone separation chamber, 4 – treated airflow outlet, 5 – segmental ring slots, 6 – curvilinear quarter-rings with a 5° opening angle of plates, 7 – opened plates of quarter-rings, 8 – cyclone channels

Experimental tests were carried out to determine the overall air cleaning efficiency and the efficiency of PM removal by fractions using a cascade impactor system.

The basic diagram of the experimental stand is illustrated in Figure 3. Experimental tests for airflow velocities and pressures were conducted within a system of air ducts with sampling points positioned along a straight section of the steady gas flow so to avoid airflow obstructions (valves, elbows, fans, *etc.)* and in 6 mm gaps made inside the structure of the cyclone, and in the cyclone lid.

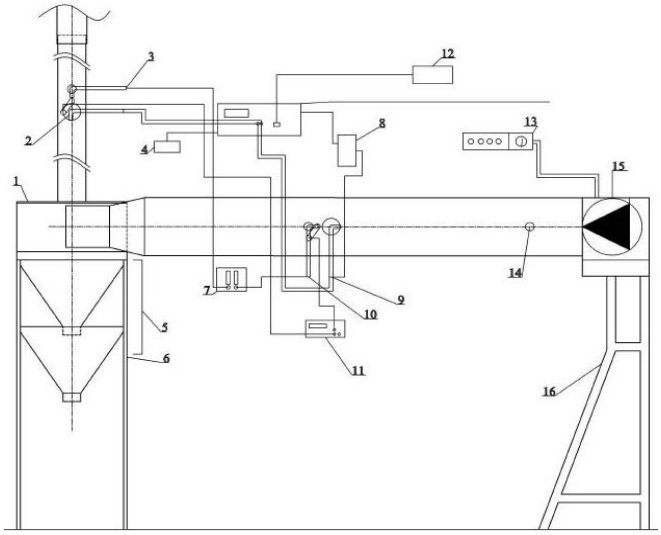

Figure 3. Basic diagram of the experimental stand: 1 – multi-channel cyclone-separator, 2, 9 – isokinetic combined probe of the cascade impactor, 3, 10 – velocity measurement and concentration measurement by using the gravity method, 4 – vacuum pump, 5 – collected PM tank, 6, 16 – supporting structure, 7 – aspirator, 8 – drying tower with the moisture trap, 11 – pressure measurement by a differential pressure gauge DSM-1, 12 – portable computer, 13 – fan control unit, 14 – PM inlet, 15 – centrifugal fan.

To perform the experimental tests, a pre-measurement procedure for airflow velocities and pressures consisted of the following steps: connecting the fan, setting the appropriate airflow velocity, setting the lever of the control unit to the appropriate position, connecting measuring devices.

Airflow pressure in the air ducts was measured before the tangential inlet and behind the cyclone by using a differential pressure gauge DSM–1 (JSC Teltonika, Lithuania, range of measurements: 0–20.000 kPa; deviation ±5 Pa); flow velocity was measured by using the instrument TESTO–400 (Testo SE & Co. KGaA, Germany, range of velocity measurements: 1–30 m s^{-1}, deviation ±0.05 m s^{-1}); aerodynamic resistance was measured by using a Pitot-Prandtl tube (range of velocity measurements: 5−30 m s^{-1}, deviation ±0.05 m s^{-1}).

The airflow within the cyclone-separators is ensured by the 7.5 kW fan system (MBRU 450 T2, CASALS Ventilacion air industrial SLU, Spain, 7.5 kW; rated capacity – 7.5 m^3 s^{-1}). Airflow velocities within the device are analyzed as a function of different airflow rates produced by the fan. Air velocities are measured at three points in each channel of the multi-channel cyclone-separator: at the inlet, in the middle and at the end of the channel. To achieve the maximum accuracy, measurements at each point are taken: 2 cm from the top of the channel, in the middle of the channel and 2 cm from the bottom of the channel.

Airflow velocities and aerodynamic resistance were measured three times in one-level, two-level and three-level multi-channel cyclonic system in order to avoid systemic errors and to reduce the error of the mean of the three results obtained.

During the experiment first stage, air cleaning efficiency is measured by using the gravity method. During the first experimental stage, PM of two sizes (sieved up to 20 µm and up to 50 µm) was used. The tests involved granite, glass, wood ash and wood particulate matter at the mean inlet concentrations of 250, 270, 260 and 235 mg m^{-3}, respectively. The mean size of particulate matter sieved up to 50 µm was equal to: granite – 13.7 µm, glass – 10 µm, wood ash – 14.9 µm and wood – 16 µm. The mean size of particulate matter sieved up to 20 µm was equal to: granite – 8.9 µm, glass – 7.6 µm, wood ash – 10.8 µm and wood – 11.0 µm. The particles are blown in the direction of the flow into the system air duct behind the fan. The appropriate velocity and flow rate of the air to be treated are set in the control unit prior to introducing PM.

Concentration of PM in the air ducts is measured in straight sections with steady gas flow so that to avoid flow obstructions (valves, elbows, fans, *etc*.): the measurement (sampling) point is preceded by a part of the straight duct 5-6 duct diameters in length and followed by the straight duct 3-4 diameters in length. The PM concentrations are measured three times in the system in order to avoid systemic errors and to reduce the error of the mean of the three results obtained. Locations of the sampling points in the experimental stands of one-level, two-level and three-level cyclone-separators are presented in Figures 2 and 3. During the second experimental stage, PM of smaller sizes (sieved up to 20 µm) was used, aerodynamic parameters (gas flowrate) and PM composition were the same as for the first stage.

The quantities of PM are measured by using a KALMAN-type cascade impactor system with an isokinetic probe (Kalman KS-220, Kalman System Ltd., Hungary). Quartz filters of the impactor allow measuring concentrations of individual PM fractions. The samples were analyzed in accordance with the standard ISO 9096.

3. RESULTS AND DISCUSSION

Analysis of the gas velocity distribution in one-level multi-channel cyclone-separator has revealed that the average airflow velocity in the channels was 10.0 m s^{-1} at the air flowrate of 935 m^3 h^{-1}. That air flowrate is often used in boilers (solid fuel (coal, coke, wood pellets used for heat or hot water production). Cyclone-separator is installed behind the boiler for separation of particulate matter from the emitted flow of a boiler of average power (0.5 – 1 MW) while the gas velocity corresponds to the range from 10 to 20 m s^{-1} usually used in conventional cyclone-separators [33,34]. For example, at the gas flowrate of 113 m^{-3} h corresponding to the velocity of 16 m s^{-1}, the cyclone pressure drop was measured as 1200 Pa [35]. On the other hand, a spiral cyclone-separator induces higher pressure drops due to a larger radius of curvature, and therefore the gas velocity should be up to 15.4 m s^{-1} [36]. Next, the aerodynamic resistance was analyzed in the multi-channel cyclone under a 50/50 flow distribution ratio between the transitional and peripheral flows using quarter-rings with a 5° opening angle of plates. The summarized tests data show that the aerodynamic resistance in this case was 1150 Pa. A study of the aerodynamic resistance of a four-channel cyclone [37] demonstrated that an aggressive dispersed gas and vapor flow increased the pressure drop by approximately 10%. Based on a numerical simulation study [34], the highest static pressure zones are at the beginning of the first and second channels where pressure values reach around 350 Pa. The static pressure of gas flow has been experimentally proved to reach 640 Pa prior to entering the cyclone but decreases by 50 % in the next sections [34]. Due to a more complex internal design of the multi-channel cyclone-separator as compared to a hollow conventional cyclone, the pressure drop is for 10–15 % greater at low flowrates, while it is equal in both devices at the maximum inlet flowrate [38]. A study of pressure drop in a small cyclone has shown that the values were equal to 1200 Pa at the same gas velocity (12 m s^{-1} approximately) [6]. The value of aerodynamic resistance is presumed to have increased compared to the conventional cyclone-separator due to additional local obstructions (curved elements and separation chamber).

Efficiency of the cyclone-separator determined for 2 particle sizes (<20 μm and <50 μm) during the first experimental stage is presented in Figure 4. The highest air treatment efficiency is obtained for granite PM with the efficiency of 88.8 % for removal of the coarse particles and 87.0 % for smaller particles.

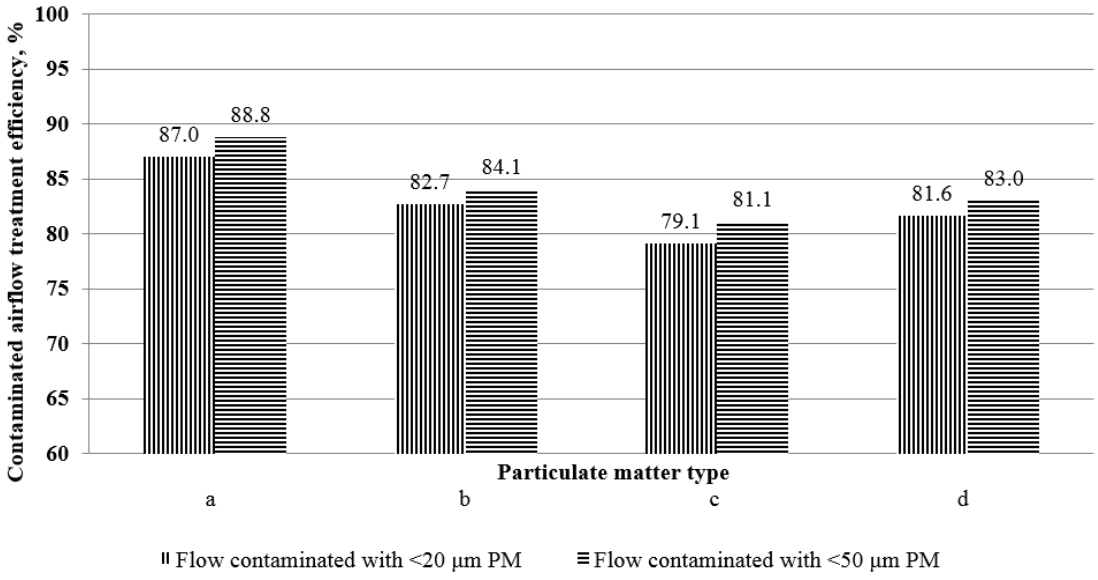

Figure 4. Overall air treatment efficiency in the one-level 8-channel cyclone-separator mock-up for different PM with particle sized of up to 20 μm and 50 μm, under the average airflow velocity in the channels of 10 m s^{-1} and a flow distribution ratio of 50/50, using quarter-rings with 5° opening angle of plates: a) granite, b) wood ash, c) glass, d) wood

Granite PM has the highest specific gravity as compared to the other investigated materials. The obtained overall air treatment efficiency was 9–11 % higher than the results reported for a dust collector of a cyclonic-vortex dry-type plant at an optimal velocity of 5 m s^{-1} [14]. In a previous research study [39] the optimal velocity for a conventional cyclone design with multi inlet guide channels is reported to be 8.8 m s^{-1}. The separation efficiency for particles of up to 2 µm in size was 71.2 % and for smaller particles up to 1 µm in size was 54.6 % [39]. In the present study, the air treatment efficiencies for wood ash PM were lower by 4.7 and 4.3% for larger (up to 50 µm) and smaller (up to 20 µm) particles, respectively, as compared to those obtained for granite PM.

It can be also presumed that the greater efficiency in collecting granite PM is obtained due to higher levels of particle agglomeration and autohesion. This leads to more intensive cohesion (autohesion) of granite PM and settlement into the cyclone hopper as compared to wood ash PM. These phenomena are highly affected by the humidity of gas which can decrease the separation level [37].It is also presumed that the difference in the efficiency of collecting PM of different particle sizes is insignificant. Therefore, it can be concluded that filtration is efficient at a 50/50 distribution ratio between the transitional and peripheral flows, with particular effects on small particles of up to 20 µm in size. Further tests with wood PM demonstrated 83.0 and 81.6 % treatment efficiency for PM <50 and <20 µm, respectively. Deposition of wood PM is influenced by the irregular shape, surface structure and cohesion (autohesion) of the particles. Difference in the efficiency of collecting wood ash PM and wood PM is only 1.1 %. Wood PM has a low specific gravity and is therefore the most difficult to be settled by centrifugation. However, tests with wood PM have shown that the particles get electrostatically charged the most intensively as compared to the other PM. The charged particles shrink, become heavier and thus easier to settle in. Tests with glass PM demonstrated lower treatment efficiencies as compared to those of the other PM being 81.1 and 79.1 % for particles of up to 50 and 20 µm, respectively, which is 7.7 and 7.9 % lower as compared to granite particles, respectively. Removal of glass PM from air is presumably impeded by comparatively low particle aggregation. It is assumed that glass particles are not so sticky as wood or wood ash particles, so that the agglomeration is lower resulting in a lower treatment efficiency in the cyclone-separator.

During the second experimental stage, the cascade impactor system was used to analyze the efficiency of the multi-channel cyclone mock-up for removing fine particles of <1, <2.5 and <10 µm in size of different material types (Fig. 5).

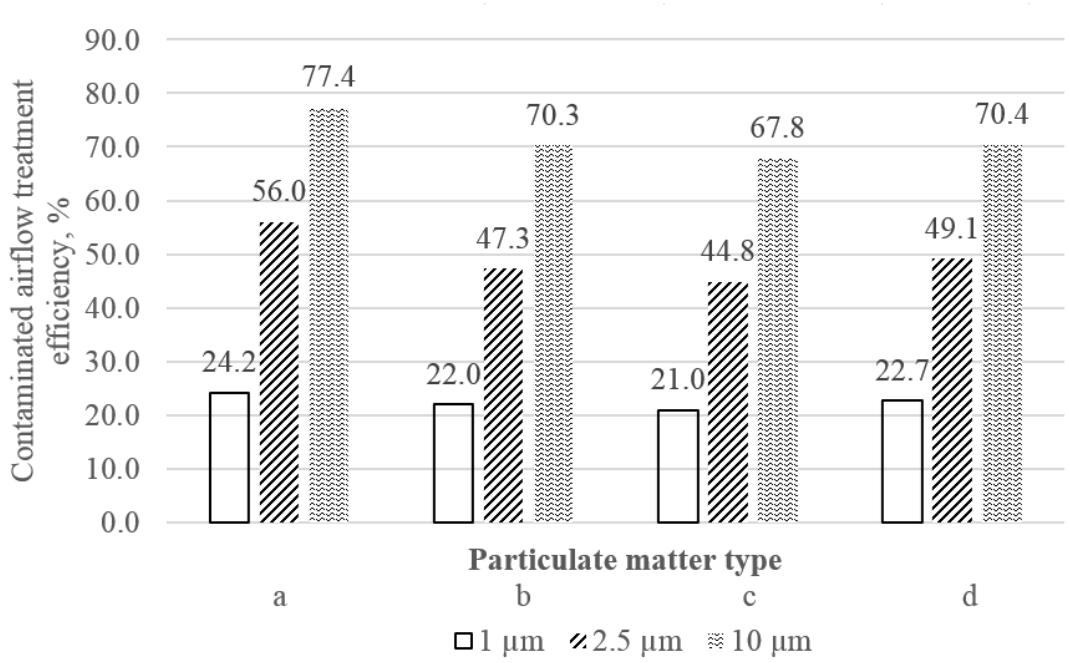

Figure 5. Relationship between air treatment efficiency (Y axis) and PM type and size: a) granite; b) glass; c) wood ash; d) wood

The efficiency of removing granite PM of up to 10 µm was 77.4 %, representing the highest value among other obtained values similarly as in the cases of larger particles. The pre-cyclone fraction of granite PM10 was 56.4 %, while

after exiting the cyclone, this percentage decreased by approx. 4.4-fold to 12.8 %. The efficiency of removing finer particles of up to 2.5 μm in size was lower by approx. 1.4-fold compared to that for PM10 amounting to 56 %. Based on the pre-cyclone distribution of PM, it can be concluded that collection of granite PM2.5 is by approx. 1.8-fold lower as compared to that of PM10. The treatment efficiency for ultra-fine particles of up to 1 μm in size was 24.2 % representing the sharpest decrease in efficiency. As compared to the removal efficiencies of PM10 and PM2.5 μm, the removal efficiency of PM1 is lower by 3.2- and 2.3-fold, respectively. The PM1 fraction in the inlet gas was lower than those of PM10 and PM2.5 amounting to 9.4 % and decreasing to 7.1 % after exiting the cyclone. It can be presumed that due to the low concentration, the finer particles failed to agglomerate and thus were more difficult to collect than larger particles. While moving together with the other particles, PM2.5 and PM10 are likely to be additionally influenced by autohesion: the particles are bonded together and settle down under a greater force of gravity acting on the aggregates.

Similar removal efficiency trends were found for all the other PM types being the highest for PM10 and the lowest for PM1. Also, in all cases the initial fraction of the largest particles was the highest, while that of the smallest particles was the lowest. The obtained efficiency of removing wood ash PM and wood PM is more or less the same. Similarly, research on fly ash particles (density of 1989.7 kg m^{-3}) from a coal-fired boiler in a power plant showed separation efficiencies in a cyclone of 62 % for PM10 and 11 % for PM1 [35]. The average difference in removal efficiency between granite PM and wood ash/wood PM is approx. 7 %. The poorest results have been obtained in the case of removing ultra-fine particles of up to 1 μm in size. For removal of submicron particles higher-efficiency devices can be used such as venturi scrubbers, baghouse filters and electrostatic precipitators. In an interesting attempt to improve cyclone efficiency an electric field-assisted cyclone was designed, which achieved high removal efficiencies of ultra-fine particles up to 0.3 μm in size [40].

The analysis of the influence of PM size on the air treatment efficiency shows that the multi-channel cyclone collects up to 80 % of PM10. This is seen as good efficiency. However, the collecting efficiency for small particles is significantly lower, *i.e.* up to 60 % for PM2.5 and up to 25 % for PM1. These values are not high. Yet, it is important to note that other cheap alternative technologies capable of collecting fine and ultra-fine particles do not exist. The air treatment efficiency of the multi-channel cyclone could be improved by increasing the number of cyclonic levels.

An improved design of a cyclone-separator with secondary inlets and a more complicated design is presented in literature. Results in that study obtained based on the numerical modeling predicted the effectiveness of trapping PM10 of 72 %, which was on average 1.7-fold higher than that predicted for PM2.5 amounting to 41.3 %. These results were confirmed, experimentally, reaching average trapping efficiencies of 46.9 and 78 % for particulate matter of 2.5 μm and 10 μm in diameter, respectively [34].

Generally, a strong correlation is observed between the particle collection efficiency and the size distribution (Fig 6), as already demonstrated in work of Majoral and co-workers [41].

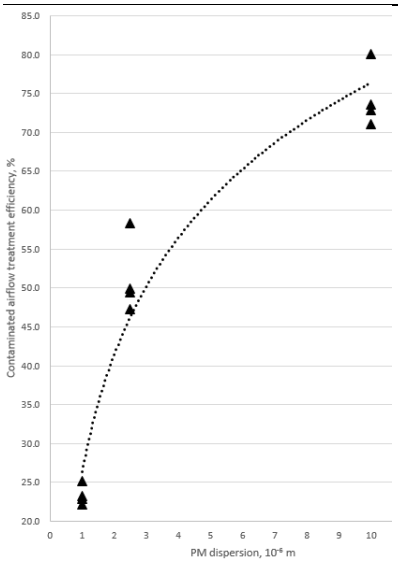

Figure 6. Dependence of air treatment efficiency (Y axis) on PM dispersion (X axis)

Although a good collection efficiency of small PM was achieved by the 8-channel cyclone mock-up it is important to note that the post-cyclone size distribution of PM is different. This should be considered with regards to the air treatment efficiency. The results of tests with the cascade impactor were compared to show changes in the PM distribution before and after the multi-channel cyclone (Figs. 7-10).

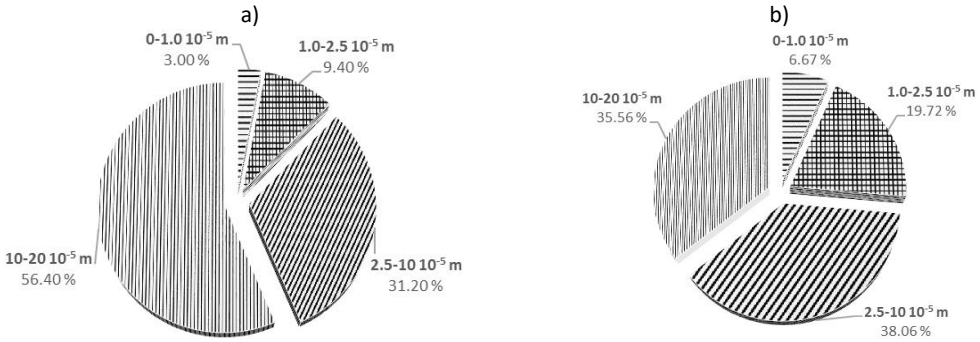

Figure 7. Granite PM distribution before (a) and after (b) in one-level 8-channel cyclone-separator mock-up

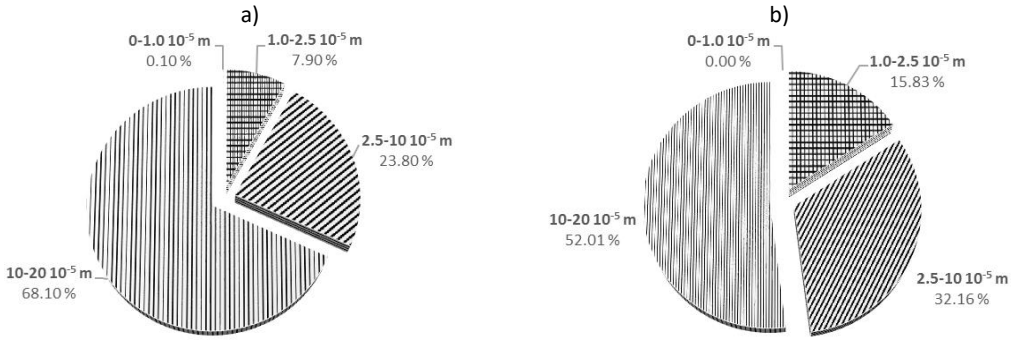

Figure 8. Wood ash PM distribution before (a) and after (b) in one-level 8-channel cyclone-separator mock-up

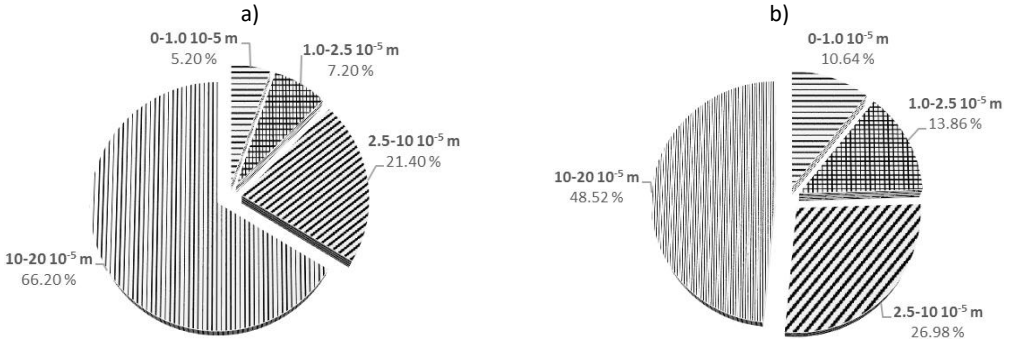

Figure 9. Wood PM distribution before (a) and after (b) in one-level 8-channel cyclone-separator mock-up

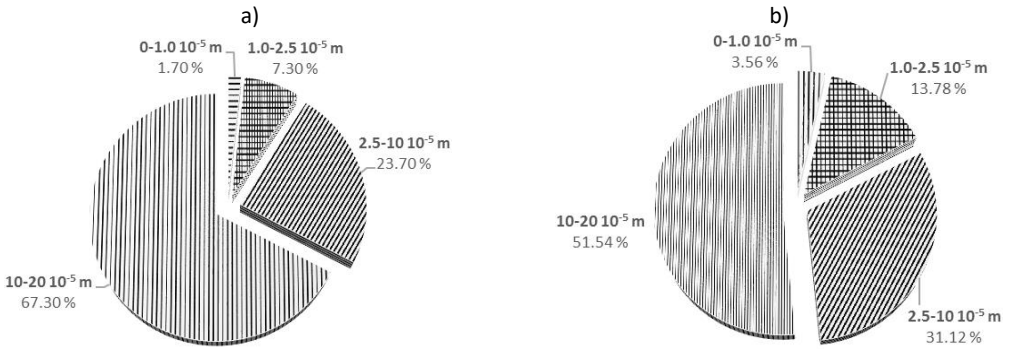

Figure 10. Glass PM distribution before (a) and after (b) in one-level 8-channel cyclone-separator mock-up

As it is known, air treatment is more efficient in collecting larger particles. Therefore, the percentage of small PM fractions is higher after the treatment. For example, the overall decrease in fractions of PM ranging from 10 to 20 µm in size was in the range 16-21 %, while the fractions of finer PM increased for: 5-9 % for PM 2.5-10 µm in size, 6-10 % for PM 1-2.5 µm in size and 2-5 % for PM1. These results point to future development of air treatment technologies capable of more efficient collection of fine and especially ultra-fine PM.

4. CONCLUSION

Based on the results obtained in this investigation, the following conclusions were drawn.

One-level 8-channel cyclone-separator collects 70 to 80 % of PM up to 10 µm in size, 45 to 60 % of PM up to 2.5 µm in size and 21 to 25 % of PM up to 1 µm in size.

Experimental studies have shown that the aerodynamic resistance of gas flow reaches 1150 Pa at the gas flow rate of up to 950 $m^3 h^{-1}$. A chain of eight sequentially arranged cyclone-separator channels, local obstructions and additional intense mixing and turbulence in the inlet and outlet are the main zones of the pressure drop.

The highest efficiency was achieved in removing high-density granite PM of fine dispersion. The analysis of PM of up to 20 µm in size showed 77.4 % efficiency under a 50/50 flow distribution ratio between the transitional and peripheral flows when the average air velocity was 10 m s^{-1}.

At the same conditions the treatment efficiency for medium-density PM (glass) of up 20 µm in size was 67.8 % those for wood ash and wood PM were 70.3 and 70.4 %, respectively.

The separation efficiency of PM up to 2.5 µm in size strongly decreased as the particle density is lower. It could be assumed that the increase in the number of levels in the multi-channel cyclone-separator will improve the air treatment efficiency. However, this solution requires the increased gas flow rate and energy needs due to the increased aerodynamic resistance.

Overall, the multi-channel cyclone-separator was shown to be efficient in removing particulate matter down to 20 µm in size from air. To clean smaller particles, it is reasonable to use other air treatment technologies.

REFERENCES

[1] Kirsanovs V, Blumberga D, Veidenbergs I, Rochas C, Vigants E, Vigants G. Experimental investigation of downdraft gasifier at various conditions. *Energy Procedia*. 2017; 128: 332-338 https://doi.org/10.1016/j.egypro.2017.08.321.

[2] Choi HY, Park YG, Ha MY. Numerical simulation of the wavy collecting plate effects on the performance of an electrostatic precipitator. *Powder Technol*. 2021; 382: 232-243 https://doi.org/10.1016/j.powtec.2020.12.070.

[3] Lee GH, Hwang SY, Cheon TW, Kim HJ, Han B, Yook SJ. Optimization of pipe-and-spike discharge electrode shape for improving electrostatic precipitator collection efficiency. *Powder Technol*. 2021; 379: 241-250 https://doi.org/10.1016/j.powtec.2020.10.044.

[4] Zhang X, Bo T. The effectiveness of electrostatic haze removal scheme and the optimization of electrostatic precipitator based on the charged properties of airborne haze particles: Experiment and simulation. *J Clean Prod*. 2021; 288: 125096 https://doi.org/10.1016/j.jclepro.2020.125096.

[5] Gao Z, Wang J, Liu Z, Wei Y, Wang J, Mao Y. Effects of different inlet structures on the flow field of cyclone separators. *Powder Technol*. 2020; 372: 519-531 https://doi.org/10.1016/j.powtec.2020.06.014.

[6] Fatahian E, Fatahian H, Hosseini E, Ahmadi G. A low-cost solution for the collection of fine particles in square cyclone: A numerical analysis. *Powder Technol*. 2021; 387: 454-465 https://doi.org/10.1016/j.powtec.2021.04.048.

[7] Joo YS, Kim J, Lee J, Chung I-J. Understanding the link between exposure to fine particulate matter and internalizing problem behaviors among children in South Korea: Indirect effects through maternal depression and child abuse. *Health Place*. 2021; 68: 102531 https://doi.org/10.1016/j.healthplace.2021.102531.

[8] Cheng J, Ho HC, Webster C, Su H, Pan H, Zheng H, Xu Z. Lower-than-standard particulate matter air pollution reduced life expectancy in Hong Kong: a time-series analysis of 8.5 million years of life lost. *Chemosphere*. 2021; 272: 129926 https://doi.org/10.1016/j.chemosphere.2021.129926.

[9] Sharma J, Parsai K, Raghuwanshi P, Ali SA, Tiwari V, Bhargava A, Mishra PK. Emerging role of mitochondria in airborne particulate matter-induced immunotoxicity. *Environ Pollut*. 2021; 270: 116242 https://doi.org/10.1016/j.envpol.2020.116242.

[10] Magee BH, Forsberg ND. Testing the validity of a proposed dermal cancer slope factor for Benzo[a]pyrene. *Regul Toxicol Pharmacol*. 2021; 120: 104852 https://doi.org/10.1016/j.yrtph.2020.104852.

[11] Qi X-M, Luo Y, Song M-Y, Liu Y, Shu T, Liu Y, Pang J-L, Wang J, Wang C. Pneumoconiosis: current status and future prospects. *Chin Med J (Engl)*. 2021; 134(8) https://doi.org/10.1097/CM9.0000000000001461.
[12] Liu L. China's dusty lung crisis: Rural-urban health inequity as social and spatial injustice. *Soc Sci Med*. 2019; 233: 218-228 https://doi.org/10.1016/j.socscimed.2019.05.033.
[13] Wu X, Wu K, Zhang Y, Hong Q, Zheng C, Gao X, Cen K. Comparative life cycle assessment and economic analysis of typical flue-gas cleaning processes of coal-fired power plants in China. *J Clean Prod*. 2017; 142: 3236-3242 https://doi.org/10.1016/j.jclepro.2016.10.146.
[14] Torsky A, Volnenko A, Plyatsuk L, Hurets L, Zhumadullayev D, Abzhabparov A. Study of dust collection effectiveness in cyclonic-vortex action apparatus. *Technol Audit Prod Reserv*. 2021; 1: 21-25 https://doi.org/10.15587/2706-5448.2021.225328.
[15] Shastri R, Brar LS. Numerical investigations of the flow-field inside cyclone separators with different cylinder-to-cone ratios using large-eddy simulation. *Sep Purif Technol*. 2020; 249: 117149 https://doi.org/10.1080/02726351.2021.1905123.
[16] Oliveira RAF, Guerra VG, Lopes GC. Improvement of collection efficiency in a cyclone separator using water nozzles: A numerical study. *Chem Eng Process - Process Intensif*. 2019; 145: 107667 https://doi.org/10.1016/j.cep.2019.107667.
[17] Sati V, Kaushik S, Kshetri R, Panwar K, Pandey R. Comparison of a Classical Cyclone Separator and Protruding Surface Cyclone Separator using CFD Software. *IOP Conf Ser Mater Sci Eng*. 2020; 802: 12008 https://doi.org/10.1088/1757-899X/802/1/012008.
[18] Honda A, Okuda T, Nagao M, Miyasaka N, Tanaka M, Takano H. PM2.5 collected using cyclonic separation causes stronger biological responses than that collected using a conventional filtration method. *Environ Res*. November 2020: 110490 https://doi.org/10.1016/j.envres.2020.110490.
[19] Zhang Y, Yang M, Jiang L, Wang H, Xu J, Yang J. High Concentration Fine Particle Separation Performance in Hydrocyclones. *Minerals*. 2021; 11: 307 https://doi.org/10.3390/min11030307.
[20] Ma L, Ingham DB, Wen X. Numerical modelling of the fluid and particle penetration through small sampling cyclones. *J Aerosol Sci*. 2000; 31(9): 1097-1119 https://doi.org/10.1016/S0021-8502(00)00016-1.
[21] Seposo X, Arcilla ALA, De Guzman JGN, Dizon EMS, Figuracion ANR, Morales CMM, Tugonon PKA, Apostol GLC. Ambient air quality and the risk for Chronic Obstructive Pulmonary Disease among Metro Manila Development Authority traffic enforcers in Metro Manila: An exploratory study. *Chronic Dis Transl Med*. February 2021 https://doi.org/10.1016/j.cdtm.2021.01.002.
[22] Guo W, Chen L, Fan Y, Liu M, Jiang F. Effect of Ambient Air Quality on Subjective Well-Being among Chinese Working Adults. *J Clean Prod*. February 2021: 126509 https://doi.org/10.1016/j.jclepro.2021.126509.
[23] Thomas J, Jainet PJ, Sudheer KP. Ambient air quality of a less industrialized region of India (Kerala) during the COVID-19 lockdown. *Anthropocene*. 2020; 32: 100270 https://doi.org/10.1016/j.ancene.2020.100270.
[24] Singh S. Ambient air quality examination of a cement industry: A case study. *Mater Today Proc*. 2020; 37: 3635-3638 https://doi.org/10.1016/j.matpr.2020.09.782
[25] Garg A, Kumar A, Gupta NC. Comprehensive study on impact assessment of lockdown on overall ambient air quality amid COVID-19 in Delhi and its NCR, India. *J Hazard Mater Lett*. 2021; 2: 100010 https://doi.org/10.1016/j.hazl.2020.100010.
[26] Li Y, Qin G, Xiong Z, Ji YF, Fan L. The effect of particle humidity on separation efficiency for an axial cyclone separator. *Adv Powder Technol*. 2019; 30(4): 724-731 https://doi.org/10.1016/j.apt.2019.01.002.
[27] Wang J, Duan X, Wang S, Wen J, Tu J. Experimental and numerical investigation on the separation of hydrophilic fine particles using heterogeneous condensation preconditioning technique in gas cyclones. *Sep Purif Technol*. 2021; 259: 118126 https://doi.org/10.1016/j.seppur.2020.118126.
[28] Li W, Hu Z, Pei Z, Li S, Chan PW. A discussion on influences of turbulent diffusivity and surface drag parameterizations using a linear model of the tropical cyclone boundary layer wind field. *Atmos Res*. 2020; 237: 104847 https://doi.org/10.1016/j.atmosres.2020.104847.
[29] Parvaz F, Hosseini SH, Elsayed K, Ahmadi G. Influence of the dipleg shape on the performance of gas cyclones. *Sep Purif Technol*. 2020; 233: 116000 https://doi.org/10.1016/j.seppur.2019.116000.
[30] Thorn R. Reengineering the cyclone separator. *Met Finish*. 1998; 96(8): 30 https://doi.org/10.1016/s0026-0576(98)80589-8.
[31] Baltrėnas P, Chlebnikovas A. Investigation into the Aerodynamic Parameters of the Recently Designed Two-Level Cylindrical Multi-Channel Cyclone-Separator. *Sep Sci Technol*. 2015; 50(8) https://doi.org/10.1080/01496395.2014.967774.
[32] Baltrėnas P, Chlebnikovas A. Cylindrical multi-level multi-channel cyclone-filter. European Patent. 2019: 1-15.
[33] El Ashry Y, Abdelrazek AM, Elshorbagy KA. Numerical and experimental study on the effect of solid particle sphericity on cyclone pressure drop. *Sep Sci Technol*. 2018; 53(15): 2500-2516 https://doi.org/10.1080/01496395.2018.1458878.
[34] Baltrėnas P, Crivellini A, Leonavičienė T, Chlebnikovas A. Investigation on particulate matter and gas motion processes in the advanced multi-channel cyclone-separator with secondary gas inlets. *Environ Eng Res*. 2022; 27(1): 200550 https://doi.org/10.4491/eer.2020.550.
[35] Wang C, Zhang Y, Dong K, Wang B, Li S, Xin R, Jiang Y. Enhanced collection of fine particles in a cyclone using ultrasonic vapor with surfactants. *Adv Powder Technol*. 2020; 31(6): 2207-2214 https://doi.org/10.1016/j.apt.2020.03.015.
[36] Vaitiekūnas, P., Petraitis, E., Venslovas, A., & Chlebnikovas A. Air stream velocity modelling in multichannel spiral cyclone separator. *J Environ Eng Landsc Manag*. 2014; 22(3): 183-193 https://doi.org/10.3846/16486897.2014.931283.

[37] Baltrėnas P, Chlebnikovas A. The investigation of the structure and operation of a multi-channel cyclone, separating fine solid particles from an aggressive dispersed gas and vapour flow. *Powder Technol*. 2018; 333: 327-338 https://doi.org/10.1016/j.powtec.2018.04.043.
[38] Shaw B, Faulkner W. Efficiency and pressure drop of cyclones across a range of inlet velocities. *Appl Eng Agric*. 2006; 22 https://doi.org/10.13031/2013.20191.
[39] Nassaj OR, Toghraie D, Afrand M. Effects of multi inlet guide channels on the performance of a cyclone separator. *Powder Technol*. 2019; 356: 353-372 https://doi.org/10.1016/j.powtec.2019.08.038.
[40] Jeon H, Park S. Separation of fine particles with electrostatically enhanced cyclone. *Sep Sci Technol*. 2020; 55(3): 575-582 https://doi.org/10.1080/01496395.2019.1567553.
[41] Furuuchi M, Kanaoka C, Shimizu Y. *Separation Characteristics of a Supersonic Virtual Impactor*.; 2004 https://doi.org/10.11491/apcche.2004.0.36.0.

SAŽETAK

Eksperimentalno istraživanje jednostepenog osmokanalnog industrijskog ciklonskog separatora

Aleksandras Chlebnikovas

Environmental Protection Institute, Institute of Mechanical Science, Vilnius Gediminas Technical University, Vilnius, Lithuania

(Stručni rad)

Glavni cilj ovog istraživanja je eksperimentalna analiza efikasnosti prečišćavanja vazduha u prototipu uređaja nove generacije - jednostepenom osmokanalnom industrijskom ciklonskom separatoru - uz promenu parametara unutrašnje strukture i određivanje efekata disperzije čestica. Stoga je istraživanje sprovedeno u dve faze: prva je obuhvatala analizu efikasnosti višekanalnog ciklona sa česticama <20 i <50 µm. Tokom druge faze, kaskadni impaktor je korišćen za određivanje efikasnosti izdvajanja čestica u višekanalnom ciklonu po frakcijama: PM1, PM2.5 i PM10. Upoređeni su rezultati ispitivanja sa kaskadnim impaktorom kako bi se pokazale promene u sastavu čestica pre i posle primene višekanalnog ciklonskog separatora. Prema dobijenim eksperimentalnim podacima, osmokanalni ciklonski separator na jednom nivou sakuplja 70 do 80 % čestica veličine do 10 mikrona, 45 do 60 % čestica veličine do 2,5 mikrona i 21 do 25 % čestica veličine do 1 mikrona.

Ključne reči: višekanalni ciklonski separator; čestice; tretman vazduha; kanal; kaskadni impaktor.

MC2021 ended successfully: The limits of the measurable - exciting developments and latest trends in light and electron microscopy

CONFERENCE REPORT

Kerstin Aldenhoff

Science journalist, Dresden, Germany

From dancing atoms to fundamental questions about the limits of the measurable - after five exciting conference days on current developments and latest trends in light and electron microscopy, the Microscopy Conference MC2021 (https://www.microscopy-conference.de/) came to a successful close. Microscopy societies from 11 countries - Austria, Croatia, Czech Republic, Germany, Hungary, Italy, Serbia, Slovakia, Slovenia and Switzerland -, organised the digital Joint Meeting of Dreiländertagung and Multinational Congress on Microscopy. Led by the congress presidents Johannes Bernardi, Michael Stöger-Pollach and Stefan Löffler, Vienna University of Technology, MC2021 offered a comprehensive scientific exchange with a diverse program.

New research results were presented in eight thematic sessions on life sciences, materials science, and instrumentation and methods by experts from all fields. As the only major electron microscopy meeting in Europe this year, MC2021 offered especially for the so-called "early-stage researchers" (ESRs) best opportunities for an international scientific exchange to develop, network and gain new insights. A large number of younger researchers took the opportunity to present their work with exciting talks.

Keywords: life sciences; materials science; instrumentation and methods.

Available on-line at the Journal web address: http://www.ache.org.rs/HI/

BOOK AND EVENT REVIEW

UDC: 005.745:543.456:537.533.35

Hem. Ind. **75 (4)** 253-256 (2021)

INTERDISCIPLINARITY AND EXCELLENT QUALITY OF THE MC2021

Special emphasis was placed on applications and developments of various microscopy techniques in the field of light and electron microscopy, which have made incredible progress in the last 20 years and have become indispensable in countless areas of research. Johannes Bernardi emphasised the high value of the new spectacular improvements and findings in these techniques. "The creativity of science opens new doors to better understand life, but also inorganic matter," said Michael Stöger-Pollach. The combination of the fields of life sciences, materials sciences and methods technology formed the major common focus. Stefan Löffler referred to the broad interdisciplinary set-up of MC2021 with excellent quality in all areas, which could not have been achieved otherwise.

The presentations showed that the trends of breakthrough improvements in electron microscopy in the field of imaging and analytics, as well as progressive automation, continued. It was clear that development of even more efficient and faster detectors and measurement methods also continues, and further advances are taking place in terms of method development in electron beam phase manipulation and the flexibility of available electron energies.

NEW DEVELOPMENTS IN LIFE SCIENCES AND MATERIALS SCIENCE

In the field of life sciences, the focus was on new developments in cryo-microscopy and in correlative techniques that combine different measurement methods on different size scales to better understand living nature with the help of this special technology. A wide range of interesting content was covered - from sample preparation and aspects of basic research to diagnostic and therapeutic applications in medicine and biotechnology.

In the field of materials science, the focus was not only on material-related topics but also on a wide variety of analytical methods. In the presentations it became clear how much "in-situ" and "in-operando" applications have gained

Corresponding author: Kerstin Aldenhoff, Science journalist, Dresden, Germany
E-mail: kerstin.aldenhoff@gmail.com

in importance. For example, gas or liquid cell imaging and spectroscopic techniques have been shown to enable the investigation of chemical reactions and processes in near real time.

MC2021 The Congress presidents, Johannes Bernardi, Michael Stöger-Pollach and Stefan Löffler (Foto CONVENTUS)

Another focus was on investigations using a wide variety of analytical techniques, as well as micro- and nano-mechanical methods to study structure-property relationships in new functional materials. Sessions on energy storage, catalysts and semiconductors, and the study of metals and ceramics were well attended.

ELECTRON MICROSCOPY IN MEDICAL RESEARCH

Presentations on cryo-microscopy capabilities and applications of machine learning and automation highlighted the essential role that high-resolution electron microscopy plays in medical research. Fascinating applications of high-resolution light microscopy were also presented in this area by labelling proteins genetically or marking them with dyes and tracking them in the organism. With regard to the fight against the coronavirus, it was fascinating to learn what an essential contribution high-resolution electron microscopy could make to the success of vaccine development. Thereby, understanding the complex structure of the viral envelope was crucial.

New developments in nanoscience were another conference focus. In addition to interesting presentations on the generation and investigation of nanostructures that can be produced by chemical processes or specifically by means of focused ion beams, research on 2D materials with special electrical properties, e.g., anisotropic dielectric properties, was presented.

DISCUSSION ON THE EU PROJECT "HORIZON EUROPE”

A special highlight was the high-level panel discussion on the EU project "Horizon Europe", in which new research infrastructures were presented. Internationally renowned experts shed light on the new opportunities offered by the European Union's planned research framework program to address global challenges for electron microscopy. Based on the analysis of previous projects, the question on how the electron microscopy community in Europe can organise broad access to its know-how was discussed. In this way, it will continue to play a crucial role in issues such as climate change adaptation, healthy oceans, climate-neutral cities, healthy nutrition and the fight against cancer.

HIGH-PROFILE PLENARY SPEAKERS AND AWARD CEREMONIES

Conference highlights were exciting presentations on important current topics. Renowned plenary speakers such as Sandra van Aert (University of Antwerp), Sarah Haigh (University of Manchester), Stefan Raunser (MPI Dortmund), Andreas Rosenauer (University of Bremen), Holger Stark (MPI Göttingen) and Marc Willinger (ETH Zurich) were able to inspire the participants with a broad range of topics in excellent presentations - from dancing atoms to fundamental questions about where the limits of the measurable lies.

A special highlight was the award of the internationally renowned Ernst Ruska Prize, awarded every two years, to Julia Mahamid (EMBL, Heidelberg) and to David A. Muller (Cornell University, USA), honoring the two scientists for their outstanding achievements in the field of electron microscopy. Joachim Mayer (RWTH Aachen and ER-C Jülich) was honored with the "Harald Rose Distinguished Lecture" award.

OUTLOOK 2023

Following the diverse exchange between young colleagues, experienced scientists and companies, the conference leaders were convinced that with MC2021 the successful series of joint conferences could be continued even during the pandemic. The next insights into the exciting properties of the world of atoms and molecules can be expected at the MC2023 Annual Meeting in Darmstadt from February 26 to March 2, 2023.

MC 2021 je uspešno završen: Granice merljivog - uzbudljiv razvoj i najnoviji trendovi u svetlosnoj i elektronskoj mikroskopiji

Kerstin Aldenhoff

Naučni novinar, Dresden, Nemačka

Izvod

Nakon pet uzbudljivih konferencijskih dana o razvoju i najnovijim trendovima u svetlosnoj i elektronskoj mikroskopiji, obuhvatajući teme od atoma “koji plešu” do fundamentalnih pitanja o granicama merljivog, konferencija o mikroskopiji MC2021 (https://www.microscopy-conference.de/) uspešno je završena. Društva za mikroskopiju iz 11 zemalja - Austrije, Hrvatske, Češke, Nemačke, Mađarske, Italije, Srbije, Slovačke, Slovenije i Švajcarske organizovala su digitalni združeni sastanak: Dreilandertagung (Konferencija tri zemlje) i Multinacionalni kongres o mikroskopiji. Predsednici kongresa bili su Johanes Bernardi, Majkl Stoger-Polak i Stefan Lofler sa Tehnološkog univerziteta u Beču. MC2021 je ponudio sveobuhvatnu razmenu naučnih informacija kroz raznovrsni program. Stručnjaci iz različitih oblasti predstavili su nove rezultate istraživanja u okviru osam tematskih sesija o prirodnim naukama, nauci o materijalima i razvoju opreme i metoda. Kao jedini veliki sastanak na temu elektronske mikroskopije u Evropi ove godine, MC2021 je bio posebno važan za istraživače na početku karijere, takozvane ""Early-Stage Researchers (ESRs)", nudeći najbolje mogućnosti za međunarodnu razmenu naučnih informacija u cilju razvoja, umrežavanja i sticanja novih saznanja. Veliki broj mlađih istraživača iskoristio je priliku da predstavi svoja istraživanje kroz usmene prezentacije.

Ključne reči: prirodne nauke; nauka o materijalima; instrumenti i metode

PRIKAZ KNJIGA I DOGAĐAJA

UDK:005.745:543.456:537.533.35

Hem. Ind. **75 (4)** 253-256 (2021)